Ph.D Thesis

2016

MULTIFACETED PROPERTIES OF LiNbO$_3$ THIN FILMS FOR OPTICAL APPLICATIONS AND POROUS Zr$_{0.8}$Sn$_{0.2}$TiO$_4$ FOR SENSING APPLICATIONS

ANIL TUMULURI

Advanced Centre of Research in High Energy Materials (ACRHEM)
SCHOOL OF PHYSICS
UNIVERSITY OF HYDERABAD

MULTIFACETED PROPERTIES OF LiNbO$_3$ THIN FILMS FOR OPTICAL APPLICATIONS AND POROUS Zr$_{0.8}$Sn$_{0.2}$TiO$_4$ FOR SENSING APPLICATIONS
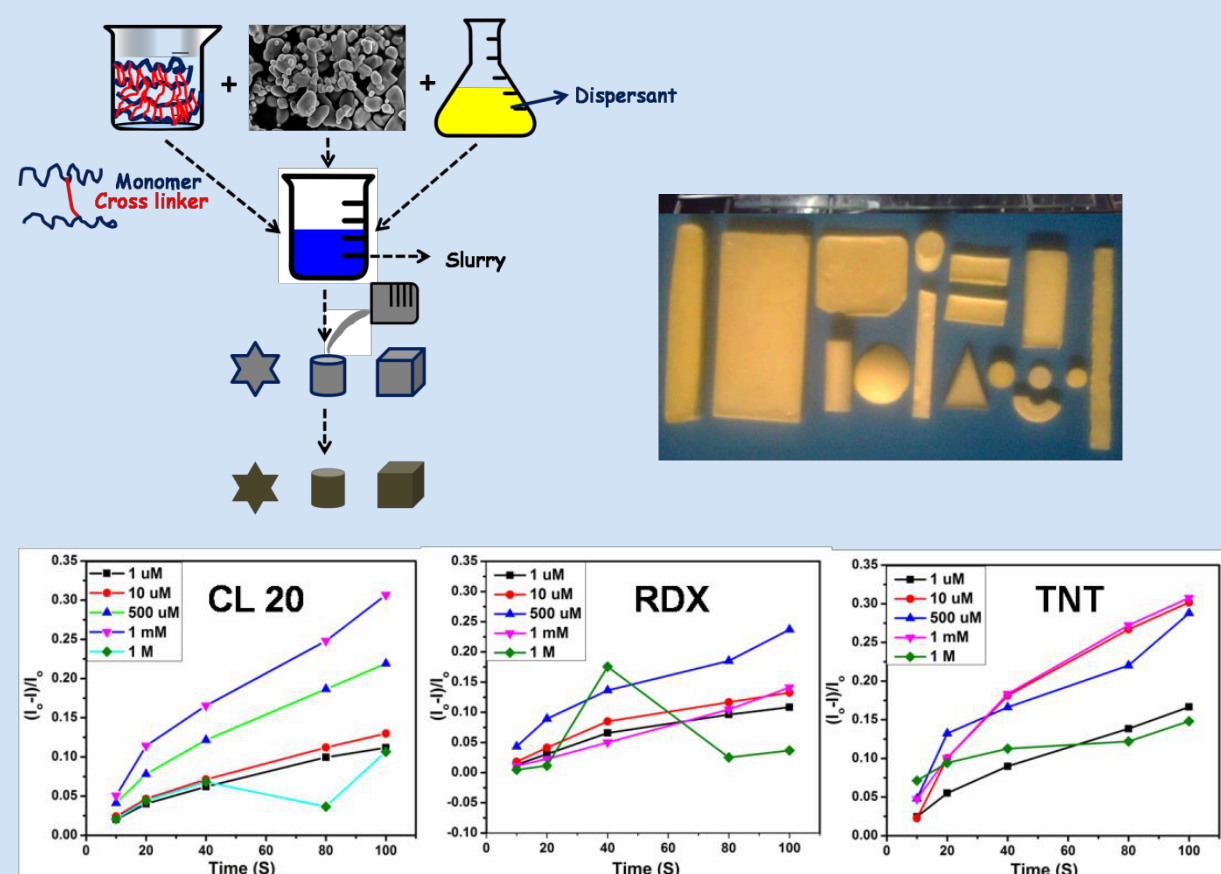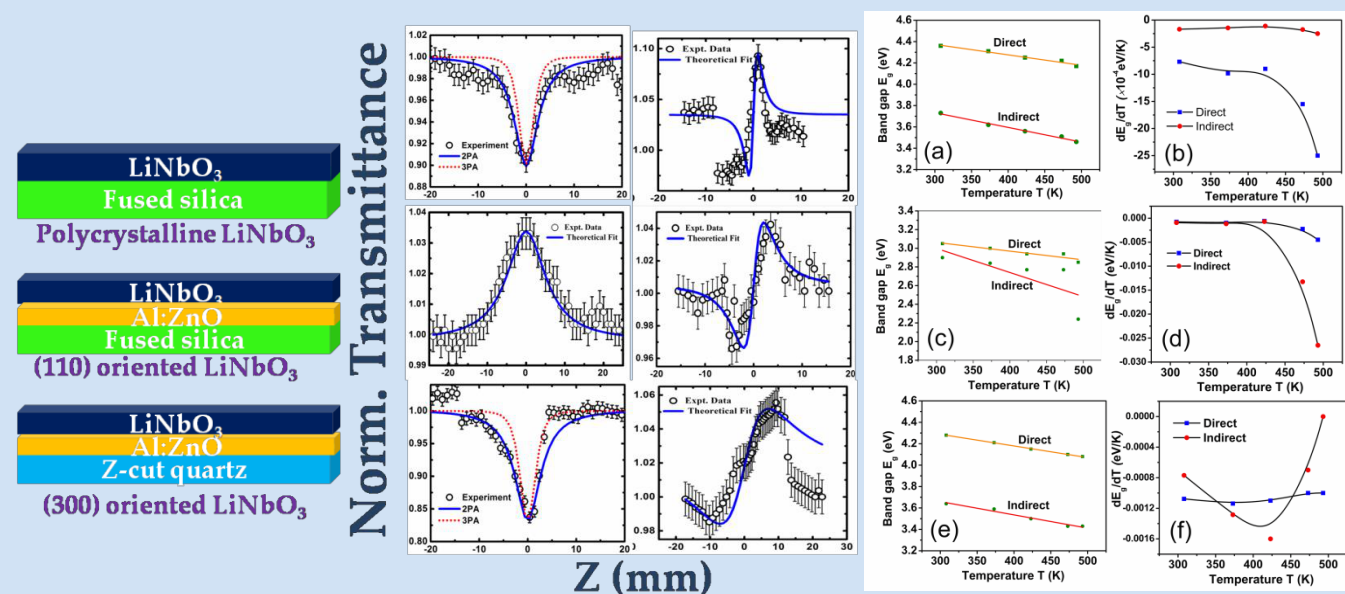
A thesis submitted for the degree of

DOCTOR OF PHILOSOPHY in PHYSICS

by

ANIL TUMULURI

Advanced Centre of Research in High Energy Materials (ACRHEM)
SCHOOL OF PHYSICS
UNIVERSITY OF HYDERABAD
HYDERABAD
INDIA

AUGUST 2016

TO
MY PARENTS
AND
FAMILY

DECLARATION

I, Anil Tumuluri, hereby declare that the thesis entitled *"MULTIFACETED PROPERTIES OF LiNbO$_3$ THIN FILMS FOR OPTICAL APPLICATIONS AND POROUS Zr$_{0.8}$Sn$_{0.2}$TiO$_4$ FOR SENSING APPLICATIONS"* **submitted by me under the guidance and supervision of Prof. K. C. James Raju is a bonafide research work which is also free from plagiarism. I also declare that it has not been submitted previously in part or in full to University of Hyderabad or any other University or Institution for the award of any degree or diploma. I hereby agree that my thesis can be deposited in Shodganga/INFLIBNET.**

A report on plagiarism statistics from the University Librarian is enclosed.

Date:

<div align="right">

Anil Tumuluri

(Reg. No. 10ACPP15)

</div>

Signature of the Supervisor

CERTIFICATE

This is to certify that the research work presented in the thesis entitled *"MULTIFACETED PROPERTIES OF $LiNbO_3$ THIN FILMS FOR OPTICAL APPLICATIONS AND POROUS $Zr_{0.8}Sn_{0.2}TiO_4$ FOR SENSING APPLICATIONS"* is an original work carried out by Mr. Anil Tumuluri. This work has been carried out under my supervision. The thesis is submitted by ANIL TUMULURI for the degree of DOCTORATE IN PHILOSOPHY in ACRHEM, SCHOOL OF PHYSICS. This thesis work has not been submitted to any other University partially or fully for the award of any degree.

Date:

Prof. K. C. James Raju   Director   Dean

Supervisor   ACRHEM   School of Physics

<u>*Acknowledgements*</u>

(Anil Tumuluri)

Contents

References

List of publications

Chapter 1

Introduction and aim of present work

In this chapter, usage of ferroelectric thin films for optical applications and porous materials for sensing applications are introduced. Importance of third order nonlinear optical properties and temperature dependent linear optical properties of ferroelectric thin films in optoelectronic devices are reviewed along with the relevant literature. A brief review and the current state of art of different types of sensors being used for explosive sensing have been discussed. In particular, advantages of fluorescence based explosive sensor using dielectric substrates are highlighted. Finally, objectives and a brief outline of thesis are presented.

1.1 Introduction

Understanding and using ferroelectrics as well as dielectric materials for variety of applications opens new windows. Till date, most of the ferroelectrics are being used for Random Access Memories (RAMs), capacitors, piezoelectric applications, pyroelectric applications and sensor applications [Setter et al. (2006)]. Although the fundamentals of the ferroelectrics are well established to use them for industrial applications, some of the unexplored properties limit them from being used in wider applications. Ferroelectrics come under the category of insulators which are well known for tuning their wide band gap [Woo Seok Choi et al. (2012), Manoj K. Gupta et al. (2012)]. This band gap can be tuned based on external parameters like temperature, engineering the cationic ordering and pressure which can have significant importance in optoelectronics [Nechache et al. (2015)]. Most of the ferroelectrics are being used in bulk polycrystalline or single crystal form. Studies on temperature dependent optical properties of ferroelectric thin films have not been explored much [Hu et al. (2007)].

On the other hand, dielectrics are the prime components in various applications like capacitors, filters, antennas and resonators [Sulong et al. (2016), Subba Rao et al. (1990)]. The usage of dielectrics for various applications is possible only when the study of interesting relationships among their crystal structure, crystal chemistry and physical properties are successfully understood. Recent dramatic changes in microelectronics and in particular wireless communication technology have highlighted the importance of materials with unusual combination of physical properties like high dielectric constant and low

dielectric loss [Sulong et al. (2016)]. Apart from these, scope of using dielectrics for novel and innovative sensing applications cannot be neglected. The synthesis of dielectrics in desired shape and size enhances the options in using them for many more applications [Jinlong Yang et al. (2011)]. In addition, porous materials have added advantages [Hammel et al. (2014)]. So far, literature available on the porous dielectrics for sensing applications is meager [Farid A. Harraz et al. (2014)]. In the following sections, fundamentals on temperature dependent optical properties as well as dielectric materials and their use in sensing of nitro based compounds are introduced.

The present thesis plan is categorized into two applications.

1. Polycrystalline and oriented $LiNbO_3$ thin films for nonlinear and optoelectronic applications.

2. Porous $Zr_{0.8}Sn_{0.2}TiO_4$ substrates for explosive sensing using fluorescence quenching.

1.2 Introduction to thin films for optical applications

In this section, brief introduction about the materials widely used for optical applications as well as the work done on $LiNbO_3$ is presented.

1.2.1 Materials for optical applications

In the past twenty years, ferroelectrics have seen rapid development since they are essential components in a wide spectrum of applications [Scott et al. (2013)]. Properties of bulk ferroelectrics are well understood whereas the same in thin film are not fully understood as to a great extent since their properties are preparation condition dependent. Understanding the origin of difference between properties of films and those of massive ferroelectrics is advancing but

many questions are still unanswered like the origin of higher dielectric losses, dynamics of light propagation and domain engineering [Setter et al. (2006)]. The applications have triggered intense research towards the understanding of materials and underlying physics to govern the functioning of thin films in devices. One of the well-studied ferroelectric is Lithium niobate ($LiNbO_3$). Properties studied and the applications of $LiNbO_3$ single crystal in various fields from literature are given in table 1.1.

1.2.2 $LiNbO_3$- a versatile material for study

$LiNbO_3$ is an artificial ferroelectric material known for its remarkable combination of functional properties. It is piezoelectric, ferroelectric, pyroelectric presents high nonlinear and electro optic coefficients [MircoImlau et al. (2015)]. $LiNbO_3$ in its single crystal form has many advantages like the possibility to add dopants in a controlled way by standard material processing techniques such as bulk doping, ion implantation or thermal diffusion which further expands the range of possible applications so that $LiNbO_3$ became an important material for integrated optics. Having these advantages, $LiNbO_3$ is being used in numerous optical devices and components in bulk single crystal form (Q-switches, Surface Acoustic Wave filters), optical waveguides (Integrated optical circuits), and domain engineered structures (Optical parametric amplifiers and frequency converters) [Marco Bazzan et al. (2015)]. Lot of literature is available concerning the studies on specific aspects of this material such as ferroelectric domains, optical wave guiding, material processing techniques for the fabrication of integrated optical devices and their properties [Das et al. (2003)].
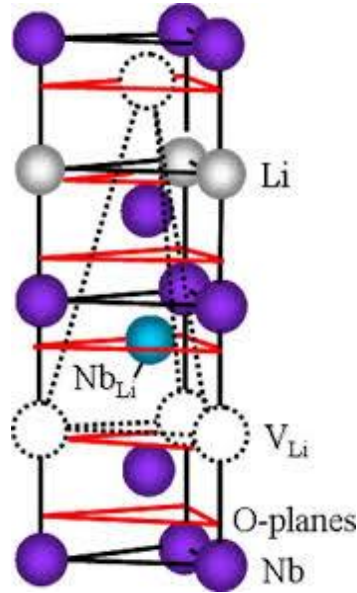
Fig. 1.1: Structure of LiNbO₃ unit cell (Violet balls represent Nb atoms and white balls represent the Li atoms, red planes corresponds to oxygen planes, dotted circles represent the Li vacancies)

The much studied literature witness the widespread interest on LiNbO₃ (single crystal in particular). Based on industrial demand, single crystal LiNbO₃ of large wafers are available at a reasonable price with sophisticated processing technology. On the other hand, there are several new aspects that are only recently being understood. Properties of LiNbO₃ vary drastically with respect to the change in processing methods and form of material being used. In particular, intrinsic defects play a key role in determining the nucleation and growth which in turn affects the optical, piezoelectric and ferroelectric properties [MircoImlau et al. (2015)]. Lithium niobate's structure at temperatures below its ferroelectric Curie temperature (approximately 1210°C) consists of planar sheets of oxygen atoms in a distorted hexagonal close-packed configuration [Weis et al. (1985)]. The octahedral interstices formed in this structure are one third filled by lithium atoms, one-third filled by niobium atoms, and one-third vacant. In the c axis

direction, the atoms occur in the interstices in the order of Nb, vacancy, Li, Nb, vacancy, Li. The positions of the lithium and niobium atoms in ferroelectric phase are shown in Fig. 1.1.

Table 1.1: Reports in literature on usage of LiNbO$_3$ single crystal for different applications

Material	Principle/Technique	Application	References
X-cut and Z-cut 700 µm Er:LiNbO$_3$ single crystal using ion implantation	Prism coupling technique	Optical waveguide	JakerbCajzl et al. (2016)
Z-cut LiNbO$_3$ single crystal	Ion implantation and wafer bonding technique	Domain switching	Jiang et al. (2015)
X-cut LiNbO$_3$	Capacitive technique	Piezoelectric transducer	Syed Bukhari et al. (2014)
Periodically poled LiNbO$_3$ single crystal	Quasi Phase matching	Terahertz generation	Ruolin Chen et al. (2012)
1 mm slab of LiNbO$_3$	Resonant acousto optic technique	Terahertz filter	Poolman et al. (2011)
Swift heavy mass ions such as Xe and Kr irradiated Z-cut LiNbO$_3$ single crystal	Second order non-linear response	Thick planar waveguides	Jose Olivares et al. (2009)
C-cut plates of LiNbO$_3$:Fe	EPR spectroscopy for LiNbO$_3$:Fe	Ferroelectric specific Stark effect	Basun et al. (2008)
Multilayered LiNbO$_3$	Piezoelectric vibration characteristic and linearity	Piezoelectric actuator	AkitoKawamata et al. (2007)
Z-cut 500 µm congruent LiNbO$_3$ single crystal	Second harmonic generation through parametric spatial solitons in a 2D purely nonlinear lattice	LiNbO$_3$ optical waveguides	Katio Gallo et al. (2008)
X-cut LiNbO$_3$ single crystal	Surface Acoustic Wave based	Acousto-optical tunable filter	Wen Chuan Jing et al. (2005)

X-cut LiNbO₃ single crystal	Optical rectification	Terahertz generation	David W.Ward et al. (2005)
LiNbO₃ monocrystal	Acoustic spectroscopy	Piezoelectric crystal	Hassel Ledbetter et al. (2004)

Table 1.2: Literature on deposition of LiNbO₃ thin films and the properties studied so far

Compound	Deposition technique	Substrate-Growth temperature (°C)	Property studied	Reference
LiNbO₃ nanostructures	Sol-gel	Quartz/---	Nanophotonics	A.FakhriMakram et al. (2016)
c-axis oriented LiNbO₃ thin films	Pulsed laser deposition	ZnO/Si-550	Structural (c-axis growth)	Peng You et al. (2013)
Polycrystalline LiNbO₃ thin films	Pulsed laser deposition	SiO₂/Si/ Nanocrystalline diamond-	Surface Acoustic Wave device	Xinchang Wang et al. (2013)
Er and Yb doped LiNbO₃ thin films	Pulsed laser deposition	SiO₂/Si-650 to 800	Luminescence and optical waveguide	M.Jelinek et al. (2013)
Polycrystalline LiNbO₃ thin films	RF magnetron sputtering	(100) Si/SiO₂-550	Piezo response	D.A. Kiselev et al. (2012)
c-axis oriented LiNbO₃ thin films	Pulsed laser deposition	(001) sapphire-700	Optical band gap	Swati Shandilya et al. (2012)
Epitaxial LiNbO₃ thin films	Pulsed injection metal organic chemical vapor deposition	C-cut sapphire-650	Structural (residual stress, thermal expansion)	A.Bartasyte et al. (2012)
c-axis oriented LiNbO₃ thin films	RF magnetron sputtering	(002) ZnO/Si-450	Structural (growth direction and stress)	Swati Shandilya et al. (2012)

c-axis oriented LiNbO$_3$ thin films	Pulsed laser deposition	SiO$_2$/Si/Nanocrystalline diamond	Piezoelectric	Xinchang Wang et al. (2012)
c-axis oriented LiNbO$_3$ thin films	Pulsed laser deposition	Au thin film on BK7 glass prism	Temperature sensor	Swati Shandilya et al. (2010)
Epitaxial LiNbO$_3$ thin films	Pulsed laser deposition	(001) Al$_2$O$_3$	Optical waveguide	S.Kilburger et al. (2009)
Epitaxial LiNbO$_3$ thin films	Pulsed laser deposition	(001) Al$_2$O$_3$	Optical waveguide	S.Kilburger et al. (2009)
c-axis oriented LiNbO$_3$ thin films	Pulsed laser deposition	Al:ZnO/Si-450	Electrical	Swati Shandilya et al. (2009)
Eu doped LiNbO$_3$ thin films	Sol-gel	z-cut congruent LiNbO$_3$-700	Luminescence	Makoto Takahashi et al. (2008)
c-axis oriented LiNbO$_3$ thin films	Pulsed laser deposition	SiO$_2$/Si-600	Optical waveguide	Xinchang Wang et al. (2007)
Ta:LiNbO$_3$ thin films	Sol-gel	Pt(111)/Ti/SiO$_2$/Si(100)	Pyroelectric infrared (IR) detectors	M.C. Kao et al. (2007)
c-axis oriented LiNbO$_3$ thin films	Pulsed laser deposition	Al:ZnO/Si-500	Electrical properties (AC conductivity and dielectric constant)	Vinay Gupta et al. (2005)
c-axis oriented LiNbO$_3$ thin films	Electron Cyclotron Resonance plasma sputtering	(100) Si	Electro optic properties	HouseiAkazawa et al. (2005)
c-axis oriented LiNbO$_3$ thin films	RF diode sputtering	ZnO/Si-450	Optical waveguide	Monika Tomar et al. (2005)
c-axis oriented LiNbO$_3$ thin films	RF magnetron sputtering	(0001) GaN-500 to 650	Ferroelectric	Peter J.Hansen et al. (2005)
c-axis oriented LiNbO$_3$ thin films	Pulsed laser deposition	Al$_2$O$_3$/Diamond	High frequency Surface Acoustic Wave devices	Hi Ki Lam et al. (2004)

c-axis oriented LiNbO₃ thin films	Pulsed laser deposition	(0001) Sapphire	Second harmonic generation	Y Nakata et al. (2004)
c-axis oriented LiNbO₃ thin films	Pulsed laser ablation	SiO₂/Si	Piezoelectric	Parmanand Sharma et al. (2003)
Polycrystalline LiNbO₃	Polymeric precursor method	(100) Silicon-500	Ferroelectric and dielectric	A.Z.Simoes et al. (2003)
Polycrystalline LiNbO₃ thin films	RF sputtering	Quartz	Third order nonlinear optical properties	Wang Qu-Quan et al. (2002)
c-axis oriented LiNbO₃ thin films	Combined RF sputtering and pyrosol technique	(111) Si, (001) Sapphire-650	Surface Acoustic Wave characteristics	V.Bornand et al. (2001)
LiNbO₃ thin films	Pulsed laser deposition	(001) Sapphire-735	Structural (strain in thin film growth)	Yoshihiko Shibata et al. (1997)
Epitaxial LiNbO₃ thin films	Sol-gel	(110) Sapphire-400 to 700	Structure	Keiichi Nashimoto et al. (1991)

1.2.3 Nonlinear optical properties of LiNbO₃

Nonlinear optical properties of LiNbO₃ are of interest due to its application in second order and third order nonlinear optical devices. In second order nonlinearity, two photons are mixed together resulting in creating a third photon of different wavelength. For e.g., Nd:YAG laser emit photons in infrared wavelength of 1064 nm which are mixed in a large second order nonlinear crystal for efficient frequency doubling to generate photons of 532 nm. Devices based on third order nonlinearity involve four photon mixing in which three photons are mixed together to create a fourth photon. In a third order nonlinear crystal, the refractive index and absorption coefficient are significantly modified by the

strength of the light intensity. Examples include a reverse saturable absorber becomes more opaque with increase in intensity because of the manifestation in nonlinear absorption. Based on this phenomenon, nonlinear optical switches have been proposed. The need for search of new materials and their enhanced properties is a critical factor in developing nonlinear optical devices.

$LiNbO_3$ is one of the most important nonlinear optical materials with versatile applications. But, major efforts have been focused on the second order optical nonlinearity $\chi^{(2)}$ because of its applications in parametric oscillation and second harmonic generation. But, additional third order optical nonlinearities $\chi^{(3)}$ in the same were not completely understood and can be used in optical switching devices. The above mentioned second order and third order optical nonlinearities were mostly studied in $LiNbO_3$ single crystals but not in thin films. Therefore, recently there has been increasing interest in $\chi^{(3)}$ studies for $LiNbO_3$ thin films. Details of second order and third order nonlinear optical properties of $LiNbO_3$ in single crystal and thin films from previous literature are given in table 1.3.

Table 1.3: Literature on deposition of $LiNbO_3$ thin films and the properties studied so far

$LiNbO_3$ form	Nonlinear absorption coefficient (β)	Nonlinear refractive index (n_2)	Nonlinear susceptibility ($\chi^{(3)}$)	Reference
$LiNbO_3$ thin film from RF magnetron sputtering	-7.2×10^{-9} cm/kW	0.39 cm²/W	9.1×10^{-7} esu	Wang Qu-Quan et al. (2002)
Z-cut $LiNbO_3$ crystal	------	0.67×10^{-7} cm²/W	------	Rabbani S.M.G. et al. (2011)
Chemically reduced nominally pure $LiNbO_3$ crystals	0.45×10^{-3} cm/kW	------	------	Kostritskii S.M. et al. (2012)

LiNbO₃:MgO single crystal	------	2.0×10⁻¹⁵ cm²/W	------	Li H.P. et al. (2000)
Pure LiNbO₃ single crystal	2.1 × 10⁻¹⁰ cm/W	------	------	Ganeev R.A. et al. (2003)
Periodically poled LiNbO₃	6.0× 10⁻¹² cm/W	------	------	M. Cherchi et al. (2008)
LiNbO₃ single crystal	2.5 × 10⁻¹⁰ cm/W	5.3 × 10⁻¹⁵ cm²/W	7.45 × 10⁻¹³ esu	Heping Li et al. (1996)
LiNbO₃ thin films from PLD	125× 10⁻⁸ cm/W	1.7×10⁻¹³ m²/W	1.0×10⁻⁹ esu	Anil Tumuluri et al. (2016)
Porous LiNbO₃ thin film from RF magnetron sputtering	------	------	1.9 × 10⁻⁸ esu	Ququan Wang et al. (2002)

1.2.4 Temperature dependent optical properties for optoelectronic applications

Ferroelectrics in its bulk form are being used in many optical devices like infrared sensors, nonlinear optical devices and luminescent displays. Having potential applications in versatile fields, ferroelectric thin films are studied for new and emerging areas of applications in random access memories, microwave tunable devices and nonlinear optical micro devices etc. [Shihui Yu et al. (2015), Venkata Saravanan et al. (2010)]. Compared to the bulk single crystals, the optical properties of thin films are strongly influenced by deposition parameters, substrate and deposition techniques.

The emerging trend is to use ferroelectric thin films in multifaceted applications. In particular, the optical properties of ferroelectric thin films are to be extensively explored because of their spontaneous electronic polarization dependence. Lithium Niobate (LN) is a kind of ferroelectric which is widely used for industrial applications in single crystal form. But, the properties of the same in thin film form have not been explored much. It presents a very interesting combination of properties and characteristics that makes possible the realization

of different classes of devices. Up to now many devices like optical waveguides and modulators, pyroelectric sensors and photovoltaic substrates have been fabricated using LiNbO$_3$. Miniaturization of devices is possible if we understand and analyze the properties of LiNbO$_3$ in thin film form. But, focused studies on temperature dependence of LiNbO$_3$ thin films are not reported. This may allow developing potential applications such as ultraviolet detectors, electro optics and high temperature electronic devices. Temperature dependent transmittance spectra can directly provide optical band gap, optical constants, absorption characteristics, band tail state behavior and optical phonon modes.

Studies on temperature dependence of optical band gap are still in the preliminary stage owing to the scope for study and scarce known physical parameters. The temperature dependence changes the characteristics of functionality for thin film. In order to develop a thin film as active or passive devices like waveguides, lasers, couplers, interferometers and MEMS, the functioning should be unaltered with external thermal effects. Changes in temperature dependent optical constants and band gap of semiconductors account for the applications in data storage, optical coatings and display industries to use the advantage of high sensitivity in the detection of the temperature induced small variations in film optical constants and thickness [Vinod et al. (2010)]. Therefore, it is very important to explore precise understanding and evaluate the thermal affects on optical properties with great accuracy for bringing out quantitative design aspects of devices. Lazziri and Jupille et al. measured reflection spectra of nanostructured silver thin films deposited on alumina substrate from 190 to 675 K in UV-Visible range [Lazzari et al. (2001)]. Temperature dependence of optical constants for silver thin films are

measured by spectroscopic ellipsometry in the range of 250-885 nm for temperature ranging from 300-650 K [Tripura Sundari et al. (2013)]. In semiconductors, Mg substituted ZnO thin films were grown and measured the absorption edge from the temperature range of 10-300 K [Chen et al. (2004)]. Reports on temperature dependent optical properties by various authors are listed in table 1.4.

Table 1.4: A brief review of literature on studies of temperature dependent optical properties of different materials and the properties analyzed.

Compound	Method used	Temperature range (K)	Optical parameters measured	Reference
$CH_3NH_3PbI_3$	Chemical solution deposition	77-297	Photovoltaic (light harvesting properties)	Yajie Jiang et al. (2016)
Gold thin films	Electron beam evaporation	308-773	Temperature dependent dielectric functions	Harsha Reddy et al. (2016)
TiO_2 thin films	Electron beam evaporation	293-533	Temperature dependent optical constants	Fan Zhang et al. (2013)
Silver thin films	Pulsed DC magnetron sputtering	300-650	Temperature dependent optical constants	Tripura Sundari et al. (2013)
Silver thin films	Pulsed DC magnetron sputtering	300-650	Thermo optic coefficients	Tripura Sundari et al. (2013)
2 mol% Mn doped $Pb_{0.5}Sr_{0.5}TiO_3$	Chemical solution deposition	80-500	Band gap shrinkage and Urbach band tail behavior	Yang et al. (2010)
$Bi_{3.25}La_{0.75}Ti_3O_{12}$	Chemical solution method	77-500	Band gap narrowing	Hu et al. (2007)
$Mg_xZn_{1-x}O$ thin film alloys	Reactive electron beam evaporation	10-300	Phase transition (cubic to hexagonal)	Chen et al. (2004)

As discussed, single crystal $LiNbO_3$ is predominantly being used industrially for versatile applications. But, utilization of thin films of the same as a substitute for single crystal offers great advantages in miniaturization of device structures in integrated circuits. Sapphire (Al_2O_3) single crystal possess similar crystalline structure as of $LiNbO_3$ with low refractive index which makes it suitable to grow high quality $LiNbO_3$ thin films for optical wave guiding and non linear optical studies. The unique advantages in using thin films rather than single crystal are doping foreign ions or atoms for enhanced properties, fabrication of multi layers and cost effective for industrial applications. Therefore, research is focused on developing $LiNbO_3$ thin films and studies their properties for miniaturized device structures. In the present work, $LiNbO_3$ thin films were deposited using Pulsed Laser technique and their temperature dependent linear optical properties as well as nonlinear optical properties using femtosecond laser are studied. These results are encouraging in using them for nonlinear and optoelectronic applications.

1.3 Introduction to dielectric materials and materials for fluorescence quenching based explosive sensing

In this section, the fundamentals of dielectric materials for resonator applications are given in detail. The variety of oxide materials used and their properties obtained are explained. Apart from that, the work done by researchers on fluorescence quenching based explosive sensing is also reviewed.

1.3.1   Dielectric materials for resonator applications

Dielectric resonators are polycrystalline ceramics which have high dielectric constant (ε_r), high quality factor (Qxf) and high frequency stability with temperature (temperature coefficient of resonant frequency τ_f close to 0 ppm/^{0}C) [Yih-Chien Chen et al. (2011)]. Fabrication of dielectric resonators into complex and net shaped components is of great interest in view of their potential applications. A few worth mentioning applications are cylinders and annular rings as dielectric resonators (DR) for oscillators, dielectric resonator antennas, rectangular substrates for microwave integrated circuit devices, circular discs as targets for deposition of thin films, radomes, impedance transformers, dielectric rod waveguides, housing and carriages for packaging, Low Temperature Co-fired Ceramic (LTCC) substrates etc. [Qingwei Liao et al. (2012), Di Zhou et al. (2014)]. Machining of dielectric resonator materials to their final dimensions or net shape is difficult and in some cases impossible since the conventionally processed samples possesses low toughness.
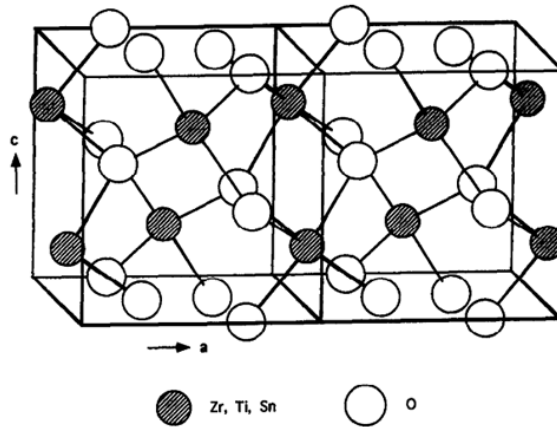
Fig. 1.3: Unit cell structure of Zr$_{0.8}$Sn$_{0.2}$TiO$_4$

In view of the above mentioned applications for dielectric resonators, ceramic compositions in the $Ba(Zn,Ta)O_3$ series, $Ba(Sn,Mg,Ta)O_3$ series, $(Zr,Sn)TiO_4$ series, $Ba_2Ti_9O_{20}$ series and others have been understood as suitable for realizing microwave dielectric resonators [Kugsun Honget.al(2001)]. Materials of the $(Zr,Sn)TiO_4$ series and the $Ba_2Ti_9O_{20}$ series have relatively large dielectric constants(ε_r) of 37 to 40 with $Q.f_0$ values of 50,000 to 60,000 [Tatsuya Ishikawa et al. (2002)]. Cheng Liang Huang et al. in "Improved high-Q microwave dielectric resonator using ZnO and WO_3 doped $(Zr_{0.8}Sn_{0.2})TiO_4$ ceramics" explained the effect of WO_3 along with ZnO addition on the microwave dielectric properties of ZST ceramics [Huang et al. (2001)]. Effect of various oxides of group-II elements on the ZST ceramics has been discussed in "Effect of BaO, SrO and MgO addition on microwave dielectric properties of ZST ceramics" [Pamu et al. (2007)]. It is evident from the above references that the dielectric ceramic composition ZrO_2-SnO_2-TiO_2 serves as an excellent material for application as microwave dielectric elements like dielectric resonators. But, in all of the above mentioned processes, DRs have been processed using conventional solid state reaction method where the scope of processing the DRs in different shapes is limited. In general, dielectric resonators of cylindrical shapes can be prepared using hydraulic presses of large tonnage and using expensive dies.

Fabrication of ceramic components in desired shapes for application of wireless communication is reported in "Gel casting of ceramic components for wireless communications" [Xiong et al. (2005)]. In this article, the manufacture of green bodies of complex shaped ceramics like BaO-Nd_2O_5-TiO_2, BaO-La_2O_3-TiO_2, $MgTiO_3$-$CaTiO_3$ system using a slurry based technique is reported. But, in this

work, the dielectric properties like quality factor and τ_f are quite inadequate when using the slurry based process, making the process limited in applications.

The major hurdle in using ceramic materials for most applications is shaping into the desired dimensions and machining into net shape because of their brittle nature. Melt casting of ceramic is not possible because of their remarkably high melting points. Machining of ceramics to their final dimensions by conventional methods is extremely laborious, time consuming and often impossible or limited to simple geometries. Samples prepared by conventional methods are often brittle and possess relatively inferior mechanical properties. M. A. Janney, Stephen D. Nunn, Claudia A. Walls et al. in "Gel casting, The Handbook of Ceramic Engineering" introduced the processing of ceramic parts in thick to thin sections using a slurry based technique [Janney et al. (1998)]. In this article, complex shaped ceramic parts like turbine rotors and radomes have been fabricated. The use of several monomer systems along with the advantages of different mold materials is discussed. In the present study, the slurry based technique as mentioned above is adopted and modified to process ZrO_2-SnO_2-TiO_2 (ZST) ternary systems in such a way as to retain their properties required for sensitive applications like DR where the τ_f is to be close to zero ppm/^{o}C. ZST is a multi-component oxide and its dielectric properties are extremely sensitive to composition, purity and density. Hence the slurry based processes as discussed in the literature cannot be adopted directly.

Wang et al. prepared the parent compound $ZrTiO_4$ ceramics with additives such as ZnO, CuO and Y_2O_3 [Wang et al. (1997)]. The microstructure and microwave dielectric properties are highly sensitive to the presence of additives and processing conditions. $(Zr_{0.8}Sn_{0.2})TiO_4$ powders do not readily sinter by solid

state diffusion. It is difficult to fully densify ZST ceramics without sintering aids if the powder is prepared by the mixed oxide route [Sebastian et al. (2008)]. Even sintering at a high temperature such as 1600 ^{0}C is inadequate to give good densification. Hence ZnO is usually added as a sintering aid [Sebastian et al. (2008)]. The ZnO additive forms a liquid phase at the grain boundaries during sintering thus helping densification through rapid transport of matter through liquid phase and considerably lowering the sintering temperature. Sintering aids such as ZnO, NiO, CuO, V_2O_5 and Bi_2O_3 [Michiura et al. (1995)] can be added to $Zr_{0.8}Sn_{0.2}TiO_4$ to aid the synthesis by solid state reaction method through the formation of a liquid phase. Copper oxide and Vanadium pentoxide are flux formers and hence they are added to lower the sintering temperature of $Zr_{0.8}Sn_{0.2}TiO_4$ ceramics.

There is a lot of literature available describing the application (usage) of dielectric resonators in filters, antenna, combiners, duplexers, oscillators and many more [Ioachim et al. (2006)]. All these applications need different shape and sizes of dielectric resonators. But, till now no literature has been published describing the development of a shaping technique for molding dielectric resonators in desired shapes. The final properties are highly sensitive to the composition which can alter at high temperatures and hence a low temperature processing technique is very much desired. In addition, lower temperature processes helps in minimizing capital investment while scaling up to industrial level. ZST needs secondary impurities/ sintering aids to sinter to full density at relatively low temperatures. Hence a method needs to be developed wherein uniform distribution of sintering aids is possible, especially when processing large quantities. Therefore, in order to obtain net shaped ceramic components

with improved mechanical properties and appropriate microwave dielectric properties, slurry based inexpensive and room temperature shaping technique is developed as part of this study, where the final density can also be tailored with a uniform distribution of sintering aids.

Dielectric resonators of different compositions have been successfully reported so far. The microwave dielectric properties of the reported compositions were very good and high enough to use them as for microwave device applications. But, very few literatures are available on the processing of dielectric resonators in complex shapes. In the present thesis, we give a detailed procedure for fabricating complex shaped dielectric resonators retaining their microwave dielectric properties. In addition, we processed porous $Zr_{0.8}Sn_{0.2}TiO_4$ substrates from gel casting and used the same for explosive sensing applications. Detailed literature on dielectric resonator materials and their properties are presented in table 1.5.

Table 1.5: Reports in literature on development of dielectric resonator compounds and their properties

Material	Properties / Application	References
$(Zn_{1-x}(Li_{2/3}Ti_{1/3})_x)_2TiO_4$ (x = 0–1)	ε_r=16 to 28, Q×f=1,60,000 GHz/Resonator	Jian Zhang et al. (2016)
$(Mg_{1-x}Zn_x)Ti_{1.1}O_4$	ε_r=16 to 20, Q×f= 1,41,000 to 2,10,700 GHz / Resonator	HuidongXie et al. (2016)
$ZnNb_2O_6$ with $BiVO_4$ additive	ε_r = 26, Q×f = 55,000 GHz / LTCC substrates	Xuewen Jiang et al. (2015)
$Ni_{1-x}(Zn_{1/2}Zr_{1/2})_xW_{1-x}Nb_xO_4$	ε_r = 12 to 16, Q×f = 23,400 to 53,350 GHz / Resonator	S. D. Ramarao et al. (2015)

Sr_3WO_6	Temperature coefficient of capacitance (TCC)= 6156.52 to 471.73 ppm ^{o} C^{-1} / microwave dielectric filter	D. V. M. Paiva et al. (2016)
$Sr_2LaAlTiO_7$	ε_r = 26, Q×f 1,10,850 GHz / Microwave dielectric filter	Bing Liu et al. (2016)
$(Ba,Sr)TiO_3$	880<ε_r<990 570<Q×f<1150 GHz / Phase shifters and tunable filters	Zhe Song et al. (2015)
Pure $Ba(Zn_{1/3}Ta_{2/3})O_3$	ε_r=30, Q×f=119 THz / Resonator	Bashaiah Sindam et al. (2015)
$xBi(Fe_{1/3}Mo_{2/3})O_4–(1-x)BiVO_4$	ε_r=75, Q×f= 11,500 GHz / microwave integrated capacitive devices, such as filters, antennas,	Di Zhou et al. (2012)
$Li_2O–MgO–BO_2$ system	ε_r = 12 to 16, Q×f = 1,50,000 GHz / microwave devices	Haitao Wu et al. (2016)
$(1–x)Ba(Mg_{1/3}Nb_{2/3})O_3–xBaSnO_3$	ε_r = 29, Q×f = 90,000 GHz / Resonator	Jie Zhang et al. (2015)
$(1 – x)BiVO_4–xYVO_4$ ($x \leq 0.65$)	ε_r = 45, Q×f = 14000 GHz / multiplexer and EMI filter	Di Zhou et al. (2015)
$(1-x)$ $MgTiO_3-xMg_{2.05}SiO_{4.05}-0.06CaTiO_3$	ε_r=15.4, Q×f=72,705 GHz / New composition for resonator	Hao Li et al. (2015)
$(Bi_{1–x}Ce_x)VO_4$ (x = 0.10, 0.20,0.25, 0.30, 0.40, 0.60)	ε_r=47, Q×f=18000 GHz / LTCC substrates	Di Zhou et al. (2014)
$NaAgMoO_4$	ε_r = 7.9, Q×f = 33,000 GHz / LTCC substrates	Zhou Di et al. (2014)
$[(Li_{0.5}Ln_{0.5})_{1–x}Ca_x]MoO_4$ (Ln = Sm and Nd)	ε_r = 11, Q×f=18,695 GHz / LTCC substrates	Hai Hong Xi et al. (2014)
BaV_2O_6	ε_r = 11, Q×f = 42,790 GHz / Ultra low temperature co-fired ceramic substrates	U A Neelakantan et al. (2014)
$(Sr_{1–x}Ca_x)La_2Al_2O_7$	ε_r = 20, Q×f = 1,35,400 GHz / Resonator	Lie Yi et al. (2014)
$Sr_2LaAlTiO_7$	ε_r = 26.5, Q×f = 1,10,850 GHz / New composition for resonator	Bing Liu et al. (2013)

$Ni_{0.5}Ti_{0.5}NbO_4$	ε_r=56, Q×f=21,000 GHz / 1–10 GHz civil mobile communication apparatus	Qingwei Liao et al. (2012)
$(Mg_{1-x}Zn_x)_{1.8}Ti_{1.1}O_4$ (x = 0.03–1.00)	ε_r=15 to 20, Q×f=1,41,000 to 20,000 GHz / dielectrics for Ultra high frequency applications	Cheng Liang Huang et al. (2012)
$(1-x)Li_2TiO_3–xZnO$ (x = 0.1–0.5)	ε_r=23, Q×f=99,800 GHz / LTCC substrates	Cheng-Liang Huang et al. (2012)
$Nd(Mg_{0.5}Sn_{0.5})O_3$	ε_r=19, Q×f=43,300 GHz / filters and antennas	Yih-Chien Chen et al. (2011)
$Bi(V_{0.008}Nb_{0.992})O_4$	ε_r=40, Q×f=18,500 GHz / LTCC substrates	Di Zhou et al. (2009)
BaO, SrO and MgO addition in $Zr_{0.8}Sn_{0.2}TiO_4$	ε_r=36, Q×f=38,000 to 60,000 GHz / Resonator	D.Pamu et al. (2008)
$0.95MgTiO_3–0.05CaTiO_3$	ε_r=20, Q×f=65,000 GHz / Microwave dielectric filter	Cheng-Liang Huang et al. (2006)
$Ba(Mg_{1/3}Ta_{2/3})O_3$	ε_r=25, Q×f=1,20,500 GHz / Resonator	Kuzhichalil P. Surendran et al. (2005)

1.3.2 Fluorescence quenching based explosive sensors-Materials being used

The detection of explosive molecules is of prime concern for military operations, homeland security and to control environmental toxicity. Although the technology is well developed to detect explosives, sensing trace level explosives based on nitramines, nitro aromatic, nitro alkanes, peroxides and nitro ester is becoming prime concern for security purpose [Lourdes Basabe-Desmonts et al. (2007)]. In addition, sensitive and cost effective detection could provide rapid warning to the environmental hazard and offer appropriate feed-back in remediation of contaminated sites. Optical based methods using infrared or visible light are found to be efficient for explosives detection [Lourdes Basabe-

Desmonts et al. (2007)]. Examples like Surface Enhanced Raman Scattering (SERS) is well advanced, non destructive, cost effective and higher sensitive technique for detection of explosives by identifying characteristic vibrational modes [Krishna G Podagatlapalli et al. (2013)]. In addition, fluorescence based methods provide good sensitivity because the emission signal is visible and is measured with a low background emission.
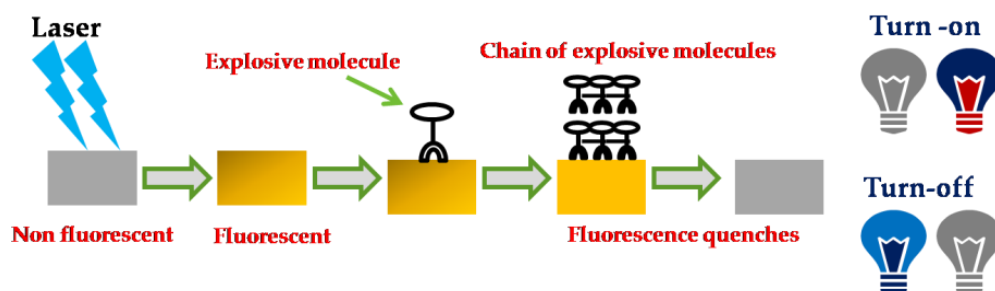
Fig. 1.4: Mechanism explaining the fluorescence quenching based explosive sensing.

The mechanism of fluorescence quenching is based on photo induced electron transfer from excited fluorescent molecules to analytes [Hana Woo et al. (2013)]. Diffusion of analyte molecules take very long times through dense matrix and therefore sensing performance will be decreased. Thin films (<100 nm) can be used for the same where the reliability and reproducibility are difficult because of the low intensity in fluorescence signal. Therefore, in this study work is focused on preparing micro scale and nanoscale porous materials for explosive detection as the transport rate of analyte through porous network and the sensitivity of detection are enhanced. Another added advantage of porous structures is that the sensitivity and discrimination of analyte can be engineered by tuning the porous structures accordingly.

The emerging progress in wireless communications and wireless sensor networks demands for materials that can be miniaturized into integrated components [Sebastian et al. (2008)]. Typically, many microwave dielectrics have been proposed and are used as potential candidates for communication purposes. On the other hand, wireless sensors play a significant role in instrumentation. In specific, sensors for explosive molecules take a major lead in the field of security and preventing environmental hazards [Lourdes Basabe et al. (2007), Patrick et al. (2012)]. Therefore, there is a need to establish and design new materials for wireless sensors that expands the scope and range of applications [Jennifer et al. (2013)]. The dielectric ceramics are materials that can be fine tuned for variety of properties. In particular they give resonances in the microwave frequencies. Depending on the loss factor, the Q value offered by these resonances could be quite high (in the range of 5000- 10000 at about 10GHz). Hence perturbations brought in by the adsorption of explosive molecules by these resonators or a sensor layer coated over it result in considerable change in their Q value as well as shift in resonance frequency which can be measured using microwave instrumentation.

In general the onsite detection of explosive molecules should satisfy explicit requirements: high sensitivity, low response time and room temperature sensing [Meaghan et al. (2009)]. Most of the organic and inorganic fluorescent materials used for explosive sensing should satisfy the above mentioned criteria. Organic polymers like pyrene, pyrene doped polyethersulfone (Py-PES), mesoporous ormosil thin films, poly (phenyleneethynylene) (PPES) contains electron-rich aryl rings which form π-π interactions to bind the electron-poor nitroaromatics. Inorganic polymers include polysilanes, poly (3,3,3-trifluoropropylmethysilane)

(PTFPMS) possess σ-σ* delocalization along Si-Si backbones to confine electrons similar to organic conjugated polymers [Meaghan et al. (2009)]. Apart from polymers, porous dielectric silica nanotubes, TiO_2 based nanostructures, nanocrystalline diamond have great deal of interest because of their inert nature, active surface functionalization and hydrophilicity [Adem Yildirim et al. (2011)]. The development of new dielectrics as fluorescent indicators in explosive sensing is needed. Moreover, microscale or nanoscale porous materials are being used in explosive detection to support fluorescent indicators as the porous structures allows easy diffusion of analyte to the indicator.

In this context, $Zr_{0.8}Sn_{0.2}TiO_4$ (ZST), a well known dielectric resonator is found to be fluorescent and porous substrates of ZST can be fabricated using gel casting technique [Anil Tumuluri et al. (2016)]. Advantages include reusability, easily reproducible and inexpensive because of its high mechanical strength and ease in tuning porosity from μm to nm levels [Christoph Brandes et al. (2014)]. Apart from porous substrates the dielectric resonators also could be shaped by the gel casting process. This gives rise to a new opportunity of gel casted ZST being used for explosive detection by two alternate methods. One is by noting the change in Q value and resonant frequency of the ZST based dielectric resonator coated with a sensitive layer tuned to absorb the target explosive molecules. The other one is by employing the flourescent quenching with absorption of selected explosive molecules into the pores of porous gel casted ZST as discovered in this study. Since the same material (ZST) and process (gel casting) offers two alternate routes for explosive detection, by simultaneously employing both of them, the reliability of the detection and identification of species can be greatly enhanced. Hence in this study the development of gel

casting process for both dielectric resonator application and for porous substrate application are emphasized.

Till date, $Zr_{0.8}Sn_{0.2}TiO_4$ (ZST) is well investigated for its microwave dielectric properties so as to use them in microwave applications such as resonators, antennas, oscillators and filters. In the present study, usage of fluorescence from $Zr_{0.8}Sn_{0.2}TiO_4$ substrates for analyte sensing and its porosity for analyte diffusion were studied. The emission peaks are observed to be the same for porous and nonporous ZST. In table 1.6; the explosive molecules recognized by various materials are given in detail.

Table 1.6: Reported literature on fluorescence quenching for detection of nitro compounds using different materials and their corresponding quenching efficiencies.

Material	Molecule detected	Quenching efficiency/minimum detectable concentration	Reference
Nph-An (anthracene and 1, 8- Naphthalimide units)	2, 4, 6-TNP	----/ 1.40×10-7 M	Hongwei Ma et al. (2016)
Fluorescent Carbon dot	4C-2,6DNA, 6C-2,4DNA, 2,5DC-4NA and 305 2,6DC-4NA	----/ 2 μM	Bruno B. Campos et al. (2016)
Aggregate Induced emission luminogen functionalized nanomaterials (Mesoporous silica nanoparticles)	2,4-DNT vapours	75 to 80% / ----	Dongdong Li et al. (2015)
Phenol red as fluorophore in a poly(vinyl alcohol) (PVA) membrane	2,4,6-TNT, 2,4-DNT,4-NT,2,4,6-TNB,NB	----/1.0 μM	Ali Reza Zarei et al. (2015)
Quantum dots ZnS:Mn2+@allylmercaptan	TNT, TNP, DNT and NB	TNT-47%/---- TNP-52%/----	Min Bai et al. (2015)

Mesoporous Ormosil Thin Films	TNT, DNT and NB	TNT-68%/---- DNT-88%/---- NB-67%/----	Pinar Beyazkilic et al. (2014)
Conjugated porous polymer	TNT	----	Jennifer L. Novotney et al. (2013)
pyrene-doped polyethersulfone (Py-PES) polymer	DNT, TNT,NB, AN, Toulene, Raspberry, Benzene, Piperidine, Piperazine	----	GokcenBirlikDemirel et al. (2013)
Silica Nanotubes	TNT, DNT and NB	TNT-28%/---- DNT-33%/---- NB-7.5%/----	AdemYildirim et al. (2011)
Conjugated polycarbazole polymer	TNT and DNT	TNT-87%/---- DNT-77%/----	HeranNie et al. (2010)

1.4 Aim and objective of this study

This thesis is broadly motivated by the idea of developing LN thin films for nonlinear as well as for optoelectronic applications and porous ZST for explosive sensing based on fluorescence quenching.

The main objectives of this study are

1. To obtain polycrystalline and oriented $LiNbO_3$ thin films by Pulsed Laser Deposition.

2. To study the nonlinear optical properties of LN thin films from Z scan. To study the effect of orientation and defects present in LN on nonlinear absorption, nonlinear refractive index and nonlinear susceptibility in detail.

3. To investigate the temperature dependent linear optical properties of LN thin films for optoelectronic applications.

4. To fabricate $Zr_{0.8}Sn_{0.2}TiO_4$ ceramics in near net form by using gel casting technique. The microwave dielectric properties of ZST are to be measured using vector network analyzer in order to examine the quality of ZST for dielectric resonator applications.

5. To fabricate porous ZST substrates were fabricated using gel casting technique. The obtained substrates are to be used for nitro explosive sensing with fluorescence quenching method. In the present study, porous ZST substrates are able to sense TNT, RDX and CL 20 efficiently and their mechanism is explained.

1.5 Outline of the thesis

Chapter 1: Introduction

This chapter reviews the basics of Lithium niobate (LN) and $Zr_{0.8}Sn_{0.2}TiO_4$ and their applications. The difficulties aroused in the deposition of LN are discussed. In addition, usage of LN in single crystal form for versatile applications is given in detail. The drawbacks in using single crystals and advantages of thin films for miniaturization are discussed. The literature on the studies of nonlinear optical properties of LN thin films is reviewed. There are many reports on second order nonlinearity in $LiNbO_3$ crystals. But, the third order nonlinearity in $LiNbO_3$ thin films is not well studied and reports on third order nonlinearity are tabulated. In addition, ferroelectric thin films have potential applications in optoelectronic devices and needs temperature dependent optical properties for practical applications. Therefore, linear optical

properties of LN thin films are studied with change in temperature so that it can be used for optoelectronic applications.

$Zr_{0.8}Sn_{0.2}TiO_4$ ceramics have potential applications as dielectric resonators, antennas and filters. Gel casting technique is explained in detail where the production of dielectric materials in arbitrary near net shape can be achieved for industrial applications. The quenching concentration and their mechanism for explosive sensing are explained.

Chapter 2: Experimental techniques and characterization

In this Chapter, the main experimental techniques and characterization tools used in this study are introduced. The fundamentals of vacuum technology and deposition techniques used for the synthesis of $LiNbO_3$ thin films as well as detailed procedure for gel casting process to fabricate porous ceramics are discussed. Pulsed laser deposition is used to get $LiNbO_3$ film with Al:ZnO as underneath layer. The structural details of the films were analyzed using grazing incidence X-ray diffraction and RAMAN spectra. The morphology of the same was recorded from FE-SEM and AFM to explain the roughness, grain shape and size. The transmission spectra in the wavelength range of 190-2500 nm were recorded using UV-Visible spectrophotometer. Direct and indirect band gap of $LiNbO_3$ thin films were extracted from the transmission spectra. Photoluminescence spectra were plotted with an excitation wavelength of 355 nm. Z scan technique is used to get nonlinear optical properties through which nonlinear absorption coefficient, nonlinear refractive index and nonlinear susceptibility were extracted. Finally, the chapter focuses on the principles of characterization techniques like GI-XRD, FE-SEM, RAMAN, photoluminescence,

Atomic Force Microscopy (AFM), UV-Visible spectrophotometer, Z scan and Vector Network Analysis which are explained in detail.

Chapter 3: Structural, linear and nonlinear optical properties of LiNbO$_3$ thin films

In this Chapter, LiNbO$_3$ thin films deposited by means of Al:ZnO as intermediate layer using pulsed laser deposition and their structural details using GI-XRD are discussed. The films were found to be polycrystalline, (110) oriented and (300) oriented while deposited on fused silica, Al:ZnO/fused silica and Al:ZnO/quartz substrates respectively. The films evidenced transparency of above 80% in visible and near IR region. The polycrystalline and (300) oriented LiNbO$_3$ films demonstrate reverse saturable absorption and transits to saturable absorption in case of (110) oriented LiNbO$_3$ film. Nonlinear optical properties measured from Z-Scan gives the detailed insight into the nonlinear absorption coefficient, nonlinear refractive index and nonlinear susceptibility. The two photon absorption is attributed to the indirect transition via intermediate defect levels which relates to the structural asymmetry and significant change in band gap also contributes to the nonlinearity in LiNbO$_3$ thin films. The large nonlinearity in refractive index is the result of electronic polarization influenced by ferroelectricity. The third order nonlinearity of all the films are in the order of 10^{-9}esu which is three orders of magnitude greater than the single crystal z-cut LiNbO$_3$. The high optical transparency and third order optical nonlinearity show that LiNbO$_3$ thin films are a promising candidate for nonlinear photonic devices.

Chapter 4: Temperature dependent optical properties of LiNbO$_3$ thin films using UV-Visible spectrophotometer for optoelectronic applications

This chapter comprises the details of temperature dependent linear optical properties of LiNbO$_3$ thin films of various thicknesses using UV-Visible spectrophotometer. The optical constants like absorption coefficient, refractive index and optical band gap of LiNbO$_3$ thin films were extracted from the transmittance spectra in the temperature range of 308-493 K. It is found that the transmittance decreased with increase in temperature from 85 to 57% in the visible range and the optical band gap also got red shifted with increasing temperature from RT to 493 K. The band gap is found to decrease from 3.9 to 3.7 eV where the shift can be attributed to the presence of polaronic absorption. The asymmetric absorption humps at lower energies are due to the 1.0 eV (Nb_{Nb}^{4+}), 1.6 eV (Nb_{Li}^{4+}) and 2.5 eV (both $Nb_{Nb}^{4+}:Nb_{Li}^{4+}$ and O$^-$) polaronic peaks which affect the linear and nonlinear optical properties of LiNbO$_3$. The band gap narrowing and decrease in transmittance favors LiNbO$_3$ thin films for practical applications in some optoelectronic devices.

Chapter 5: Synthesis and forming of Zr$_{0.8}$Sn$_{0.2}$TiO$_4$ ceramics using gel casting and their microwave dielectric properties

This chapter includes the synthesis and forming of dielectric resonators through slurry based route involving organic/inorganic carrier medium. The main emphasis is on optimizing the conditions to get Zr$_{0.8}$Sn$_{0.2}$TiO$_4$ ceramics. An inexpensive polyethylene mould is used for the fabrication of dielectric resonators. This is taken as critical requirement for the synthesis of porous ZST for fluorescence quenching based explosive sensor realization. Zr$_{0.8}$Sn$_{0.2}$TiO$_4$ ceramics processed using this technique were sintered at 1400 °C and exhibited

desirable microwave dielectric properties of ϵ_r=37, Qxf=32000 and τ_f=+6 ppm/⁰C. The obtained microwave dielectric properties for $Zr_{0.8}Sn_{0.2}TiO_4$ using gel casting are enough to use them for microwave dielectric resonator based applications. The advantages of this technique include low cost, desirable and complex shapes with fine surface finish and adaptable to industrial applications.

Chapter 6: Porous $Zr_{0.8}Sn_{0.2}TiO_4$ substrates: Fluorescence quenching based detection of nitro explosives

In this chapter, porous $Zr_{0.8}Sn_{0.2}TiO_4$ were made using gel casting with different pore forming agents like baking soda, ethyl cellulose and starch. The substrates have multi emission peaks in green, orange and red regions with an excitation wavelength of 355 nm. When an analyte of TNT, RDX and CL 20 were in contact with ZST, the fluorescence emission got quenched with time as well as with analyte concentration. The quenching efficiency of each analyte is discussed in detail. Analyte diffusion through porous matrix and the sensing performances are analyzed. TNT is found to be an effective analyte for diffusion through porous $Zr_{0.8}Sn_{0.2}TiO_4$ substrates. These porous substrates exhibit fast, sensitive, inexpensive and highly selective fluorescence quenching. The quenching efficiencies varied for CL 20, TNT and RDX. The materials developed in this study have extensive potential in sensing applications due to the ease in fabrication, high mechanical strength and tenability in porous structures.

Chapter 7: Conclusions and Scope for Future work

The main conclusions of the present thesis are presented in this chapter. Some possibilities for extending this work in the future are also discussed. The most important contributions of the thesis are

1. Detailed understanding of the LiNbO$_3$ thin films with Al:ZnO as intermediate layer using pulsed laser and their linear and nonlinear optical properties.

2. Demonstration of the temperature dependent optical constants of LiNbO$_3$ thin films.

3. Fabrication of Zr$_{0.8}$Sn$_{0.2}$TiO$_4$ ceramics in various geometries using gel casting and study of their microwave dielectric properties.

4. Porous Zr$_{0.8}$Sn$_{0.2}$TiO$_4$ substrates exhibit dominant green and red emissions which quenches with different analyte concentrations. The quenching efficiency is found to be good enough to use these porous substrates for nitro explosive sensing.

Chapter 2

Experimental and characterization techniques

In this Chapter, techniques used for the synthesis of thin films and gel casting process for fabrication of porous ceramics were explained in a broad manner. In addition, the principle of characterization techniques like GI-XRD, FE-SEM, RAMAN, photoluminescence, Atomic Force Microscopy (AFM), UV-Visible spectrophotometer, Z-scan and Vector Network Analysis were explained in detail. This chapter introduces the various thin film deposition techniques and working principle of characterization techniques involved in the present work.

2.1 Thin film deposition and techniques

Thin film science and technology plays a significant role in the development of devices. Applications of these devices include but not limited to solar cells, energy harvesting, optical devices, batteries, sensors and super capacitors [Norbert Kaiser et al. (2002)]. What not, most of the technology is based on thin films and their enhanced properties. Thin films of metals, semiconductors and insulators have wide ranging applications from sensors to display devices [Abliz Yimit et al. (2005)]. Depending on the material characteristics, properties of thin films vary from their bulk counterpart [Li-ping Wang et al. (2013)]. A film can be considered as thin, as long as its surface properties are different from their bulk characteristics. In general, thin film properties vary depending on the thickness which extends from nanometer to micrometer, nature of the substrate and deposition conditions. Thin films possess larger surface to volume ratio and hence the properties of thin films depend on the surface structure and its modifications. In general, thin films can be modified in terms of its surface morphology, porosity, roughness and crystallite size. The final properties can be either enhanced or degraded by tuning these parameters during deposition. Interpretation of thin film growth and their properties is essential in developing new thin film based devices with higher efficiency.

2.1.1 Deposition techniques

Depending on the nature of deposition, thin film growth techniques can be classified into (i) Chemical Vapor Deposition (CVD) (ii) Physical Vapor Deposition (PVD). In CVD technique, gas/liquid phase of the target material is allowed to undergo reaction during the deposition process. In PVD, the target material is vaporized either through thermal or a thermal vaporization of target

material to get thin film condensed onto a substrate [Donald M. Mattox et al. (1998)]. The classification of thin films is based on the nature of deposition and is depicted in fig. 2.1.

Thin film deposition techniques

Physical vapor deposition

Chemical vapor deposition

Thermal PVD
1. Thermal evaporation
2. Pulsed laser deposition
3. Electron beam deposition
4. Molecular beam deposition

Athermal PVD
1. DC Magnetron sputtering
2. RF Magnetron sputtering

1. Plasma enhanced CVD
2. Vapor phase epitaxy
3. Microwave plasma assisted CVD
4. Ultrahigh vacuum CVD

Fig. 2.1 Classification of thin film deposition techniques

In the present work, LiNbO$_3$ thin films were deposited using Pulsed Laser Deposition (PLD) technique and electrodes (Au and Pt) were coated using RF magnetron sputtering. For that reason, the mechanism behind the pulsed laser deposition and RF magnetron sputtering are explained in detail.

2.1.2 Pulsed Laser Deposition technique

Pulsed laser deposition technique is a well established PVD procedure for thin film growth especially for oxide materials. In PLD, a high energy laser is focused onto the target material to generate thermal energy and thus vaporizes the material and allowed to condense onto a substrate as a thin film. The growth and quality of film depends on number of internal factors including choice of substrate, substrate temperature, partial pressure, relative kinetics of the constituents within the plume and external factors such as laser fluence, laser

wavelength and pulse width [Aziz et al. (2008)]. Variety of lasers were applicable for the thin film growth ranging from mid infrared e.g. CO_2 laser (λ=10.6 μm) through infrared and visible (e.g. Nd:YAG laser where fundamental and second harmonic wavelengths are 1064 nm and 532 nm respectively) and down to ultraviolet operating at different wavelengths e.g. 308 nm (XeCl), 248 nm (KrF), 193 nm (ArF) and 157 nm (F_2) [Michael N. R. Ashfold et al. (2004)]. Currently, most of the PLDs are using excimer lasers with UV wavelength [Costas et al. (2009)]. The deposition of thin films will be performed either in reactive background gas atmosphere such as oxygen and nitrogen or inactive gases like argon. The complete PLD process can be divided into three steps and is as follows:

1. Laser-target interaction
2. Plume expansion after laser irradiation
3. Condensation of plume constituents on a substrate and subsequent film growth

Fig. 2.2 shows the PLD process schematically and PLD chamber along with laser used in the present work. In the present work, an Excimer laser (Coherent Compex Pro 102F) operating at a wavelength λ=248 nm is used. The spherical deposition chamber (Excel Instruments, Mumbai) is fitted with a turbo molecular pump (Pfeiffer, Germany) and a base vacuum of 10^{-6} mTorr is achieved prior to deposition. The chamber has substrate heater which can reach 800 °C with resistive heating. In addition, chamber is equipped with a target carousel which can accommodate six targets allowing for multilayer deposition without disturbing vacuum. The substrate holder is held parallel to the target material to

get the maximum plume condensed onto substrate. The substrate holder to target distance is fixed to be 5 cm in the present study.
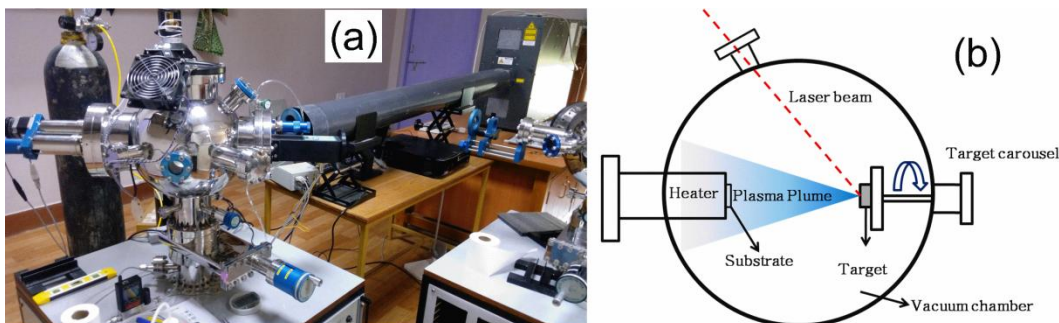
Fig. 2.2 (a) Chamber of Pulsed Laser Deposition process (b) Schematic picture (top view) of PLD

PLD is chosen to deposit $LiNbO_3$ thin films because of its ease in deposition and reproducibility in stoichiometry, since Li is a lighter element and its evaporation is a major issue in preserving stoichiometry and for enhanced properties [Christen et al. (2008)]. Several reports on $LiNbO_3$ thin films using sol-gel, RF magnetron sputtering and pulsed laser deposition are available till now.

2.1.3 RF magnetron sputtering

In a basic sputtering process, a target material is bombarded with highly energetic ions, typically inert gas argon (Ar^+) ions as shown in fig. 2.3. The forceful collision of inert gas ions with the source (target) material causes the removal of target atoms to eject out and condense onto the substrate [Donald M. Mattox et al. (1998)]. The deposition conditions were to be optimized in such a way that the stoichiometry of thin film and target material is to be preserved. The basic procedure looks simple but the experimental process is quite complex. Metals, semiconductors and insulators were successfully deposited using RF magnetron sputtering. Sputtering process is driven by the momentum exchange

between the highly energetic ions and atoms in the target material due to collisions. In the present work, RF magnetron sputtering is used for the electrode (Au) deposition.
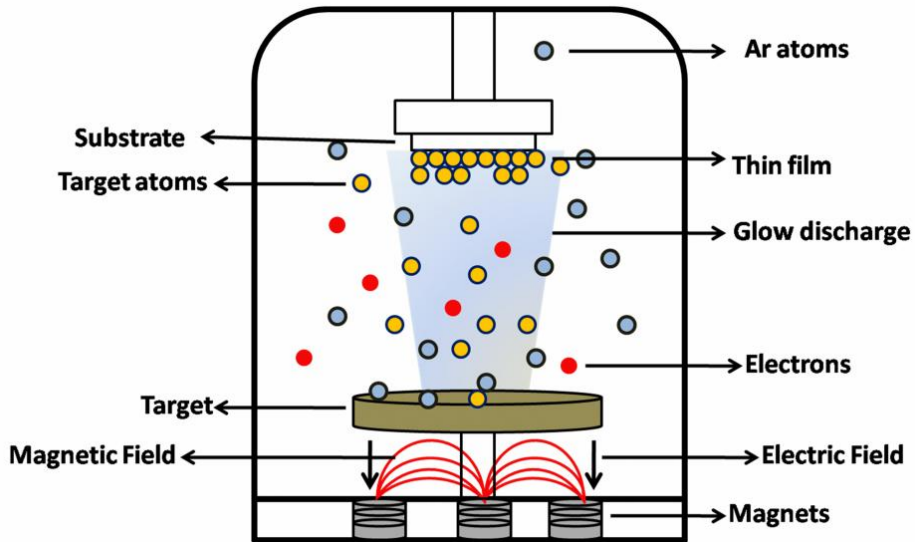
Fig. 2.3 Schematic representation of RF magnetron sputtering process inside the chamber (side view)

2.2 Gel casting technique for $Zr_{0.8}Sn_{0.2}TiO_4$

Gel casting is a well studied and widely applicable process to cast different complex shaped ceramics and alloys. In this technique, powder will be dispersed in a polymer matrix along with a dispersant to form solids loading slurry after which it transforms into a gel to cast in desired moulds followed by de-molding, de-binding and sintering [Narottam et al. (2012)]. This technique cannot be limited to ceramics as the processing additives are all organic and leave no cation impurities behind in the fired part. Mostly, researchers have adapted gel casting for its advantages like high mechanical stability, ease in machining, reproducibility and cost effectiveness. Typical gel casting technique is based on the polymer chemistry to certain extent. The heart of the technology is the use of

an aqueous organic monomer solution that can be polymerized to form a strong cross linked polymer solvent gel.

Fig. 2.4 Photograph of planetary ball mill used in the present study

The monomer solution provides a low viscosity medium after suspension of ceramic powder along with dispersants to form a highly solids loaded slurry. Methacrylamide (MAM) and Methylenebisacrylamide (MBAM) are the best preferred monomer and cross linker respectively. Ammonium per sulfate (APS) is the free radical initiator and tetramethylenediamine (TEMED) is the catalyzer to accelerate the polymerization and cross linking reaction [Gilissen et al. (2000)]. Thus formed slurry is to be poured into moulds of desired shapes. The monomer solution after cross linking forms a polymer solution which immobilizes the ceramic particles in the shapes defined by the mould. The final product constitutes of 15-20 wt.% of polymer which can be removed during the drying or de-binding stage with remnants of 2-4 wt.% which can be removed during the sintering stage.
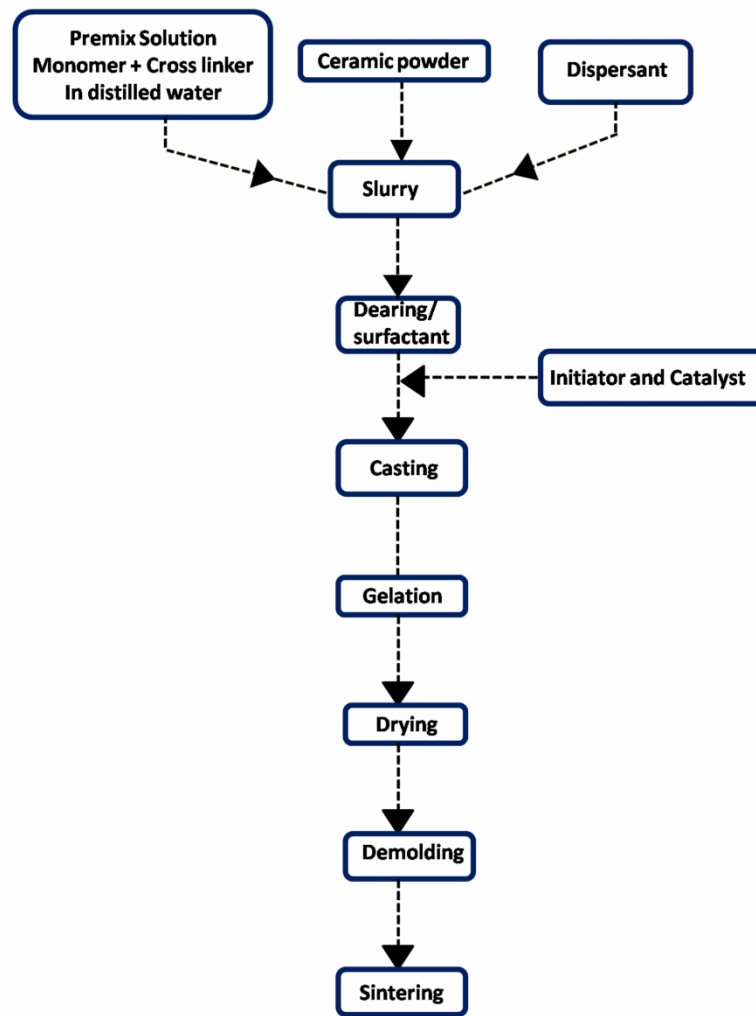
Fig. 2.5 Flowchart explaining the typical gel casting procedure

In general, the strength of the gel and the gel cast ceramics increases with increasing monomer concentration in solution and with increasing ratio of cross linker to monomer ratio. Machinability can be further increased with the addition of plasticizers like ethylene glycol and glycerin. The critical aspects of successful gel casting are selection, fabrication and the usage of mould. The most commonly used mould materials are aluminum, glass, polyvinylchloride (PVC),

polysterene (PS) and polyethylene (PE). Each of the materials has their own advantages and disadvantages like mould release, fabrication and ungelled layers segregating at the surface of the gelled parts. General procedure for gel casting is clearly mentioned in fig. 2.5.

2.3 Characterization tools

2.3.1 X-ray diffraction

The X-ray diffraction (XRD) is a non-destructive and vital technique to analyze the crystalline phases and orientation of solid materials. Diffraction effects are observed when X-rays impinge on the periodic features with geometrical variations corresponding to length scale of the wavelength of the radiation. In amorphous crystals, atoms are placed randomly whereas in crystalline solids atoms will be periodic with inter atomic distance on the order of 100 pm or 1 Å. The wavelength of the incident light has to be of the same order as the spacing of the atoms, thus X-rays are used for this purpose. In 1913, Sir W.L.Bragg and W.H.Bragg gave an empirical relation for diffraction of X-rays from crystal planes,

$$n\lambda = 2d \sin\theta \tag{2.1}$$

where n is the order of diffraction, λ corresponds to the wavelength of incident X-rays (λ=1.5406 Å for Cu K$_\alpha$ radiation), θ is the angle of diffraction and d is the inter-planar spacing of the crystal lattice (fig. 2.6). The above equation is known as the Bragg's equation and the value of θ for which equation (2.1) is satisfied is called the Bragg's angle.
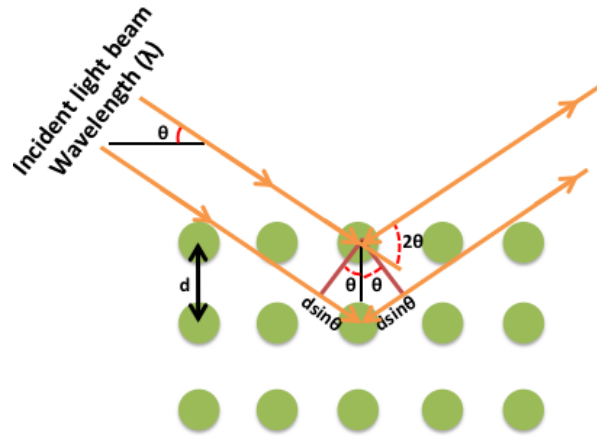
Fig. 2.6 Constructive interference of X-ray waves to satisfy Bragg's law

In the present work, Bruker X-ray diffractometer (Bruker D8 Discover with Cu K_α=1.5405 A° source) was used to examine the crystallographic structure of the deposited LiNbO₃ and Al:ZnO thin films. The diffracted peaks pertaining to the (hkl) crystal planes are indexed and matched with the standard available data in JCPDS card for LiNbO₃ (# 880289) and ZnO (# 891397).

The lattice parameters (a, b and c) can be calculated from the value of inter-planar spacing (d_{hkl}) for a particular crystal plane (hkl). In case of ZnO, the inter-planar spacing in hexagonal lattice (a=b≠c) is givenby

$$\frac{1}{d^2_{hkl}} = \frac{4}{3}\left[\frac{h^2 + k^2 + l^2}{a^2}\right] + \frac{l^2}{c^2} \tag{2.2}$$

Linear equations corresponding to each reflection (hkl) in the XRD spectra could be obtained after substituting the respective values of d_{hkl} in equation (2.2) and thus the values of lattice constants (a, b and c) can be determined.

Fig. 2.7 Photograph of grazing incidence XRD used in the present work

2.3.2 Surface Profiler

Surface profilometer is an instrument used to measure the surface roughness as well as thickness of thin film samples. The automated instrument is equipped with a stylus, which is capable of making vertical and horizontal motion. In order to make measurements, the stylus is moved vertically down to make a contact with the sample at a specified contact force. Subsequently, the stylus is moved laterally across the sample surface for a specified scan distance and the profilometer measures small surface variations in vertical displacement of the stylus as a function of lateral position. The fluctuations along the vertical direction of stylus generate an analog signal which is converted into equivalent digital signal and is stored, analyzed and displayed. In the present study,

thickness and roughness measurements of deposited thin films are carried out using surface profilometer.

2.3.3 Atomic Force Microscope

The Atomic Force Microscope (AFM) is a high resolution type of scanning probe microscope to examine the surface morphology of a sample by measuring the forces between a cantilever tip and the sample surface. The probing tip apex is affixed to a cantilever type spring. The force between the probe tip and sample causes deflections in cantilever which are then monitored by deflection sensor (fig. 2.8). The deflection is identified with the help of a laser beam which is focused on the cantilever. The relative position of the laser beam spot can be detected using the photodiode. A plot of the laser deflection versus tip position in the x, y and z directions on the sample surface provide two/three dimensional surface images. A sensitive piezoelectric element is also provided, which controls the position and motion of the tip as it scans the surface of the substrate.
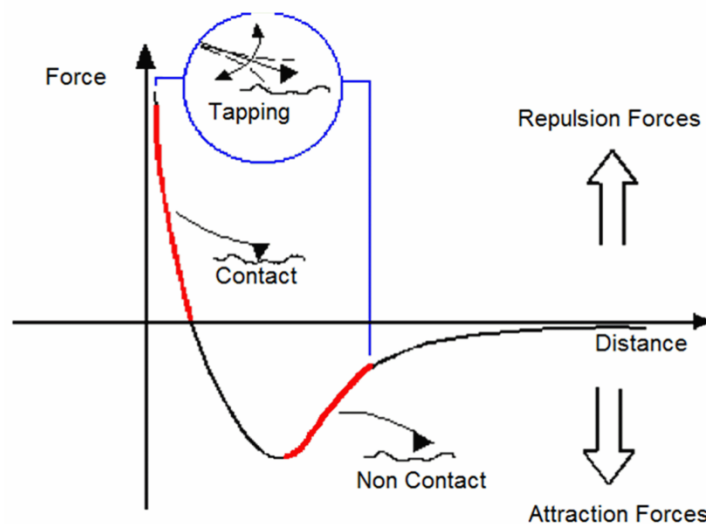
Fig. 2.8 Attractive and repulsive forces at the tip of AFM working in contact and noncontact modes

AFM can be operated in mainly 3 modes: (i) contact mode (ii) non-contact mode and (iii) tapping mode. In contact mode, the tip apex makes direct contact with the surface and the force acting between the atoms of tip and sample is counter balanced by the elastic force produced by the deflected cantilever according to Hooke's law: $F = -kz$. Ionic repulsion forces allow the surface topography to be examined with high resolution.

Fig. 2.9 Photograph of AFM used in the present study

In the contact mode, the tip being in contact with the sample may deform the surface topography. In non-contact mode, the tip sample surface separations are of the order of 10-100 nm. Forces such as Vander Waal's electrostatic or magnetic forces can be sensed in this mode, to yield information such as surface topography, charge distribution etc. However, the data obtained in non-contact

mode could be inaccurate owing to the weak forces (Vander Waal) involved in the process. In the tapping method, the tip vibrates at a particular resonance frequency and taps the surface and detects the change of frequency due to the changes in Coulomb force. In the present study, AFM measurements of samples were carried out using company name and the images were analyzed by Spiwin Lab analysis software. The instrument used in the present work is shown in fig. 2.9.

2.3.4 Field Emission Scanning Electron Microscope

In any material, morphology is a key factor in deciding the material properties. The morphological features of the materials are best analyzed by the scanning microscopy techniques which differ or enhance the chemical/physical properties of the material. In standard electron microscopes, electrons are generally emitted from a thermionic source. Commonly used filaments are Tungsten (W) and Lanthanum hexaboride (LaB_6). When the heat is enough to overcome the work function of the filament material, the electrons can escape from the material itself. Thermionic sources have low brightness, evaporation of cathode material and thermal drift. These disadvantages can be avoided by using field emission guns (FEG). An FEG, also called as cold cathode field emitter does not heat the filament. The emission is reached by placing the filament in a huge electric potential gradient. An extremely thin and sharp tungsten needle (10-100 nm) works as cold cathode. The significance of the small tip radius is that an electric field can be concentrated to an extreme level to make the work function of the material lower and electrons can easily leave the cathode. The electron beam produced by the FEG source is about 1000 times smaller than that in a standard microscope with a thermal electron gun and hence the image quality

will be markedly improved. The FESEM setup with an EDX inbuilt with which the measurements were carried out for the present work is shown in fig. 2.10.

Fig. 2.10 Photograph of FESEM used in the present work

2.3.5 UV-Visible spectrophotometer-optical studies

Ultraviolet-Visible spectrophotometer refers to the absorption spectroscopy in the ultraviolet-visible spectral region wherein, the spectrophotometer quantifies the electronic transitions made by the sample. It is an efficient technique to determine the band gap and refractive index of the thin film samples. In the present study, $LiNbO_3$ and Al:ZnO thin films were deposited on optically transparent substrates to minimize the error corresponding to substrate transmission/absorption. The UV-visible measurements were carried out in the wavelength range of 190-2500 nm using a computer interfaced Jasco V-570 UV/VIS/NIR spectrophotometer as shown in fig. 2.11.

Optical band gap refers to the minimum photon energy required to transfer the electron from the top of the valence band to the bottom of the conduction band. It is one of the major factors determining the conductivity of a given sample. The band gap of the deposited thin films was calculated from the values of absorption coefficient plotted as a function of wavelength using Tauc's plot. The determination of optical band gap was done by extrapolating Tauc's plot [Anil Tumuluri et al. (2014)] using the

$$\alpha h\nu = A(h\nu - E_g)^n \qquad (2.3)$$

where A is a constant, hν – photon energy, E_g – allowed energy gap, n = ½ for allowed direct transition, n = 2 for allowed indirect transition. A graph between $(\alpha h\nu)^2$ or $(\alpha h\nu)^{1/2}$ and hν is plotted and the band gap is estimated by extrapolating the linear part of the Tauc's plot on the energy axis.

Fig. 2.11 Photograph of UV-Visible spectrophotometer used in the present study

2.3.6 Raman Spectroscopy

Raman spectroscopy measurement is a very reliable spectroscopic technique for the investigation of phase purity and the composition of chemical species based on their vibrational modes. Raman spectroscopy is based on the elastic scattering of monochromatic light, usually from a laser source. Inelastic scattering means that the frequency of photons in monochromatic light changes upon interaction with a sample. Photons of the laser light are absorbed by the sample and then re-emitted. Frequency of the re-emitted photons is shifted up or down in comparison with original monochromatic frequency, which is called the Raman effect. An incident optical photon of frequency (ω_i) and wave vector (**k_i**) interacts with the lattice through exchanges of quantum of energy (electron-radiation interaction) and creates an electron-hole pair in the process. These electrons after creating (or annihilating) a photon of frequency ω (and wave vector K) via electron-lattice interaction recombines with the hole. As a result, the scattered light loses or gains energy depending on whether a phonon is created or annihilated. If the scattered photon frequency is ω_s (and wave vector K_s), then the conservation of energy and wave vector leads to

$$\omega_i = \omega_s \pm \omega \quad \text{and} \quad k_i = k_s \pm k \qquad (2.4)$$

If ω_s is smaller (or larger) than incident photon frequency, it is called Stokes (or anti Stokes) scattering. Change in the incident photon frequency (often expressed in wave number, cm^{-1}), (ω_i-ω), is called the Raman shift. By measuring the Raman shift of the energy of the scattered light relative to the incident light, the characteristic vibrational energy spectrum of a given solid (Raman spectrum) is obtained.

In the present work, Raman scattering measurements on LiNbO$_3$ and ZnO thin film samples were performed using a SNOM (Scanning Near field Optical Microscopy) equipped with a Raman spectrophotometer-Reinshaw Invia Raman Microscope equipped with Nd:YAG 532 nm wavelength in the back scattering geometry in a CRM spectrometer equipped with a confocal microscope and 100x objective (1 µm diameter focal spot size) with a CCD detector (model alpha 300 of WiTec, Germany).

2.3.7 Z-scan technique

The nonlinear optical properties can be measured from Z-scan, a widely used technique. Z-scan technique is simple and most sensitive. The Z-scan works on the principle of moving the sample under investigation through the focus of a tightly focused Gaussian laser beam. The interaction of the medium changes with laser light as the sample is moved. The sample exhibits different laser light intensities depending on the sample position (Z) with reference to the focus (Z=0). By measuring the transmitted power (the transmittance) through the sample as a function of Z-position of the sample, one can extract the information about the light matter interaction as a function of intensity. Nonlinear refractive index and nonlinear absorption coefficient can be determined from these nonlinear interactions. To measure the optical nonlinearities of LiNbO$_3$ thin films, a standard Z-scan technique was employed. For these studies, a tunable Ti:Sapphire femtosecond laser (Chameleon, Coherent) with 150 fs, 80 MHz and 800 nm wavelength was used. The open aperture Z-scan curve is fitted to the two photon absorption given by the following equation using Sheik Bahae model [Soma Venugopal Rao et al. (2011)]

$$T(z) = 1 - \frac{\beta I_o L_{eff}}{2\sqrt{2}(1 + Z^2 / Z_o^2)} \qquad (2.5)$$

where, β- third order nonlinear absorption coefficient, L_{eff} – $[1-\exp(-\alpha_o L)]/ \alpha_o$ is the effective length. Z is the position of sample and Z_o is the Rayleigh range. The closed aperture Z-scan curve is fitted using the following equation for positive nonlinearity.

$$T(z) = 1 + \frac{4x\Delta\Phi_0}{(x^2 + 9)(x^2 + 1)} \qquad (2.6)$$

where $x=z/z_0$, Z is the position of the sample, Z_0 is the Rayleigh range, $\Delta\Phi_0 = 2\pi n_2 I_0 L_{eff}/\lambda$ is the phase modulation and n_2 is third order nonlinear refractive index.
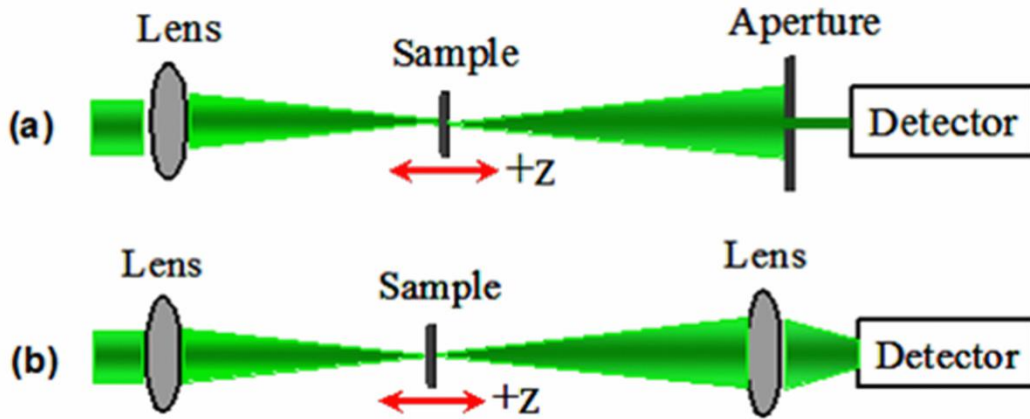
Fig. 2.12 *Schematic of (a) open aperture (OA) (b) closed aperture (CA) configuration of experimental set up*

2.3.8 Vector Network Analyzer - Microwave dielectric characterization

Network analyzer is a very sensitive instrument used to analyze the complicated microwave circuits and structures in terms of their S parameters, where S_{11} (complex input reflection coefficient), S_{21} (complex input transmission coefficient), S_{12} (complex output reflection coefficient) and S_{22} (complex output

transmission coefficient) can be measured. These parameters can be employed for the calculation of precise microwave dielectric parameters (Anil Tumuluri et al. (2015)). Commercially available network analyzers can be of two types: scalar and vector network analyzers. Scalar network analyzer is used to measure the magnitude of reflection and transmission coefficients while the vector network analyzer measures both the magnitude and phase.

Fig. 2.13 Photograph of Vector Network Analyzer (model no. E8361C) used in the present study

In the present work, the microwave dielectric properties like dielectric constant, Quality factor and temperature coefficient of resonant frequency of dielectric resonators (DR) were measured using the $TE_{01\delta}$ mode resonance of the DRs using cavity resonator purchased from QWED of Poland. The $TE_{10\delta}$ mode is one of the most accurate modes to extract the dielectric loss tangent and real permittivity of isotropic low loss dielectric materials.

Chapter 3

Structural, linear and nonlinear optical properties of LiNbO$_3$ thin films

---

In this chapter, LiNbO$_3$ thin films were deposited by means of Al:ZnO as intermediate layer using pulsed laser deposition and their structural details were revealed. The films were found to be polycrystalline, (110) and (300) oriented deposited on fused silica, Al:ZnO/fused silica and Al:ZnO/quartz substrates respectively. The films evidenced transparency of above 80% in visible and near IR region. The polycrystalline and (300) LiNbO$_3$ demonstrate reverse saturable absorption and transits to saturable absorption in case of (110) LiNbO$_3$. Nonlinear optical properties measured from Z-Scan gives the detailed insight into the nonlinear absorption coefficient, nonlinear refractive index and nonlinear susceptibility. The two photon absorption is attributed to the indirect transition via intermediate defect levels which relates to the structural unsymmetry and significant change in band gap also contributes to the nonlinearity in LiNbO$_3$ thin films. The large nonlinearity in refractive index is the result of electronic polarization and ferroelectric polarization. The third order nonlinearity of polycrystalline LN and LN (300) are in the order of 10^{-9} esu and LN (110) is in the order of 10^{-15} esu which is greater than the single crystal Z-cut LiNbO$_3$.

3.1 Introduction

Lithium niobate ($LiNbO_3$) with its distinct features possess unique combination of versatile properties like non-linear optical, piezoelectric, ferroelectric, electro-optic, pyroelectric by making this material suitable for wide range of applications like non-linear optical devices, transducers, electro optic modulators and pyroelectric sensors [Mirco Imlau et al. (2015)]. The phenomenal growth of $LiNbO_3$ crystal for versatile applications encouraged for further studies till date.

Research on single crystal X-cut, Y-cut and Z-cut $LiNbO_3$ are highly in demand to meet the device structures and the performance can be enhanced with oriented single crystal of $LiNbO_3$ [Marco Bazzan et al. (2015)]. Researchers focused the work to integrate and miniaturize devices in to a single platform. For this reason, $LiNbO_3$ single crystal in many orientations are studied and widely used in thin film form by chopping them into thin slices using crystal ion slicing technique [Mackwitz et al. (2016), Cai et al. (2015)]. Although, the advantages were enjoyed, the drawbacks like high surface roughness, difficulty in implantation of foreign ions and expensive chopping made it difficult to use them for versatile miniaturized applications [Martin F. Volk et al. (2016)]. Keeping this in mind, epitaxial $LiNbO_3$ thin films came into existence to support the above mentioned applications. High quality $LiNbO_3$ thin films can be utilized to overcome the above mentioned drawbacks to certain extent [G. Balestrino et al. (2001)].

Reports on deposition of $LiNbO_3$ thin films using different techniques like sol-gel, RF magnetron sputtering and pulsed laser deposition are widely available [Peng You et al. (2013)]. Most of the literature explains the optimization

of deposition conditions for the successful deposition of LiNbO$_3$ thin films. Epitaxial growth of LiNbO$_3$ thin films with ZnO as buffer layer is meager [Shandilya et al. (2009)]. Moreover, oriented deposition of LiNbO$_3$ thin films on amorphous substrates is found to be interesting in many applications. Because of its flexibility in deposition, LiNbO$_3$ thin films on amorphous substrates are highly in demand. LiNbO$_3$ is well known for its second order nonlinearity and several groups reported the enhancement of nonlinearity using different techniques. But, third order nonlinear optical properties of LiNbO$_3$ thin films have not been explored much [WANG Qu-Quan et al. (2002)].

Third order nonlinear optical properties of ferroelectric materials have profound applications in nonlinear photonic devices [Li et al. (2014)]. Ferroelectric materials have been widely investigated for their random access memory devices, piezoelectric, pyroelectric, integrated photonics and nonlinear optical applications [Setter et al. (2006)]. Among all the ferroelectric materials, Lithium niobate (LN) is a well studied ferroelectric with high spontaneous polarization and high Curie temperature. Although paramount properties that can be enjoyed in single crystal cannot be reproduced in thin film, the miniaturization of device structure, high quality thin film on desired substrate and ease in doping foreign ions made the researchers to focus on LiNbO$_3$ thin films [Anil Tumuluri et al. (2016)].

C-axis oriented ferroelectric LiNbO$_3$ thin films were deposited with ZnO as buffer layer [Shandilya et al. (2012)]. More studies are to be done to explore LiNbO$_3$ thin film properties to utilize them for device structures. S.M.Kostritskii et. al measured nonlinear absorption of congruent LiNbO$_3$ crystals and observed two photon absorption associated with the photo dissociation of bipolarons

[Kostritskii et al. (2012)]. The nonlinearity in LiNbO$_3$ crystal with changing beam waist with Z-scan and the nonlinear absorption coefficient (β) is found to be 5 cm/KW [Fryad et al. (1995)]. Studies on LiNbO$_3$ thin films on amorphous substrates (fused silica) are of interest because of its cost effective applications in optical devices.

3.2 Experimental details

LiNbO$_3$ and Al:ZnO thin films were deposited by PLD (Excel Instruments-Mumbai, India), employing a KrF excimer laser (λ=248 nm). The LiNbO$_3$ target of one inch diameter was prepared from commercially available LiNbO$_3$ powder (Alfa aesar, 99.99% purity) by adding 5 wt.% of Li$_2$CO$_3$ (Sigma Aldrich, 99.99% purity) for Li loss compensation. The LiNbO$_3$+Li$_2$CO$_3$ mixture is pressed using Poly Vinyl Alcohol (PVA) as binder followed by sintering at 1100 ^{o}C for 2h. Al:ZnO (Al:0.5 wt%) target of 1 inch diameter was prepared by ball milling Al$_2$O$_3$ (purity 99.9%, Alfa aesar) and ZnO (purity 99.99%, Sigma Aldrich) and pressed with PVA as binder followed by debinding and sintered at 900 ^{o}C for 2 h. Fused silica and Z-cut quartz (SiO$_2$) substrates were ultrasonicated in acetone solution and then dried to get impurity free substrate wafers. These substrates were mounted onto substrate holder facing target with an angle of 180° to get maximum plume condensed onto the wafer. All deposition conditions like laser fluence, partial pressure, and substrate temperature and repetition rate for both ZnO and LiNbO$_3$ were tabulated in fig.3.1.

The present Z-scan technique possesses a configuration of mode locked Ti:sapphire laser with a continuous wave 800 nm high power laser with a Gaussian spatial profile at a repetition rate of 80 MHz.

	Substrate Temperature (°C)	Working Pressure (mbar)	Laser fluence (J/cm^2)	Repetition rate
LiNbO$_3$ / **Fused silica**	600	1.5×10^{-1}	1.52	5
Polycrystalline LiNbO$_3$ - LN 01				
LiNbO$_3$ / **Al:ZnO** / **Fused silica**	600 / 100	1×10^{-1} / 1.5×10^{-1}	1.52 / 1.52	5 / 5
(110) oriented LiNbO$_3$ - LN 02				
LiNbO$_3$ / **Al:ZnO** / **Z-cut quartz**	600 / 500	1×10^{-1} / 2×10^{-3}	1.52 / 1.52	5 / 5
(300) oriented LiNbO$_3$ - LN 03				

Fig. 3.1 *Schematic representation of substrate/ZnO/LiNbO₃ thin films used for the present study and their deposition conditions*

3.3 Structural studies on LiNbO₃ thin films

XRD spectra of LN 01, LN 02 and LN 03 are measured using GI-XRD and are shown in fig. 3.2. XRD studies show that all the peaks in LN 01 correspond to LiNbO₃ and are found to be polycrystalline in nature. All peaks were indexed based on JCPDS diffraction file # 880289. The amorphous nature of the substrate and the annealing temperature (600 °C) allowed LiNbO₃ to grow as polycrystalline with multiple planes oriented in different directions. LN 02 has predominantly one diffraction peak centered at $2\theta\sim34.6°$ which corresponds to (110) reflection from LiNbO₃ and underneath Al:ZnO grows in (002) direction. The Al:ZnO is deposited on fused silica under the minimal stress conditions at 100 °C oriented in (002) direction [XU Jian-Ping et al. (2010)]. The peak positions of (002) Al:ZnO at 34.5° and (110) LN 02 at 34.6° overlaps and cannot be distinguished. LN 03 deposited on Z-cut quartz with Al:ZnO as intermediate layer has only one peak at 62.9°. This peak also overlaps with the bottom layer

ZnO whose (103) plane originates at 62.7° (JCPDS diffraction file # 891397). Al:ZnO acts as a nucleating layer and controls the growth of LiNbO$_3$ in case of LN 02 and LN 03. In case of LN 02, Al:ZnO is oriented in (002) and (103) in case of LN 03.
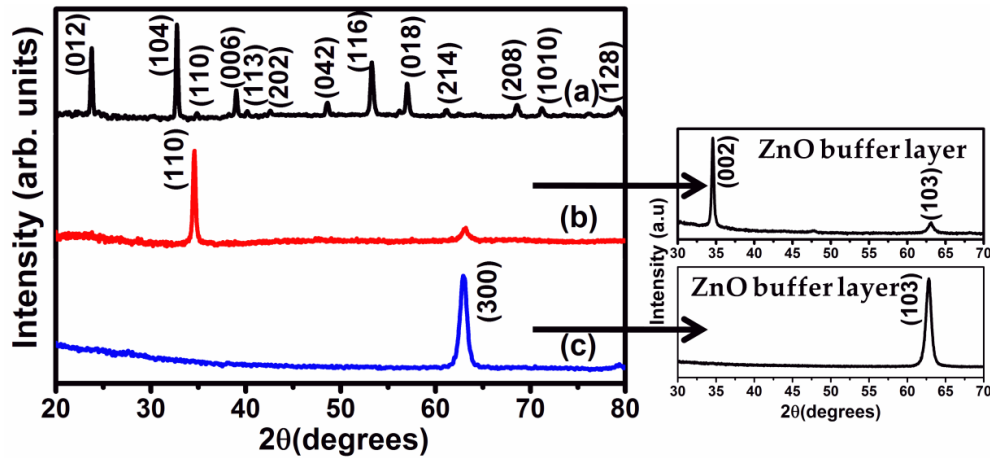
Fig. 3. 2 XRD patterns of (a) LN 01 (b) LN 02 (c) LN 03

In general, ZnO tend to grow in (002) preferred orientation because of its lowest surface energy in this plane [Yunlan Wang et al. (2013)]. The FWHM of (103) peak is larger than (002) peak indicating the induced stress along (103) direction larger than that of (002) direction. The main reason for stress is due to the lattice mismatch for LN 03 where this can be ignored in case of LN 02. Another important reason for stress is the substrate temperature of both the films deposited at 100 °C and 500 °C. It has been reported that at higher temperature, in Al:ZnO the (103) growth strongly dominates over (002) [Ashish Kumar et al. (2015)]. This confirms that Al:ZnO possess (103) oriented film deposited at 500 °C has lower surface free energy than (002) oriented film deposited at 100 °C. Based on the nature of substrate, substrate temperature, parameters like laser fluence

and partial pressure growth of LiNbO$_3$ can be optimized in preferred orientation. The optimized parameters were given in fig. 3.1.

3.4 Morphological studies

Fig. 3.3 shows the 2D and 3D AFM images along with microstructure obtained from FESEM of LN thin films. The surface morphology of LN 01 consists of loosely packed grains with random orientation which can be confirmed from FESEM image also (fig. 3.3). LN 02 consists of dense and well structured grains. The (002) oriented Al:ZnO as an underlying layer controlled the morphology of LN where incase of LN 01, the grains are distorted and not well crystallized at 600 ^{o}C. This also infers that 600 ^{o}C is not the optimized crystallization temperature for LN on fused silica (amorphous) substrate. In case of LN 02, the grains are well crystallized and oriented in a direction. The average roughness of all the films were extracted by AFM images using SPIWIN image analysis software.

The average roughness of is found to be 10 nm, 7 nm and 4 nm for LN 01, LN 02 and LN 03 respectively. The roughness is descending for LN 01, LN 02 and LN 03. The role of the substrate is highly important in the growth of bottom layer which ultimately decides the microstructure and growth of top layer. In case of LN 03, the morphology is apparently different with elongated grains. In this case, LN 03 has Al:ZnO has (103) orientation where the stress induced to grow along (103) is more when compared to (002) as discussed before. From XRD, the FWHM of peaks follows the trend $FWHM_{LN01} < FWHM_{LN02} < FWHM_{LN03}$ which confirms the increased stress in case of LN 03.
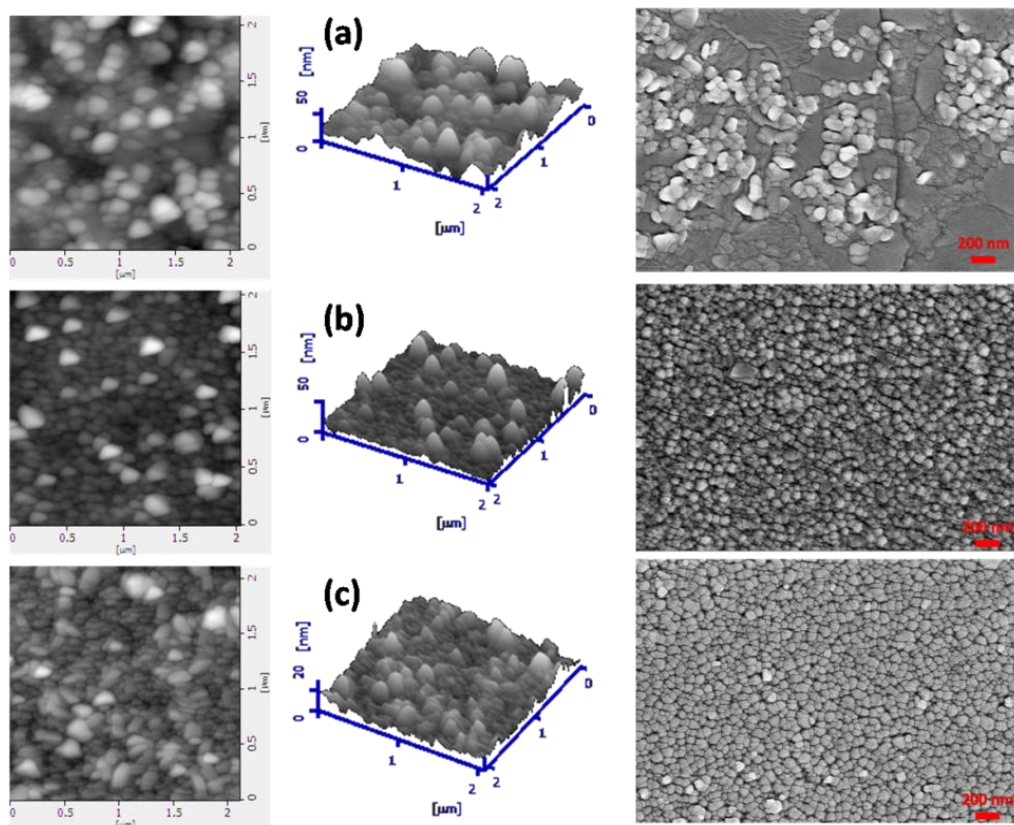
Fig. 3. 3 AFM (2D and 3D) and FE-SEM images of (a) LN 01 (b) LN 02 (c) LN 03

3.5 Linear optical properties

Fig. 3.4 gives the transmission spectra of LN films in the wavelength range of 200-1400 nm (visible-near IR) region. The oscillations in the spectra confirm that the films are smooth and possess uniform thickness. It can be inferred that the films exhibit good transparency in visible and near infrared region. In near IR, the average transmittance of all films is around 86% and got decreased in visible region ranging 78-86%. The LN 02 and LN 03 are more transparent compared to LN 01. This might be because of the optical loss obtained from scattering of incident photon from grains and grain boundaries present in the

polycrystalline film whereas the LN 02 and LN03 has densely packed grains with lesser grain boundaries. The morphology of LN 01, LN 02 and LN 03 confirms the roughness of the films where the scattering of incident photons will be more in case of LN 01 and less in case of LN 02 and LN 03. The thickness of the films was given in table 3.1.

The optical band gap (E_g) of the films are determined from Tauc's plot and shown in fig. 3.5. The single crystal LiNbO$_3$ exhibits a fundamental direct/indirect band gap of 4 eV [Thierfelder et al. (2010)]. The optical band gap of LiNbO$_3$ is detrimental to the valence electronic transitions from 2p orbitals of O^{2-} to the 4d orbitals of Nb^{5+} [Anil Tumuluri et al. (2014)]. The distortion of oxygen octahedron also depends on the concentration of intrinsic defects. This band gap either red shifts or blue shifts depending on the crystal orientation and growth technique and defect concentration [Sangeetha et al. (2015)].

The literature on band gap of LiNbO$_3$ thin films is insufficient. Fig. 3.5 gives the direct and indirect band gap plots of LiNbO$_3$ thin films for comparison and analyzed to give more insight into the electronic transitions of LiNbO$_3$ in polycrystalline and oriented form. For LN 01, LN 02 and LN 03 a plot of α did not provide an exponential dependence on hν. Therefore, the low energy absorption edge observed from the transmittance data of fig. 3.4 can be better interpreted as being due to the indirect absorption instead of the direct absorption.

It is clear that the direct band gap is in the range of 4.5 to 3.7 eV whereas there is a decrease in indirect band gap ranging from 4 to 3.3 eV. For all the films, the band gap is found to be indirect which can be confirmed from the absorption band edge of transmission spectra.
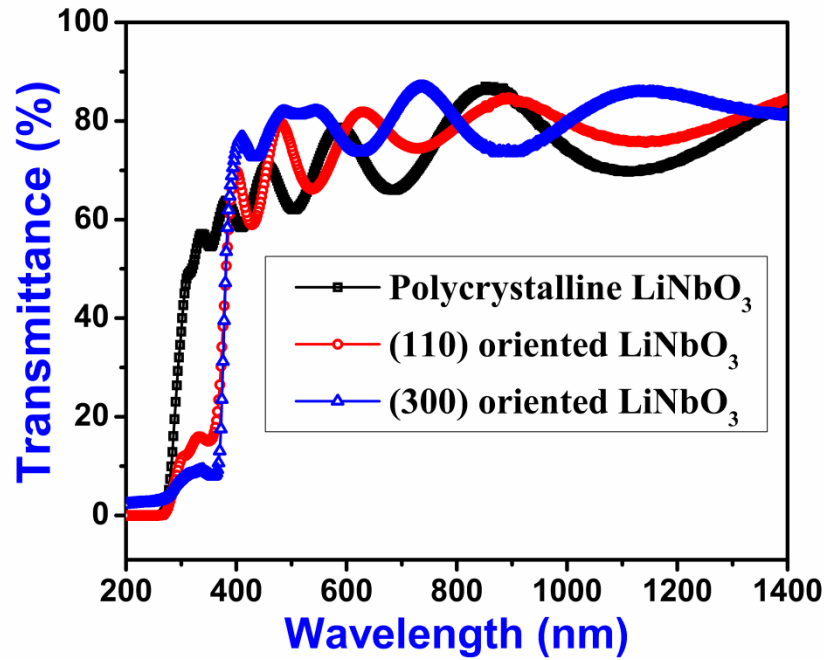
Fig. 3.4 Optical transmittance spectra of LiNbO₃ thin films Polycrystalline LiNbO₃ (LN 01), (110) oriented LiNbO₃ (LN 02) and (300) oriented LiNbO₃ (LN 03)

LiNbO₃ thin films have been deposited using RF magnetron sputtering and found that band gap is varying with change in substrate annealing temperature [Anil Tumuluri et al. (2014)]. Ferro and paraelectric states of LiNbO₃ have theoretically been calculated from DFT and GW approximation [Thierfelder et al. (2010)]. The determination of optical band gap is obtained by Tauc's equation [Brian D. Viezbicke et al. (2015)]

$$\alpha h\nu = A(h\nu - E_g) \tag{3.1}$$

where A is a constant, hν is photon energy, E_g is the allowed energy gap, n=1/2 for allowed direct transitions, n=2 for allowed indirect transitions.

From the indirect band gap plots, apart from the major absorption band edge, small unsymmetric absorption band peaks centered at different energies

were clearly observed which cannot be ignored. These absorption peaks were correlated with the defect centers or polaronic peaks which ultimately affect the linear and nonlinear optical properties [Mirco Imlau et al. (2015)]. The contribution of the polaronic states on nonlinear optical properties were discussed in detail in the next section.
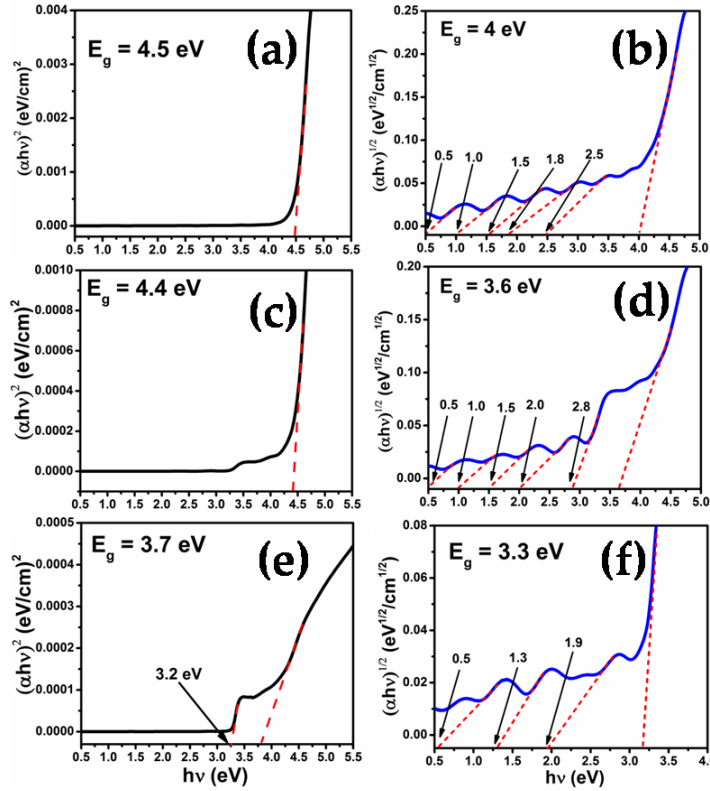
Fig. 3.5 Tauc's plot for (a) Direct band gap of LN 01 (b) Indirect band gap of LN 01 (c) Direct band gap of LN 02 (d) Indirect band gap of LN 02 (e) Direct band gap of LN 03 (f) Indirect band gap of LN 03

The PL spectra recorded for all the thin films with an excitation wavelength of 355 nm were given in fig. 3.6. The wavelength emission wavelength is found to be distinct for LN 01, LN 02 and LN 03. LN 01 did not show any significant emission because of its higher band gap of 4 eV. The excitation wavelength is 355

nm which corresponds to 3.5 eV and is not sufficient to equivalent or higher band gap materials to excite the states of the structure. Small emission peak at 519 nm in case of LN 01 is observed which may be due to the presence of polarons. Broad emission peaks at 614 nm (red) and 558 nm (green) were observed in case of LN 02 and LN 03 respectively.
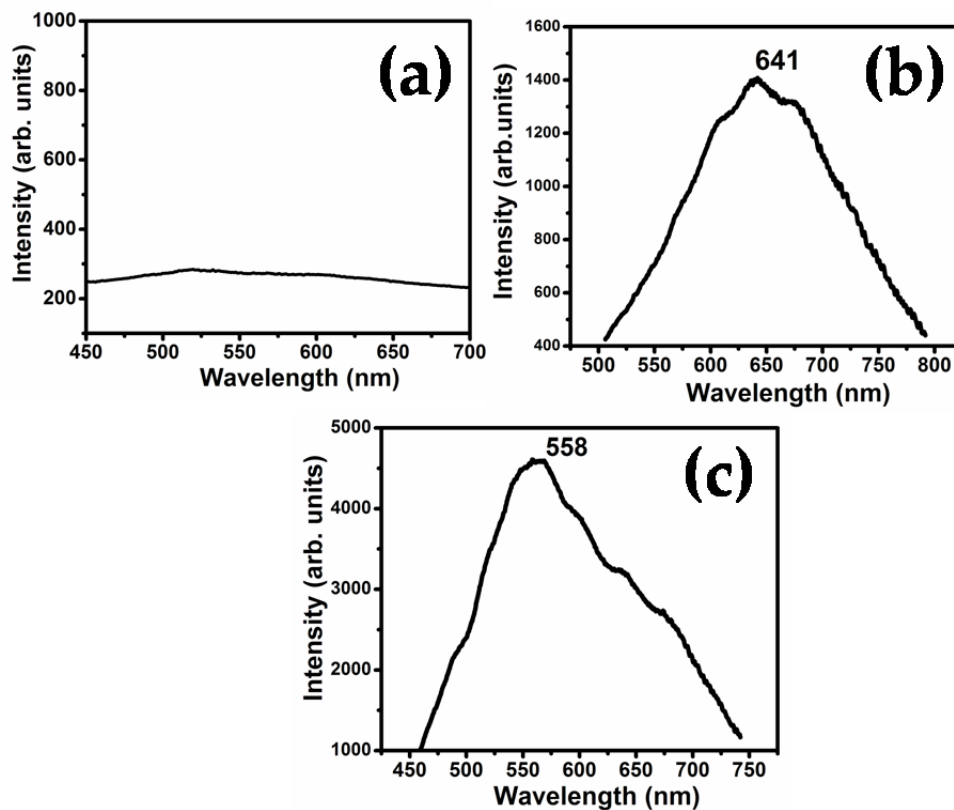
Fig. 3.6 Photoluminescence spectra for (a) LN 01 (b) LN 02 (c) LN 03

In general, literature on emission spectra from pure LiNbO$_3$ is scanty [Anil Tumuluri et al. (2014)]. The red and green emissions are due to the electronic transitions happened in the intermediate states near 1.0 eV (Nb_{Nb}^{4+}), 1.6 eV (Nb_{Li}^{4+}) and 2.5 eV (both Nb_{Nb}^{4+} : Nb_{Li}^{4+} and O$^-$). But, the emission mechanism cannot be

explained solely based on the luminescence spectra. Efficient blue (473 nm) and green (505 and 525 nm) emissions were observed from polycrystalline $LiNbO_3$ ceramics doped with Sc_2O_3 and Lu_2O_3 [Anil Tumuluri et al. (2014)]. Luminescence centers are measured in $LiNbO_3$ crystals and the kinetics of color-center recombination due to different polaronic states which can be confirmed from the asymmetric absorption bands are explained in fig. 3.5 [Yakovlev et al. (2001)].

3.6 Nonlinear optical properties

The intensity dependence of nonlinear absorption and refraction were examined for LN 01, LN 02 and LN 03 thin films. Open Aperture (OA) and Closed Aperture (CA) Z-scan experiments were carried out with an femtosecond laser and were shown in fig. 3.7. The thickness of all samples satisfies the Rayleigh range condition L< $n_o Z_o$ where n_o is the linear refractive index at 800 nm, Z_o is the Rayleigh range, L is the thickness of sample. The substrate (fused silica and quartz) nonlinearity is recorded for reference and subtracted for all the films.

The OA Z-scan curve is fitted to the two photon absorption given by using Sheik Bahae model [Sheik Bahae et al. (1990)]. The OA curve is fitted for two photon absorption (2PA) and three photon absorption (3PA) using equations 2 and 3 respectively. From OA fitted curve, nonlinear absorption coefficient (α_2) is calculated

$$T_{OA}(2PA) = 1/1 + \alpha_2 Leff(I_{00}/1 + (Z/Z_o)^2)$$

(3.2)

where effective path length $L_{eff}(2PA) = 1 - e^{-\alpha_2 L}/\alpha_2$

$$T_{OA}(3PA) = 1/[1 + 2\alpha_3 L_{eff}(I_{00}/(1+(Z/Z_o)^2))]^{1/2} \qquad (3.3)$$

$$L_{eff}(3PA) = 1 - e^{-2\alpha_3 L}/2\alpha_3 \qquad (3.4)$$

I_{00} is the peak intensity, Z is the sample position, Z_o is the Rayleigh range, α_2 and α_3 are 2PA and 3PA coefficients.

The optical band gap of all the films satisfies $2h\nu < E_g < 3h\nu$ ($h\nu = 1.55$ eV is the energy corresponding to laser wavelength of 800 nm), suggesting an indirect two photon absorption via intermediate defect states [Li et al. (2014)]. Reverse Saturable Absorption (RSA) is observed in case of LN 01 and LN 03 where as Saturable Absorption (SA) in case of LN 02.

The factors influencing the switching phenomenon from RSA to SA is the competition between the ground-state excitation and the nonlinear absorption, which further depends on the laser photon energy, the optical band gap of materials and intensity of the incident radiation [Basanth S. Kalanoor et al. (2016)]. In the present study, the Z-scan experiments were conducted at fixed intensity of incident radiation (I_o) and wavelength (λ). Therefore, the nonlinear optical absorption switching in LiNbO$_3$ thin films may be attributed to the changes occurred in optical band gap (E_g) due to structural indifferences. Even a small difference in E_g less than 10 meV is quite enough for the transformation from RSA to SA [Li et al. (2015)].
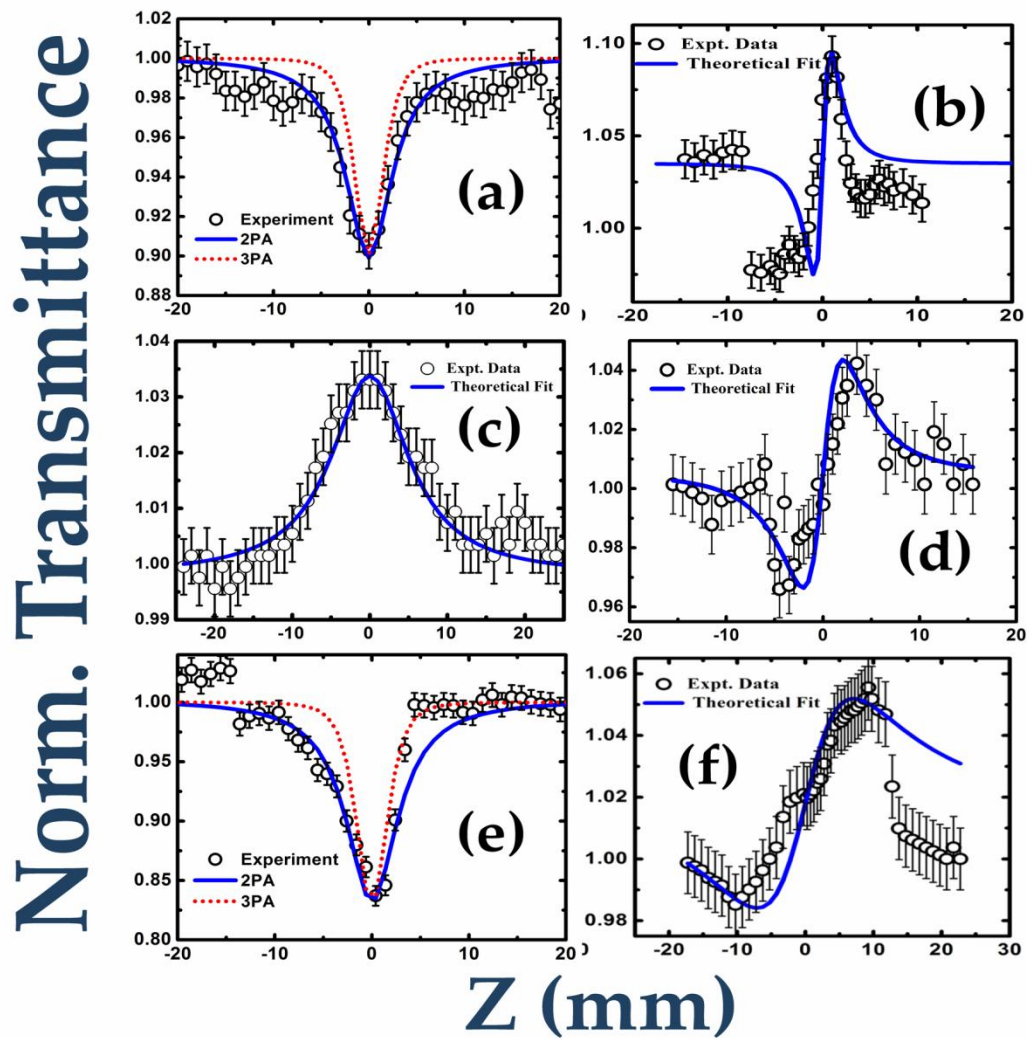
Fig. 3.7 Open aperture and Closed aperture curves of (a) OA curve of LN01 (b) CA curve of LN 01 (c) OA curve of LN 02 (d) CA curve of LN02 (e) OA curve of LN03 (f) CA curve of LN 03

In general, the intermediate defect states (energy levels) between valence and conduction bands act as barrier for the excited electrons to transit. When E_g is larger, it is difficult to excite electrons from defect states to conduction band

through 2PA resulting SA. When E_g is small, more electrons can be allowed into conduction band resulting in RSA [Anusha et al. (2015)].

Again LN 03 holds defect states with a band gap of 3.3 eV confirming the 2PA via intermediate defect levels. The unsymmetric absorption humps from indirect Tauc's plot (fig. 3.5) also confirms the presence of defect states in LN 01, LN 02 and LN 03.
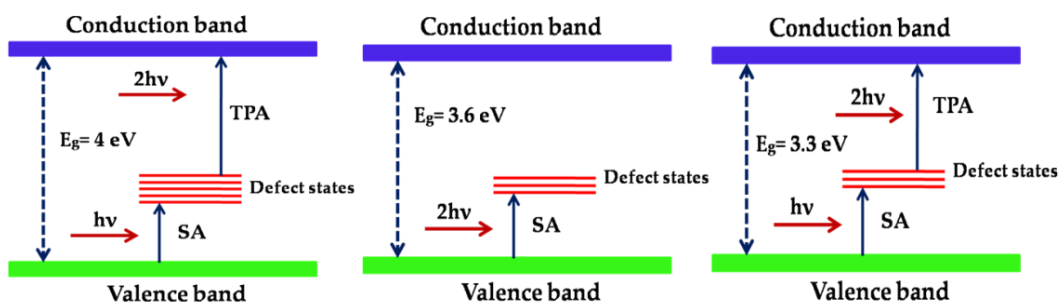
Fig. 3.8 Schematic diagram of nonlinear absorption process in LiNbO₃ thin films with varying band gaps (LN 01 - 4 eV, LN 02 - 3.6 eV, LN 03 – 3.3 eV)

In case of LN 01 and LN 02, E_g is observed to be 4 eV and 3.3 eV whereas 2PA energy corresponds to 3.1 eV. When the films are away from the focus, the transmittance is high and as the sample translates towards focus, the transmittance decreases indicating RSA behavior. RSA is observed mainly because of the nonlinear mechanisms such as two-photon absorption (TPA), free carrier absorption (FCA), nonlinear scattering or a combination of these processes [Pramodini et al. (2014)].
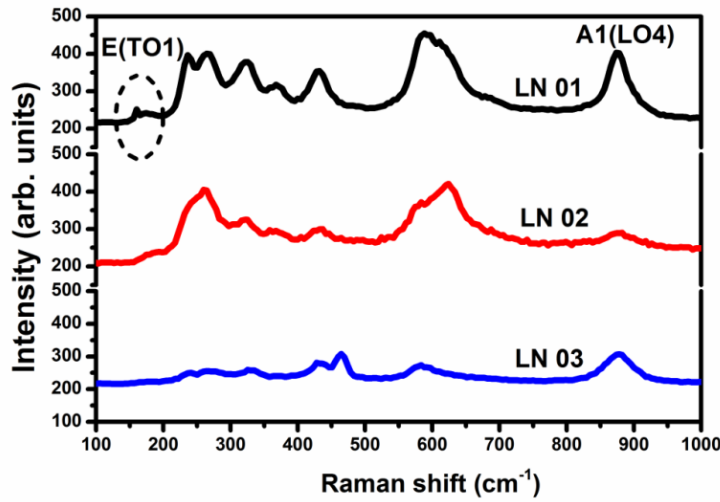
Fig. 3.9 Raman spectra recorded for LN01, LN02 and LN03

In $LiNbO_3$, the defect states are mainly attributed to the antisite defects like Nb replacement in Li site and oxygen vacancies [Shandilya et al. (2009)]. In $LiNbO_3$, RSA is mainly dominated by TPA and the contribution from FCA can be highly ignored since the number of free carriers in $LiNbO_3$ is less where the observed indirect band gap is found to be between 4 to 3.3 eV. Despite of large difference between E_g of LN 01 and 2PA energy, RSA behavior is observed. This might be due to the density of defect states in the band gap. The presence of the density of defect states in LN 01 can be confirmed from intensity of A1(LO4) and E(TO1) Raman peaks corresponding to defect states in $LiNbO_3$ are significantly observed [Marc D. Fontana et al. (2015)]. From microstructure of LN 01 (fig. 3.3(a)), it is clear that grain growth is not complete.

SA is observed from LN 02 where E_g is low compared to LN 01. In general when E_g is low, the possibility of electrons to jump from valence band to conduction band via 2PA is high. This results in absorption saturation of defect states resulting in SA behavior. The laser irradiation results in intraband electron

excitation yielding saturable absorption (SA). This might be because of the absence or inadequate density of defect states. This kind of behavior has not been reported previously in ferroelectric thin films [Li et al. (2015)].

Another reason for RSA and SA can be explained based on polaronic movements in LiNbO₃. The indirect band gap of LN 03 is around 3.3 eV where the contribution to nonlinearity arises from the presence of small bipolarons. In general, the manifestations of small polarons affect strongly the linear and nonlinear optical properties in LiNbO₃ crystal [Mirco Imlau et al. (2015)]. Till now, three different small electron polarons and one type of small hole polaron have unambiguously identified in LiNbO₃. These polarons show strong absorption bands near 1.0 eV (Nb_{Nb}^{4+}), 1.6 eV (Nb_{Li}^{4+}) and 2.5 eV (both Nb_{Nb}^{4+} : Nb_{Li}^{4+} and O⁻) [Mirco Imlau et al. (2015)]. These absorption bands are asymmetric in nature with typical half widths of 1 eV. The presence of these bipolarons can be confirmed from Tauc's plot (fig. 3.5) where asymmetric absorption peaks at lower energies were present. Small polaron absorption is proportional to the product of number density and their absorption cross section.

The values of nonlinear absorption coefficient (β) of LN 01, LN 02 and LN 03 are given in table 3.1. It is clear that for LN 01 and LN 03 positive β is observed and in case of LN 02 it got saturated. The β value is slightly more in case of LN 03 when compared to LN 01 than LN 03. In order to cross check results, 3PA equation is fitted for OA curves of LN 01 and LN 03 as shown in fig. 3.7. But, the 3PA curves did not fit well with the experimental data confirming the two photon absorption.

Fig. 3.7 gives the CA Z-scan curve of LN 01, LN 02 and LN 03 films. The intense valley followed by a peak was observed while moving the sample through the focal point. This indicates the positive sign associated with the nonlinear refraction accompanied by nonlinear absorption.

$$T_{CA} = 1 - \frac{4\Delta\phi_o(z/z_o)}{\left[1+(z/z_o)^2\right]\left[9+(z/z_o)^2\right]} \tag{3.5}$$

where $\Delta\phi_o$ - Phase change of the laser beam due to nonlinear refraction and is estimated by fitting the experimental data, Z is the position of sample Z_o is the Rayleigh range.

$$n_2(cm_2/W) = \frac{|\Delta\phi_o|\lambda}{2\pi I_{00}L_{eff}} \tag{3.6}$$

The nonlinear refractive index was estimated from closed aperture Z-scan. The large refractive nonlinearity of LN 01 and LN 03 compared to LN 02 is due to the third order polarization $P^{(3)}$ which includes the electronic polarization P_e and ferroelectric polarization P_f [Li et al. (2014)]. Another important reason is the enhancement of strain in the film which further increases the ferroelectric polarization.

For calculating $Re|\chi^{(3)}|$ and $Im|\chi^{(3)}|$ values following equations were used and the value of $|\chi^{(3)}|$ is extracted. Nonlinear optical coefficients like real and imaginary parts of susceptibility, nonlinear absorption coefficient and refractive index were given in table 3.1.

$$Re|\chi^{(3)}|(esu) = \frac{10^{-4}\varepsilon_o n_o^2 c^2}{\pi} n_2\left(\frac{m^2}{W}\right) \tag{3.7}$$

$$Im|\chi^{(3)}|(esu) = \frac{10^{-2}\varepsilon_o n_o^2 c^2 \lambda}{4\pi^2} \alpha\left(\frac{m}{W}\right) \tag{3.8}$$

where n_o is refractive index of solvent, n_2 is refractive index of material, ε_o is permittivity of free space and c is the velocity of light

$$\left|\chi^{(3)}\right|(\text{esu}) = \sqrt{\left\|\text{Re}\left|\chi^{(3)}\right|\right\|^2 + \left\|\text{Im}\left|\chi^{(3)}\right|\right\|^2}$$ (3.9)

Table 3.1 Nonlinear optical parameters calculated for LiNbO₃ thin films

Sample	Femtosecond laser power (mW)	α_2 (cm/W) ×10^{-8}	n_2 (m²/W)	Re|$\chi^{(3)}$| (esu)	Im|$\chi^{(3)}$| (esu)	|$\chi^{(3)}$| (esu)
LN 01	3	125	1.7×10^{-13}	2.2×10^{-15}	1.2×10^{-9}	1.0×10^{-9}
LN 02	3	-217	1.1×10^{-17}	1.90×10^{-19}	2.3×10^{-15}	2.3×10^{-15}
LN 03	3	165	1.1×10^{-16}	1.4×10^{-10}	1.3×10^{-9}	1.3×10^{-9}

In conclusion, LiNbO₃ thin films were deposited using pulsed laser deposition. Third order nonlinear optical properties of the films were investigated from Z-scan technique at a wavelength of 800 nm. Positive nonlinearity is observed for polycrystalline LiNbO₃ and (300) LiNbO₃. The two photon absorption is observed with indirect transitions via intermediate defect states. The polycrystalline LiNbO₃ and (300) LiNbO₃ exhibits reverse saturable absorption and changes to saturable absorption in case of (110) LiNbO₃. The nonlinear susceptibility of LN 01 and LN 03 (polycrystalline and (300) LiNbO₃) are in the order of 10^{-9} esu which is three orders of magnitude greater than the single crystal Z-cut LiNbO₃. The high optical transparency and third order optical nonlinearity show that LiNbO₃ thin films are a promising candidate for nonlinear photonic devices. SA phenomenon can be used as an ultra fast optical modulation in the laser oscillator to produce ultra short pulse laser and RSA is a typical characteristic for optical limiting by sensors which is seldom reported in LiNbO₃ thin films.

Chapter 4

Temperature dependent optical properties of LiNbO$_3$ thin films using UV-Visible spectrophotometer

This chapter comprises of the studies on temperature dependent linear optical properties of LiNbO$_3$ thin films of various thicknesses using UV-Visible spectrophotometer. The optical constants like absorption coefficient, refractive index and optical band gap of LiNbO$_3$ thin films were extracted from the transmittance spectra in the temperature range of 308-523 K. It is found that the transmittance decreased with increase in temperature from 85-57% in the visible range and the optical band gap also red shifts with increasing temperature from 308-523 K. The band gap is found to decrease from 3.9-3.7 eV where the shift can be attributed to the band gap renormalization. Positive thermo optic coefficient (dn/dT) is observed and is attributed to the structural dissimilarities.

4.1 Introduction

A thin film optical coating is expected to exhibit wide range of properties by fine tuning various external parameters. In general, a thin film presents a range of different properties like thermal, acoustical, nonlinear, chemical and corrosion resistant behavior [Setter et al. (2006), John et al. (2000)]. Influence of external parameters like temperature, pressure and corrosion affect the properties of thin film while using them for practical applications. Many researchers have studied the effect of deposition temperature on the optical, mechanical and electrical properties [Mark J. Miller et al. (2015), Pramodini et al. (2014)]. But, the temperature dependence of optical properties is less studied.

The temperature dependence of thin metal films is prominent because of its versatile applications in chemical, optical telecommunications and biomolecular sensing [Bo Xiao et al. (2016)]. For all the applications mentioned above, the temperature dependence changes the characteristics of functionality. In general, for a thin film to be used in a active or passive device like waveguides, lasers, couplers, interferometers and MEMS, the functioning should be unaltered with external thermal effects. The functioning of the device in turn depends on the properties of thin film. The nature of refractive index and its variation with temperature is of significance in the design of optical devices such as waveguides and optical couplers [Schneider et al. (1982)].

When the devices are irradiated with laser, significant rise in temperature is bound to occur, thereby altering the optical response leading to its converging or diverging properties. Therefore, the study of temperature dependent optical properties is very important to understand. For example, Q.Gan et al. reported

that the trapping of telecommunication rainbow storage of THz light can be scaled to nm level from μm level by frequency dependent dielectric properties of metals [Gan et al. (2009)]. Thus, confined waves are released by capping the metal grating with a dielectric material and temperature tuning of the refractive index of the material at the interface. This temperature dependence of optical properties at the interface is found to have potential applications in nanophotonics and optical telecommunications.

Similarly, temperature dependent optical constants for dielectric and ferroelectric thin films have fundamental importance in many fields such as optoelectronic switches, optical fibers and laser techniques [Liu et al. (2006)]. Changes in temperature dependent optical constants and band gap of semiconductors account for the applications in data storage, optical coatings and display industries to use the advantages of high sensitivity in the detection of the temperature induced small variations in film optical constants and thickness [Allwood et al. (2000)]. Therefore, it is important to explore and develop a precise understanding to evaluate the thermal affects on optical properties with accuracy for bringing out quantitative design aspects of devices.

Lazziri and Jupille et al. measured reflection spectra of nanostructured silver thin films deposited on alumina substrate from 190 to 675K in UV-Visible range [Lazzari et al. (2001)]. S.Tripura Sundari et al. derived temperature dependence of optical constants of silver thin films measured by spectroscopic ellipsometry in the range of 250-885 nm for temperature ranging from 300-650K [Tripura Sundari et al. (2013)]. The changes in band gap and the band gap narrowing coefficient for ferroelectric $Bi_{3.25}La_{0.75}Ti_3O_{12}$ (BLT) films are investigated

in the range of 77-500K [Hu et al. (2007)]. In this paper, they presented the results for future electro-optic and high temperature optoelectronic applications.

N.B.Chen et al. have grown Mg substituted ZnO thin films and measured the absorption edge from the temperature range of 10-300K [Chen et al. (2004)]. The changes observed in optical absorption edge are attributed to the phase transition from cubic to hexagonal structure. The changes in temperature dependent refractive indices of TiO_2 thin films are attributed to thermal expansion and electron phonon interaction [Fan Zhang et al. (2013)]. In that study, optical constants of the thin films are determined by spectroscopic ellipsometry in the temperature range of 293-533K. J.Yang et al. conducted experiments on temperature dependent optical properties of Mn doped $PbSrTiO_3$ ferroelectric films in the temperature range of 80-500K [Yang et al. (2010)]. They investigated thermally driven band gap shrinkage and Urbach tail behavior and the changes were attributed to electron-phonon interaction.

Lithium niobate (LN) is one of the most used materials in optoelectronics. It presents a very interesting combination of properties and characteristics that makes possible the realization of different classes of devices. Their optical, acoustical, piezoelectric, and photorefractive properties have been widely studied and exploited in optoelectronics and photonics [Hirotoshi Nagata et al. (2000)]. As a matter of fact, LN has been employed in many optical devices, such as waveguides, high-speed modulators, beam deflectors, optical frequency converters, and tunable sources of coherent light for spectroscopic applications [Ringleb et al. (2011)].

$LiNbO_3$ nanostructures, thin films and single crystals are being used for multidimensional applications. In particular, the optical properties of

ferroelectric thin films are extensively explored because of their spontaneous electronic polarization dependence. Studies on temperature dependence of optical band gap are still in the preliminary stage owing to the scope for study and scarce known physical parameters. Moreover, the transformation in optical parameters of $LiNbO_3$ thin films with changing temperature is not reported so far. In the present study, temperature dependent linear optical properties of $LiNbO_3$ thin films of various thicknesses are studied using UV-Visible spectrophotometer. The optical constants like absorption coefficient, refractive index and optical band gap of $LiNbO_3$ thin films were extracted from the transmittance spectra in the temperature range of 308-493 K.

4.2 Experimental procedure

$LiNbO_3$ thin films of different orientations and thicknesses were prepared by pulsed laser deposition. $LiNbO_3$ of (110) orientation, $LiNbO_3$ of (300) orientation and polycrystalline $LiNbO_3$ thin film with two different thicknesses were considered for the studies on temperature dependent optical properties. The X-ray diffraction (XRD) spectra are given in fig. 3.2 in Chapter 3. The transmission spectra were measured with a UV-Visible spectrophotometer (Jasco V-570 UV/VIS/NIR spectrophotometer) in the wavelength ranging from 200-1200 nm. The temperature is varied using a homemade temperature set-up with a soldering rod interfaced with a temperature controller. For easy understanding, the films are renamed and the details are given in table 4.1.

Table 4.1 Deposition conditions of LiNbO₃ thin films used for the present study

Sample	Substrate temperature (°C)	Laser fluence (J/cm²)	Thickness (nm)
LiNbO$_3$ (110) orientation [LN 01]	600	1.52	400
LiNbO$_3$ (300) orientation [LN 02]	600	1.52	400
Polycrystalline LiNbO$_3$ [LN 03]	600	1.52	980
Polycrystalline LiNbO$_3$ [LN 04]	600	1.52	400

4.3 Transmission spectra: Temperature dependence

The characteristic UV transmittance spectra of LN 01, LN 02, LN 03 and LN 04 at the temperatures ranging from 308 to 493 K are given in fig. 4.1. The transmission spectra recorded (200-1200 nm) can be roughly divided into two regions. The high transmission region (~400 - ~1200 nm) has a weak absorption process in visible and near IR region where the transmittance increases with increasing wavelength. After this, there is a strong absorption region (~200 - ~300 nm) leading the transmittance nearly to zero, which generally corresponds to the electron transition between the valence and conduction bands.

It is clear from fig. 4.1 that absorption edge shows a red shift trend with the increasing temperature, the common trend observed in most of the semiconductor materials and few ferroelectrics [Pai Chun Wei et al. (2009)]. The transmittance is not observed to be same for all the films with increasing temperature. The various transmittance may be attributed to the variations in the optical parameters at different temperatures e.g. the dielectric function, optical band gap and thermal expansion [Yang et al. (2010)]. In order to elucidate the temperature effects on the optical band gap in detail, direct and indirect band gaps are plotted in fig. 4.2. It is important to note that the absorbance of the

LiNbO₃ thin films can be directly obtained from the transmittance spectra due to the complete transparency of substrates used in the present study. The absorption coefficient (α) can be calculated if the film thickness is known.
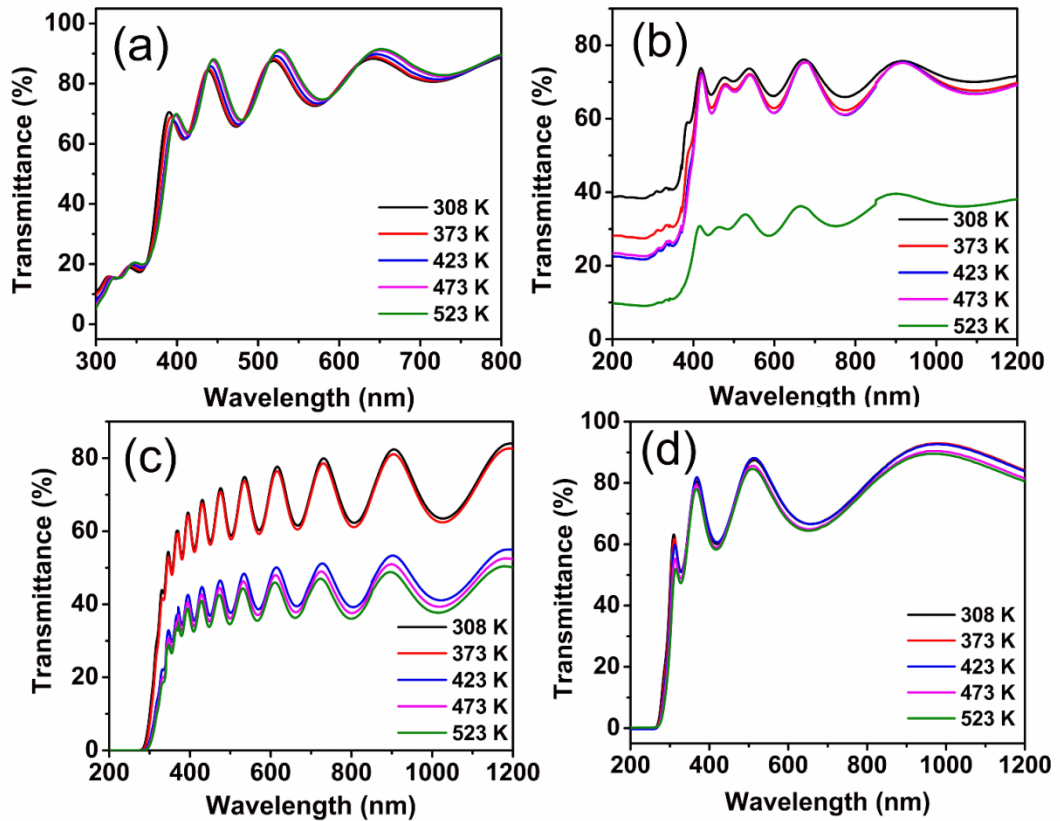
Fig. 4.1 Transmittance spectra of the films in the temperature range from 308-523K

4.4 Optical band gap narrowing: Temperature dependence

Fig. 4.2 shows the direct and indirect band gaps of LiNbO₃ thin films at four typical temperatures 308, 373, 423, 473 and 493 K. There is a significant red shift in direct to indirect band gap for all the LiNbO₃ thin films. Generally, when $E>E_g$ it satisfies the Tauc's power law [Anil Tumuluri et al. (2014)]

$$\alpha h\nu = A(h\nu - E_g)^n \qquad\qquad (4.1)$$

where A is a constant, hν is the photon energy, E_g is the allowed energy gap, n=1/2 for allowed direct transition, n=2 for allowed indirect transition

In the fundamental absorption region (E>E_g), the good linear fitting of (αE)^2 versus E can be seen in fig. 4.2 at all temperatures. For all the plots, the values of E_g are evaluated from the line portion of (αE)^2=0 and are found to be decreasing with increasing temperature. The band gap narrowing trend with increasing temperature can be usually attributed to two factors: thermal expansion of the lattice and band gap renormalization by electron-phonon interaction [Fan Zhang et al. (2013)]. Yang et al. measured optical parameters in the temperature range of 80-500 K for Mn doped $Pb_{0.5}Sr_{0.5}TiO_3$ thin films and correlated the thermally driven shift in band gap to the renormalization of electronic band structure due to collision between electron-electron and electron-phonon [Yang et al. (2010)]. With the supply of external thermal energy, the lattice atoms or ions in their balance sites starts vibrating with higher amplitude leading to anharmonicity and modifies the overlap between the electronic wave functions of neighboring atoms thereby modifying the band gap. Ideally, a pristine material has some band gap. But, with the addition of defects or impurities, the electrons present in the top of the valence band and bottom of conduction band interact with these defect states and shift their energies. The growth of $LiNbO_3$ always couples with the deficiency of Li ion leading to the formation of $LiNb_3O_8$ [Ausrine Bartasyte et al. (2013)]. In the present case, although there are no traces of $LiNb_3O_8$ found from XRD because of its limited resolution but the presence of unreacted or loosely bound Li ions throughout the film grown from deposition technique at higher temperatures (600 °C) cannot be neglected [Anil Tumuluri et al. (2014)].

As mentioned in the chapter 3, the optical band gap of $LiNbO_3$ is detrimental to the valence electronic transitions from 2p orbitals of O^{2-} to the 4d orbitals of Nb^{5+} [Thierfelder et al. (2010)].

In ionic crystals or semiconductors, when the concentration of impurities or defects increases to a certain level, the energy level of impurities may become wider. The concentration of defect states connects to the bottom of the conduction band or the top of the valence band. Therefore, greater the concentration of impurities, the wider is the band tail range resulting in a narrower band gap. Therefore, the transition pertaining to certain band to band tail states may occur prior to an indirect transition with phonon absorption and be present at the lower energy end in the absorption spectrum of the indirect transition [Guo et al. (2015)]. Thus, the unsymmetric absorption humps present in all Tauc's plots in fig. 4.2 accounts for the defect states or impurities. The Nb-O band will affect the forbidden band width directly according to the theory proposed by Didomenico and Wemple [DrDomenico et al. (1969)].

Depending on the preparation conditions, $LiNbO_3$ thin films grow in different orientations allowing the distortion of oxygen octahedron. The change in band structure may be different at different symmetric points in the Brillouin zone. Compared with pure $LiNbO_3$ crystals, thin films of the same will make the bottom of the conduction band at the X and Γ points move upwards and downwards causing the indirect transition energy gap to move towards the ultraviolet [Satapathy et al. (2012)].
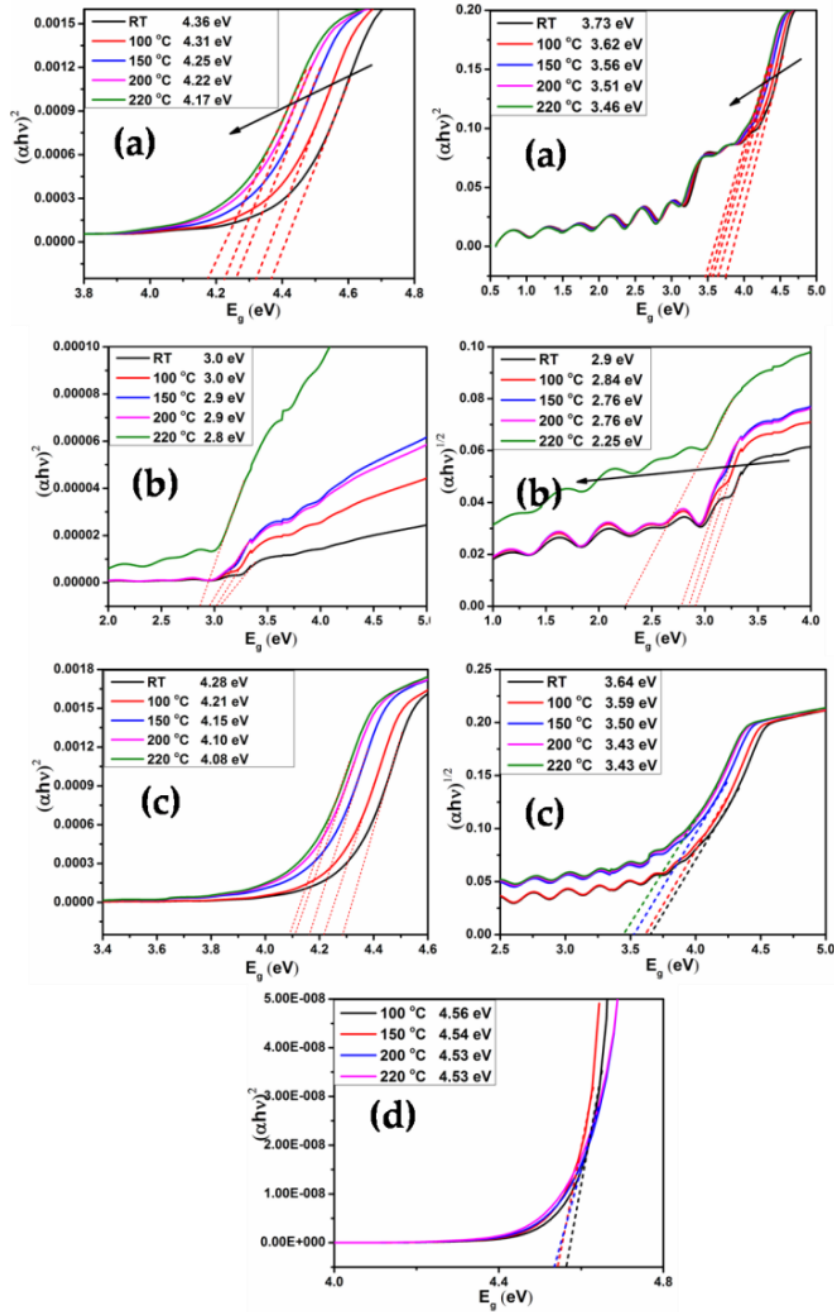
Fig. 4.2 Variations in (αE)² and (αE)¹/² changing with the photon energy are used to determine the optical band gap of the LiNbO₃ films at several typical temperatures

The band gap narrowing coefficient (dE$_g$/dT) of LN 01, LN 02, LN 03 and LN 04 is shown in fig. 4.3. The values of dE$_g$/dT of all the films calculated at different temperatures are given in table 4.2. It is clear from the values that all the films show negative band gap narrowing coefficients. The negative band gap narrowing trend is usually explained by two factors: thermal expansion of the lattice and renormalization of the band structure by electron–phonon interaction. The origin of the positive trend is more complicated. The positive band gap narrowing trend vs. temperature has attracted interest because most semiconductors show negative band gap narrowing trends. Pb$_{1-x}$Sn$_x$Te and Hd$_{1-x}$Cd$_x$Te alloys are well known narrow band gap semiconductors which have both negative and positive band gap narrowing trends depending on the SnTe/CdTe composition [Maksym et al. (2007)].

In general, the temperature dependence of band gap is well explained by Bose-Einstein model [Fan et al. (2013)],

$$E_g(T) = E_g(0) - 2a_B / [\exp(\Theta_B / T) - 1] \qquad (4.2)$$

here, E$_g$(0) is the band gap energy toward 0 K, a_B is the coupling interaction strength, B is the average phonon temperature, and T is the experimental temperature.

The E$_g$(0) value is evaluated by fitting the above model and the values are given in table 4.2. Another important reason is that the strain originating from thermal energy can induce displacement corresponding to the tilting of the oxygen octahedral simultaneously with ferroelectric cation (Li and Nb) displacements [Fernández et al. (2005)]. Therefore, the band gap narrowing with increasing temperature can be attributed to the band gap renormalization due to

the distortion of oxygen octahedra along with the displacement of Li and Nb atoms from their respective lattice sites [Riefer et al. (2016)].
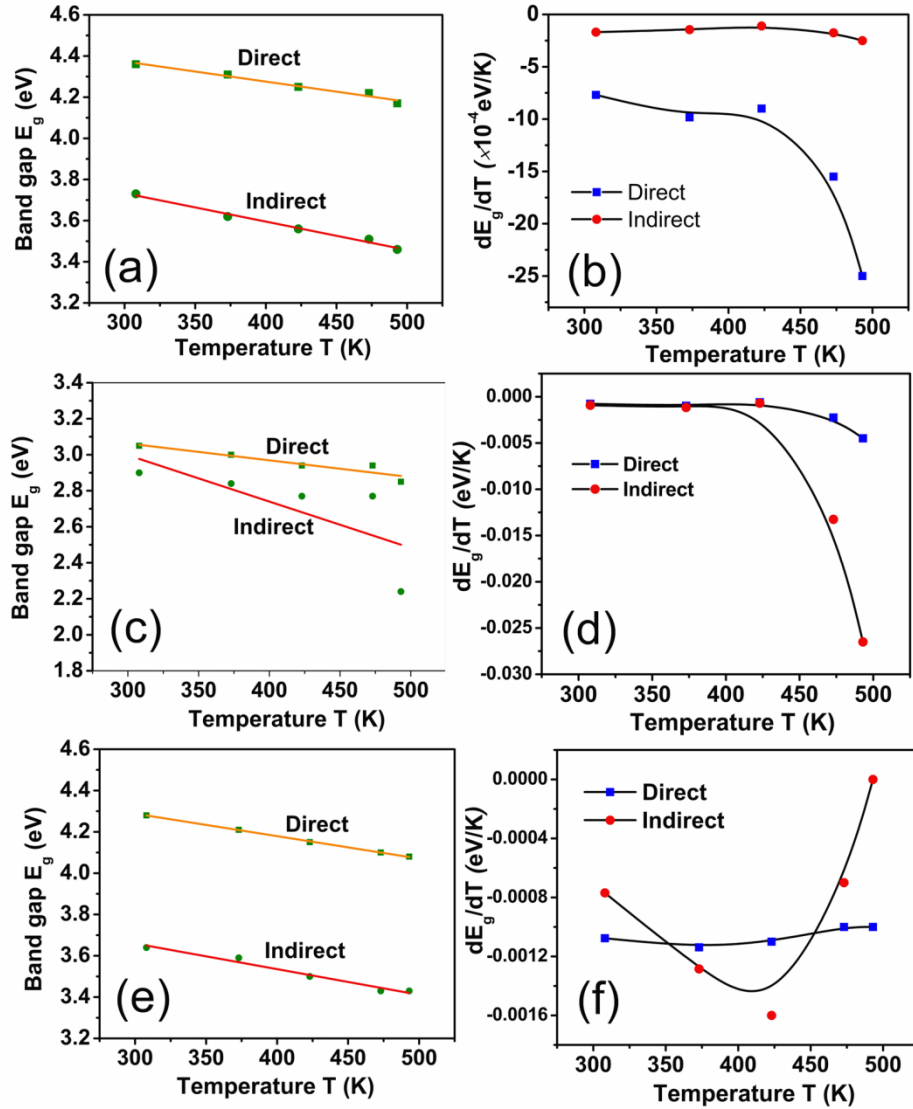

Fig. 4.3 *Temperature dependence of (a) E$_g$ for LN 01 (b) band gap narrowing coefficient for LN 01 (c) E$_g$ for LN 02 (d) band gap narrowing coefficient for LN 02 (e) E$_g$ for LN 03 (d) band gap narrowing coefficient for LN 03*

Table 4.2 The parameter value of $E_g(0)$ and band narrowing coefficient dE_g/dT

Temperature (°C)	LN 01		LN 02		LN 03	
	Direct (eV/K)	Indirect (eV/K)	Direct (eV/K)	Indirect (eV/K)	Direct (eV/K)	Indirect (eV/K)
308	-7.69×10^{-4}	-1.69×10^{-4}	-7.69×10^{-4}	-7.69×10^{-4}	-1.08×10^{-3}	-7.69×10^{-4}
373	-9.84×10^{-4}	-1.45×10^{-4}	-9.84×10^{-4}	-9.84×10^{-4}	-1.14×10^{-3}	-1.28×10^{-3}
423	-9.0×10^{-4}	-1.1×10^{-4}	-6.0×10^{-4}	-6.0×10^{-4}	-1.1×10^{-3}	-1.6×10^{-3}
473	-15.5×10^{-4}	-1.75×10^{-4}	-2.2×10^{-3}	-1.3×10^{-2}	-1.0×10^{-3}	-7.0×10^{-4}
523	-25.0×10^{-4}	-2.5×10^{-4}	-4.5×10^{-3}	-2.6×10^{-2}	-1.0×10^{-3}	----
$E_g(0)$	4.66 eV	4.14 eV	3.34 eV	3.77 eV	4.61 eV	4.03 eV

4.5 Optical constants: temperature dependence and thermo optic coefficient of refractive indices

Fig. 4.4 shows the refractive index (n) and extinction coefficient (k) spectra of LiNbO$_3$ thin films at various temperatures which are extracted from the fitted curve (envelope method) in the wavelength range from 300 to 800 nm. From this figure, it is clear that the refractive indices at all temperatures increases with increasing wavelength in the spectra ranging from 350 to 370 nm, which corresponds to anomalous dispersion regime approaching the maxima and decrease with the increasing wavelength until 800 nm. It is observed that the value of n got red shifted (350 to 370 nm) with increasing temperature in case of LN 01. Contrary to the trend followed by refractive index (n), the extinction coefficient (k) started decreasing with increasing wavelength. In case of LN 02, the value of n did not red shifted but rather increased in value from 2.3 to 3.1 with increasing temperature. The extinction coefficient also followed the same trend and the value (k) got increased with temperature as shown in fig. 4.4. In

case of LN 03, both n and k increase with increasing temperature. Again LN 04 followed the same trend as of (110) LN.
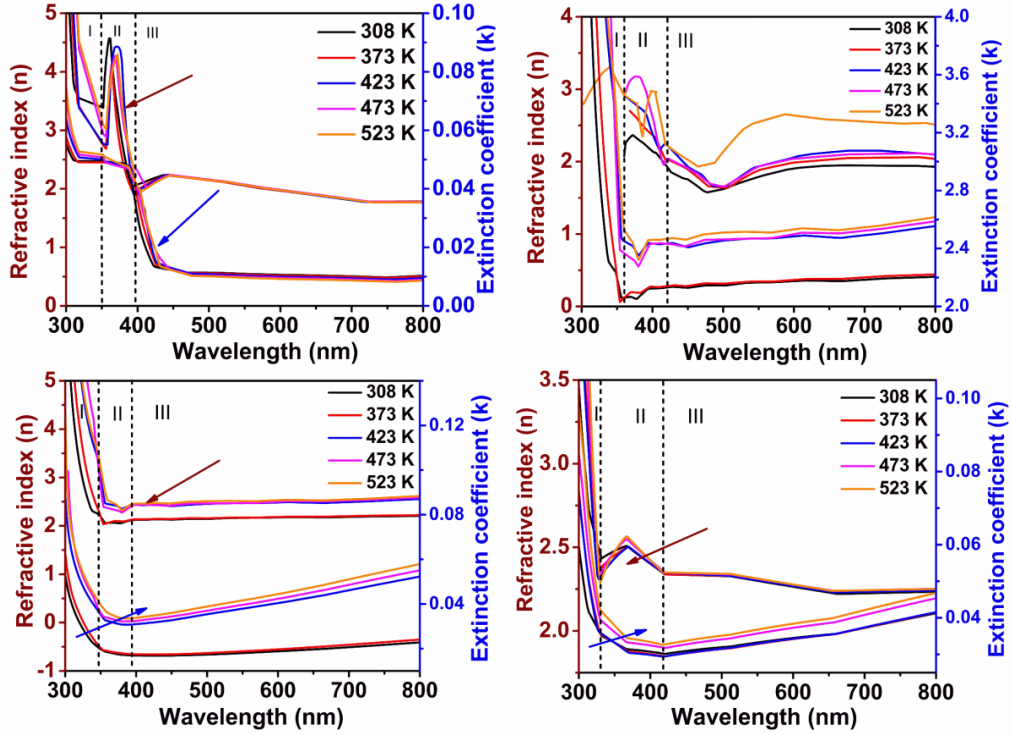
Fig. 4.4 Real and imaginary parts of the refractive index for temperatures from 308 K to 523 K

In general, the two main factors explaining the temperature dependence of refractive index (n) are electronic polarizability and thermal expansion [Gorachand Ghosh et al. (1994)]. This is described by Prod'homme model [Silva et al. (2007)] in which the two contributing factors are correlated through Lorenz-Lorenz equation and are given as

$$dn/dT = \frac{(n^2-1)(n^2+2)}{6n}(\phi - \beta) \qquad (4.3)$$

ϕ =(1/P)(dP/dT) is the temperature coefficient of electronic polarization (P), β is the volume expansion coefficient.

The temperature variation of the refractive index (n) results from the entangled change in polarisability (α) of the electron cloud and density N of the material.

$$dn / dT \sim \alpha(dN / dT) + N(d\alpha / dT) \tag{4.4}$$

The polarisability accounts for the proportional relation between the external electric field E and the resulting dipole moment

$$p = \alpha E \tag{4.5}$$

Thus α quantifies the distortion of an atom's or molecule's electron cloud induced by an external electric field (polarisability) which gives rise to refractive index.

Thermo optic coefficient dn/dT is calculated for all LiNbO$_3$ thin films. The typical thermo refractive coefficient dn/dT for all LN thin films at different temperatures is given in table 4.3. For LN 01, the maximum thermo refractive coefficient shows a well defined maximum with magnitude of 1.87×10^{-4} K^{-1} at 423 K. It is also observed that dn/dT becomes negative at elevated temperatures (473 and 493 K). According to Prodhomme's empirical formulation, the sign of the thermo-optic coefficient is determined by the difference between the electronic polarization coefficient and the thermal expansion coefficient for glasses [Hongxia Li et al. (2007)]. If the former dominates, the thermo-optic coefficient is positive, while the latter's domination results in negative thermo optic coefficient [Hussain Ali Badran et al. (2014)]. So, the same cannot be applicable for ferroelectrics. But, there are chances for loosely bound Li ion to migrate within the unit cell resulting in negative thermo optic coefficient. In case of LN 02, the maximum thermo optic coefficient is observed to be 1.53×10^{-2} K^{-1} at 473 K. With

increasing temperature, dn/dT is found to be increasing. The rise in temperature disturbs the unit cell, thereby increasing the polarisability and hence thermo optic coefficient. From previous reports, changes in dn/dT for Sb thin films are attributed to the transformation between crystalline and melted states upon focusing the laser beam [Tripura Sundari et al. (2013)]. In case of TiO_2 films grown by atomic layer deposition, the change in the dn/dT has been attributed to changes in porosity of the films [Fan Zhang et al. (2013)]. For LN 04, dn/dT does not show much difference in order of which is clearly distinctive among LN 01, LN 02 and LN 03. The changes observed in refractive indices with temperature can be attributed to the structural dissimilarity and the distinct defects states present in LN films under study.

Table 4.*3 Thermo-optic coefficient of real (dn/dT) and imaginary parts (dk/dT) of refractive index from 308 K to 493 K*

Temp. (°C)	LN 01		LN02		LN03		LN04	
	Refractive index (n)	dn/dT (K^{-1})	Refractive index (n)	dn/dT (K^{-1})	Refractive index (n)	dn/dT (K^{-1})	Refractive index (n)	dn/dT (K^{-1})
308	2.05	-7.69×10^{-5}	1.78	1.37×10^{-3}	2.16	9.84×10^{-5}	2.29	9.07×10^{-5}
373	2.05	5.65×10^{-5}	1.87	1.24×10^{-3}	2.17	3.02×10^{-3}	2.30	2.23×10^{-5}
423	2.06	1.87×10^{-4}	1.93	5.53×10^{-4}	2.46	2.98×10^{-3}	2.30	6.1×10^{-5}
473	2.07	-7.3×10^{-5}	1.93	1.53×10^{-2}	2.46	1.09×10^{-3}	2.31	1.19×10^{-4}
493	2.06	-3.3×10^{-5}	2.54	3.07×10^{-2}	2.51	2.15×10^{-3}	2.31	7×10^{-5}

In summary, the temperature-dependent optical properties of pulsed laser deposited $LiNbO_3$ thin films were characterized by UV-Visible spectrophotometer with the temperature ranging from 308 to 493 K. Changes in optical band gap and negative band narrowing coefficient (which is about 10^{-3} to 10^{-5} eV / K) are observed. The changes are attributed to the band gap

renormalization due to the distortion of oxygen octahedra. Thermo optic coefficient (dn/dT) for the same was extracted and is positive for all the films. These results could lead to the usage of $LiNbO_3$ thin film based photonic devices in optoelectronic and integrated optic applications at different temperatures.

Chapter 5

Synthesis of $Zr_{0.8}Sn_{0.2}TiO_4$ ceramics using gel casting and their microwave dielectric properties

In this Chapter, synthesis and forming of dielectric resonators are explained through a slurry based route involving organic/Inorganic carrier medium. The main emphasis is on optimizing the conditions to get ($Zr_{0.8}Sn_{0.2}$) TiO_4 ceramics. An inexpensive polyethylene mould is used for the fabrication of dielectric resonators. This is a critical requirement for the synthesis of porous ZST for fluorescence quenching based explosive sensor realization. ($Zr_{0.8}Sn_{0.2}$)TiO_4 ceramics processed using this technique were sintered at 1400 ºC and exhibited desirable microwave dielectric properties of $\epsilon_r=37$, $Qxf=32000$ and $\tau_f =+6$ ppm/ºC, which is comparable with the dielectric resonators of this composition prepared by the ceramic route. Here the advantage is the low cost approach to achieve the desired shapes, even complex shapes.

5.1 Introduction

The wireless and cellular technology grows drastically day by day in today's era. The technology demands high quality microwave components for diverse applications. Components such as dielectric resonators, microwave filters and antennas with different shapes and sizes have been used in defense and aerospace as well as in commercial applications [Ahmed A. Kishk et al. (2002), Dipali Soren et al. (2014), Long fang Zou et al. (2011)]. Ceramics are a class of insulating materials that possess chemical durability, properties invariant with thermal and mechanical changes which enable them to be used for the above mentioned applications. For this reason some of the microwave components are made up of ceramic materials with optimized electrical and magnetic properties. Variety of oxide materials like $Zr_{0.8}Sn_{0.2}TiO_4$, $Ba(Zn_{1/3}Ta_{2/3})O3$, $Nd(Mg_{0.5}Sn_{0.5})O_3$, $AMoO_4$–TiO_2 (A=Ca, Sr), $MgZrNb_2O_8$, $SrRAlO_4$ (R=Sm, Nd, La) were proposed and studied for the above mentioned applications till date [Xie Cheng Fan et al. (2008), Ying Cheng et al. (2013), Nedelcu et al. (2011), Jing Guo et al. (2013), Yih-Chien Chen et al. (2011), Huang et al. (2001)]. They have the added advantages like low absorption of moisture. In general, microwave dielectrics can be used in filters, radome, substrate and antennas for desired frequency ranges [Xie Cheng Fan et al. (2008)]. Hence fabrication of a successful microwave dielectric ceramics needs tailoring of their material properties for the same applications for example, a microwave dielectric resonator needs to have features like high dielectric constant, low loss and near zero temperature coefficient of resonant frequency to become useful for filter, resonator or antenna applications [Nedelcu et al. (2011)].

A high dielectric constant material miniaturizes the resonator since the volume of the resonator is inversely proportional to the dielectric constant. The

minimization of a resonator with change in dielectric constant is shown in fig. 5.1(b). The relation between volume and permittivity of a resonator can be expressed as follows:

$$f = \frac{233}{\sqrt{\varepsilon}V^{1/3}}$$

(5.1)

where f is the resonant frequency, ε is the permittivity of the material and V is the volume of the material

Low loss of the material enhances the storage of energy within it, which can be quantified using the quality factor (Q). The quality factor of the resonator is defined as the ratio between the microwave energy stored in the resonator to that dissipated in it per cycle. This gives insight into the losses present within the material that is represented by:

$$\tan\delta = \frac{\varepsilon''}{\varepsilon'}$$

(5.2)

$$\text{Quality factor}(Q) = \frac{1}{\tan\delta} = \frac{\varepsilon'}{\varepsilon''}$$

(5.3)

Therefore, higher the quality factor, lower the energy dissipation within the resonator. The resonant frequency of the resonator should be stable between 30-120 $^{\circ}$C. However materials exhibit slight changes in resonant frequency with temperature, owing to temperature dependence of dielectric constant and thermal expansion. The mathematical expression of τ_f can be given as:

$$\tau_f = \frac{\Delta f}{f} \cdot \frac{1}{\Delta T}$$

(5.4)

where f (GHz) is the resonant frequency at ambient temperature, Δf (MHz) is the shift in resonant frequency, ΔT (^{o}C) is the temperature range.

The theory behind dielectric resonators and their properties are described below. A dielectric resonator is a ceramic puck with desired dimensions that exhibits resonance in narrow range of frequencies particularly in microwave range. The electric and magnetic field distributions in a dielectric resonator are given in fig. 5.1 (a) [Yikai Chen et al. (2015)].
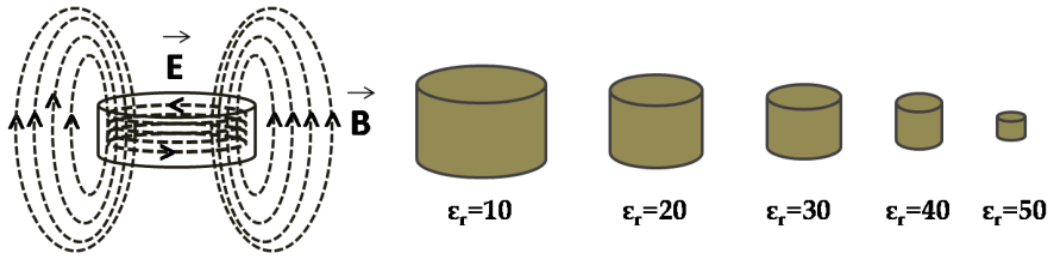

Fig. 5.1 (a) Electric and magnetic field distribution (TE~01δ~ mode) in dielectric resonator

(b) Change in volume of dielectric resonator with increasing permittivity for the same frequency and mode

In order to use ceramics for dielectric resonator, radome, substrate or antenna applications the materials are to be designed and fabricated in appropriate geometries like rectangular, spherical, cylindrical, conical and hemispherical etc. Resonators will store microwave energy in some geometries while the same materials can be used to radiate energy in some other geometry, which is required for antenna applications [Ashok Kumar Jyani et al. (2013)]. The geometry in applications like radomes is indeed quite complex. In these applications geometry plays as important a role as material properties. These shapes with good density are difficult to fabricate using traditional methods like die pressing [Xiong et al. (2005)]. Therefore, there is a need of dielectric materials

to be fabricated in different shapes without altering their basic material properties.

Gel casting is a facile technique by which near-net, high quality intricate shapes can be processed [Jinlong Yang et al. (2011)]. The ceramic powder is dispersed in a water based carrier with monomer and cross linker as binder system in order to get the stable highly solid loaded suspension with low viscosity. Polymerization of monomers leads to a cross-link network with the addition of initiator and catalyst. Thus formed slurry can be cast into a mold of desired shape to form net shaped dielectric material ready for application. High mechanical properties, ease in fabrication of complicated shapes and comprehensive use for variety of forming materials made gel casting a feasible technique for industrial applications [Ogbemi et al. (1997)]. Moreover, optimization of material parameters like grain size and addition of foreign particles in the slurry to get densification into a porous ceramics is advantageous in some applications like sensors. Gel casting is widely used in industries for reproducible properties of ceramics. In general, gel casting can be done from aqueous and nonaqueous solvents. In nonaqueous solvents, toxicity of materials, environmental and health hazards, expensive precursors etc. became a deterrent against their widespread use [Santanu et al. (2011)]. For this reason, aqueous gel casting became the dominant process. The steps involved in their synthesis procedure are given in section 5.2.

$Zr_{0.8}Sn_{0.2}TiO_4$ (ZST), a solid solution of ZrO_2, TiO_2 and SnO_2 is well investigated for its microwave dielectric properties so as to use them in microwave applications such as resonators, antennas, oscillators and filters [Olhero et al. (2014)]. ZST is derived from $ZrTiO_4$ and forms a solid solution with

partial substitution of Zr^{4+} with Sn^{4+} at 20% level yielding a temperature compensated, low loss material suitable for microwave applications. $ZrTiO_4$ is a well studied compound but have low temperature coefficient of resonant frequency [Freer et al. (2008)].

5.2 Gel casting procedure and steps involved

High purity powders of ZrO_2 (99.9%, Nuclear fuel complex), SnO_2 (99.9%, Sigma aldrich) and TiO_2 (99.9%, Sigma aldrich) were weighed as per stoichiometric ratio and mixed using planetary ball mill at a speed of 150 rpm and calcined at 1300 ^oC for 1min. Initial reagents along with distilled water were mixed using zirconia balls in a ball mill by keeping the powder to ball ratio as 1:2. This mixture is dried in hot air oven and calcined at 1300 ^oC for 1 min followed by dry milling to break the hard agglomerates formed during calcination. Dry milling avoids the particle agglomeration and grain size reduction. The experimental procedure is given in chapter 2 in detail.

As mentioned previously, gel casting can be done through aqueous and nonaqueous routes. The primary components required for the fabrication of aqueous gel casting is

1. Dispersant (helps in suspension of powder particles)
2. Monomer (forms a basic polymer network)
3. Cross linker (links each individual polymer to get cross linking network)
4. Initiator (to start gelation reaction)
5. Catalyst (accelerates the gelation reaction)

The premix solution is prepared by dissolving methacrylamide (monomer) and N,N'-methylenebisacrylamide (cross linker) in distilled water at 6:1 ratio. The foremost step is to prepare slurry by adding ZST powder to premix solution along with 1.5 wt.% of dolapix 88 as optimized dispersant. This mixture is milled with zirconia balls at a rate of 10 rpm to avoid formation of agglomerated particles in slurry. To promote the gelation reaction, ammonium per sulphate (APS) as initiator and Tetra ethyl methylenediamine (TEMED) as catalyst were added to the slurry. This gel is poured into different mould materials of desired shapes and thereafter drying in humidity controlled chamber. After drying, the samples are demolded, debinded and sintered at different temperatures.
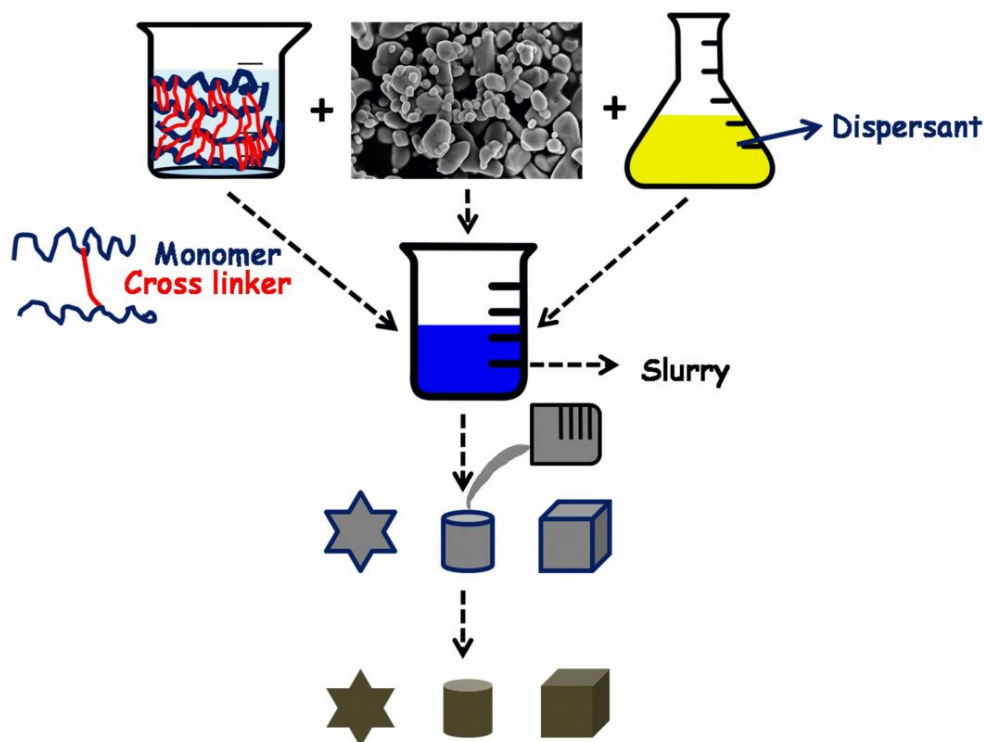

Fig. 5.2 Pictorial representation of gel casting process

ZST can be used efficiently if the fabrication of different shapes is possible without further machining. In the present chapter, dielectric resonators made of ZST in different shapes are fabricated by adapting gel casting technique. Conditions like choice of dispersant, monomer to cross linker ratio and mould material were optimized. In addition, the studies on colloidal stability of the suspension and phase determination are discussed in detail. Since the ZST is a well known dielectric resonator material and possess excellent microwave dielectric properties, it will be interesting to see if these properties are retained after subjecting it to a fabricating process with many steps as in the case of gel casting. In addition, luminescence of ZST is studied by synthesizing and sintering both porous and nonporous form of it to check the difference in emission characteristics with an excitation of light with a given wavelength.

5.3 Discussion on achieving optimized conditions for gel casting of ZST

5.3.1 Sedimentation height analysis and zeta potential

In order to make slurry, the ZST powder particles were to be suspended in premix solution which consists of polymer solution. When powder particles were suspended in liquid medium, the particles influenced by forces like gravity and Brownian motion tend to settle down. This should be avoided by using various dispersants where the dispersants form identical surface charge around the particle and develops a repulsive force against each other [Zawrah et al. (2015)]. Therefore, the state of dispersion and its stability is accounted in terms of particle settling rate or sedimentation height [Saralasrita Mohanty et al. (2013)].

The sedimentation analysis estimates the degree of dispersion stability of powder particles in premix solution with time.
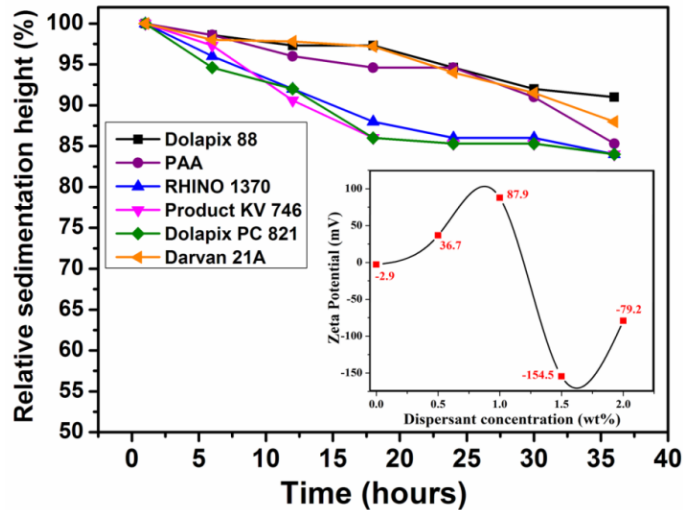

Fig. 5.3 Sedimentation height analysis for ZST suspended in aqueous media with different dispersants

For ZST particles dispersed in premix solution along with 0.5 wt.% of different dispersants used in the present study, the relative sedimentation height vs. time is given in fig. 5.3. From the plot, it is clear that Dolapix88 is showing best dispersibility even after 36 h. The amount of flocculation can be given in terms of zeta potential. The stability of the slurry mainly depends on the resistance of the powder particles to flocculation. The inset of fig. 5.3 depicts the zeta potential with varying concentration of dolapix88. It is well known that higher the zeta potential, higher will be the repulsive energy between the particle and more stable the suspension will be. Dispersant with 1.5 wt.% has best zeta potential of -154.5 mV and thereafter the zeta potential decreased. Therefore, dolapix 88 of 1.5 wt.% is found to be the best dispersant and optimized amount for ZST. So, the same amount of dolapix 88 is used for all the gel casting of ZST.

5.3.2   Structural studies

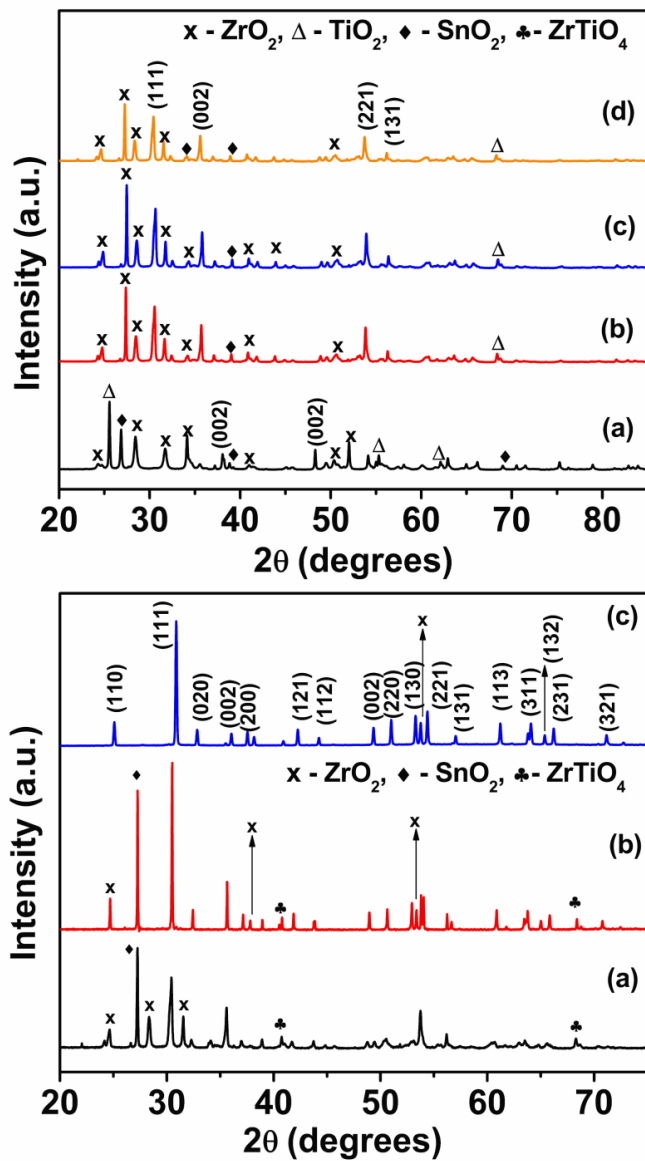Fig. 5.4 (I) XRD patterns for (Zr₀.₈Sn₀.₂)TiO₄ (a) ZrO₂-SnO₂-TiO₂ mixture after ball milling (b) after calcination (c) After particle size reduction (d) Green pellet after casting

(II) (a) sintered at 1200 °C, (b) sintered at 1300 °C (c) sintered at 1400 °C.

Fig. 5.4(II) (a)-(c) illustrates the XRD patterns of ZST ceramics sintered at different temperatures. At 1200 °C, ZrO_2 and SnO_2 were found along with $Zr_{0.8}Sn_{0.2}TiO_4$ where as at 1300 °C, few more $Zr_{0.8}Sn_{0.2}TiO_4$ peaks were originated with decreasing secondary phases. The peaks from ZrO_2 and SnO_2 were suppressed by enhancing $Zr_{0.8}Sn_{0.2}TiO_4$ phase. The ceramics sintered at 1200 °C and 1300 °C has $Zr_{0.8}Sn_{0.2}TiO_4$ with unreacted ZrO_2 as a dominant phase along with traces of $ZrTiO_4$. It is evidenced that $Zr_{0.8}Sn_{0.2}TiO_4$ phase is formed at 1400 °C with orthorhombic structure (JCPDS database: 81-2214) and were consistent with previous reports [Pamu et al. (2012)]. At 1400 °C, $Zr_{0.8}Sn_{0.2}TiO_4$ is formed completely with minor traces of $ZrTiO_4$ owing to the SnO_2 deficiency. This is due to higher sintering temperature close to the melting point of tin oxide (1630 °C) and is identified as smaller grains in fig. 5.4II (c) [Ioachim et al. (2003)].

5.3.3 Microstructure

The microwave dielectric properties of sintered ceramics are strongly dependent on the micro structural features such as porosity, grain size and its bulk geometry [Rick Ubic et al. (2010)]. Fig. 5.5(a)-(d) demonstrates the microstructure of ZST during the synthesis from powder to casted green pellet. The as mixed initial reagents are highly agglomerated with smaller grain size as displayed in fig. 5.5 (a). The calcined powder particles in fig. 5.5(b) are not highly agglomerated with varying and increased grain size. There is not much significant change in morphology after particle size reduction which is done to decrease the roughness of the powder particles. After mixing the premix solution, dispersant and ceramic powder at low speeds, the grains are of uniform size and shape as shown in fig. 5.5 (d). At some places the grain growth is found to be intermediate with tetrahedral shape as shown encircled in fig. 5.5 (d).
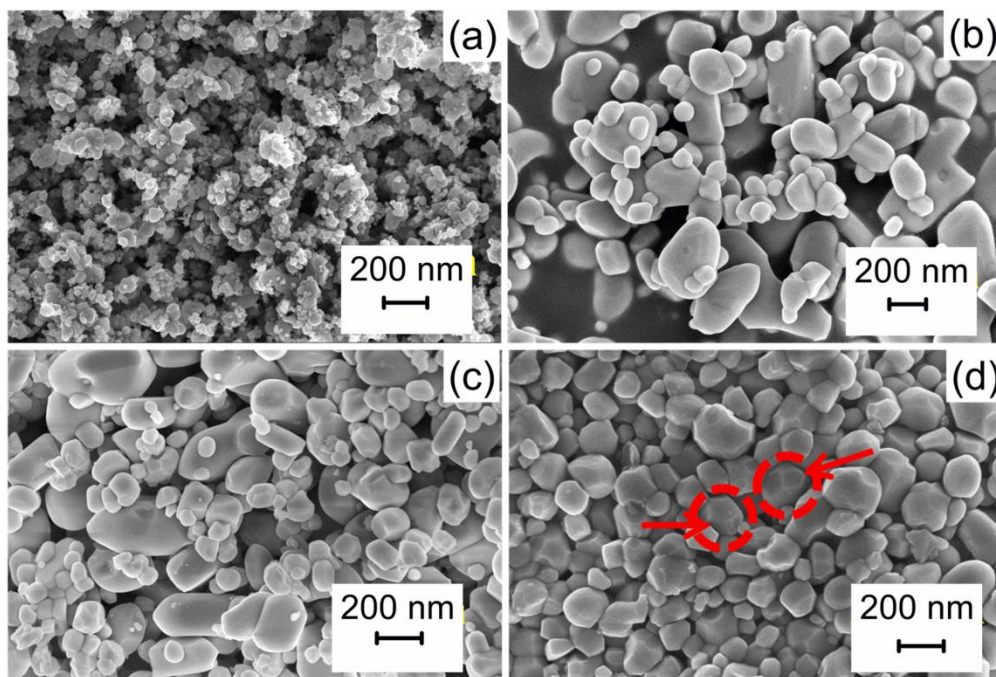
Fig. 5.5 Microstructure of (a) ZrO₂-SnO₂-TiO₂ mixture after ball milling (b) after calcination (c) After particle size reduction (d) Green pellet after casting

The morphology of ZST ceramics and their corresponding average grain size distribution at different sintering temperatures is depicted in fig.5.6. ZST ceramics sintered at 1200 $^{\circ}$C is highly porous and the grains are bar shaped with varying length in microns as in fig. 5.6(a). In 5.6(b) the bar shaped grains started to coalesce and diffuse resulting in bigger grains with reduced porosity. Further increase in sintering temperature significantly promotes the grain growth, resulting in highly densified ceramics with well defined grain boundaries as shown in fig. 5.6(c). The densities of ZST ceramics sintered at different temperatures are given in table 5.1.
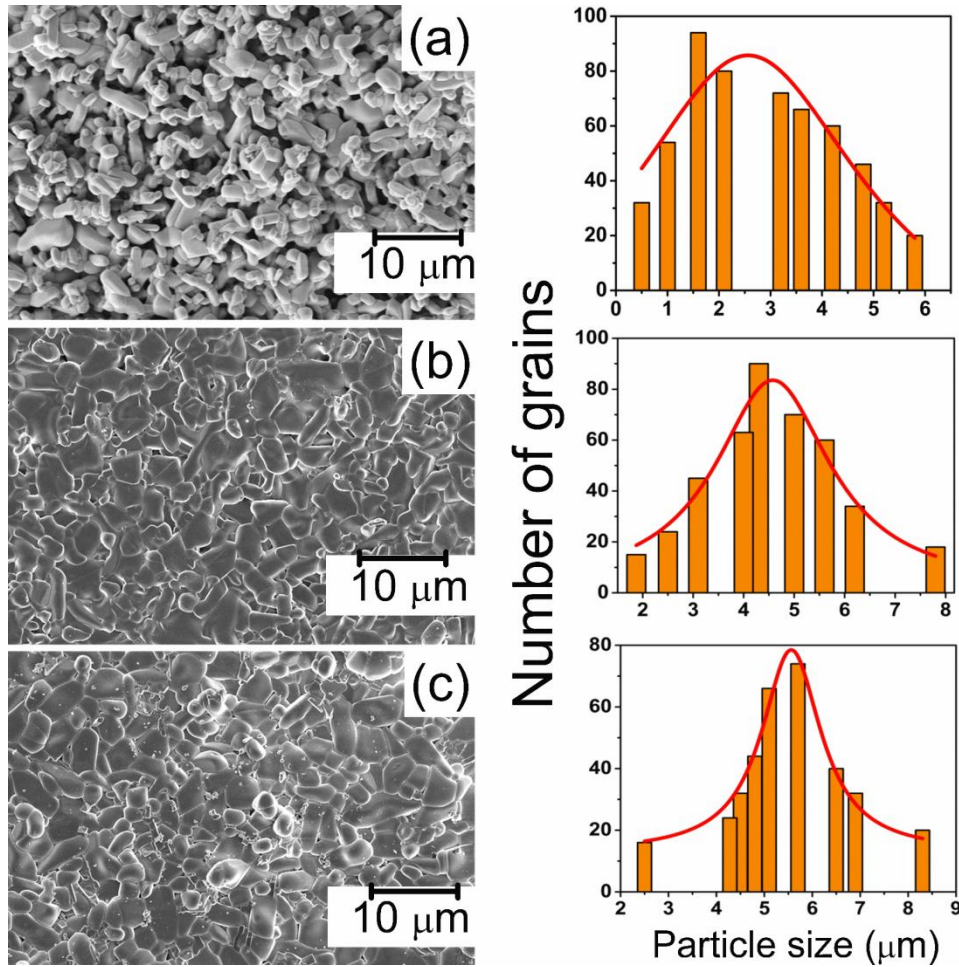
Fig. 5.6 *Microstructure and corresponding average grain size of (Zr$_{0.8}$Sn$_{0.2}$)TiO$_4$ (a) sintered at 1200 ^{o}C (b) sintered at 1300 ^{o}C (c) sintered at 1400 ^{o}C.*

5.3.4 Microwave dielectric properties

Microwave dielectric properties of any material is highly influenced by both intrinsic parameters like ionic polarizability, structural features and extrinsic parameters like porosity, oxygen deficiencies, secondary phases or two dimensional defects like grain boundaries [Ghasemi et al. (2009), Ramarao et al. (2015)]. By optimizing the external processing conditions, the extrinsic losses can

be tuned to get the best microwave dielectric properties. Intrinsic properties can be influenced only by changing the composition itself.

Table 5.1 shows the microwave dielectric properties of ZST ceramics measured around 5-7 GHz which are sintered at different temperatures. The dielectric constant has improved with increase in the sintering temperature. Dielectric constant is highly sensitive to polarizability and porosity. From XRD in fig. 5.4, it is clear that TiO_2, $ZrTiO_4$ and SnO_2 phases coexist at 1200 ^oC. The ionic polarizabilities of $ZrTiO_4$ (14.22 $Å^3$), SnO_2 (6.85 $Å^3$), TiO_2 (6.95 $Å^3$) and $Zr_{0.8}Sn_{0.2}TiO_4$ (14.14 $Å^3$) were calculated from Shannon's additive rule [Di Zhou et al. (2014), Guo Jing et al. (2013)]. Since $ZrTiO_4$ is commonly observed in all the sintered ZST ceramics, the contribution of polarizability from $ZrTiO_4$ will be the same and hence it cannot be considered as a factor for the increase in dielectric constant. ZST sintered at 1200 ^oC and 1300 ^oC have TiO_2 as the dominant phase whose ionic polarizability is less compared to $Zr_{0.8}Sn_{0.2}TiO_4$. This leads to the relatively lower dielectric constant at 1200 ^oC and 1300 ^oC when compared to 1400 ^oC. Porosity is another important parameter to be considered for the decrease in dielectric constant for ZST sintered at lower temperatures. The porosity corrected dielectric constant (ε_{rc}) can be calculated [Penn Stuart et al. (1997)].

$$\varepsilon_r = \varepsilon_{rc}\left(1 - \frac{3P(\varepsilon_{rc}-1)}{2\varepsilon_{rc}-1}\right) \tag{5.5}$$

where ε_r the experimental dielectric is constant, ε_{rc} is the porosity corrected dielectric constant, P=1-D is the fractional porosity where D is the fraction of material's theoretical density.

Quality factor (Q×f) of any microwave dielectrics depends on density, secondary phases and grain size [Haung Cheng et al. (2000)]. In addition, packing fraction gives more insight into the change in quality factor,

$$\text{Packing fraction} = \frac{\text{Volume of packed ions}}{\text{Volume of primitive unit cell}} \times Z \qquad (5.6)$$

where Z is the number of formula units per unit cell.

In the present case, the calculated packing fraction is 40.1, 40.3 and 41 % at 1200 ℃, 1300 ℃ and 1400 ℃ respectively. The grain size also affects the dielectric loss of the material where the dielectric loss decreases with reduction in number of grain boundaries per unit volume which act as two dimensional defects. The relative decrease in packing fraction and grain size at 1200 ℃ and 1300 ℃ resulted in increase of dielectric loss, as a reduced packing fraction gives more degree of freedom for the ions to respond to an applied external electric field. The Q×f value reached a maximum value of 32000 at 1400 ℃.

Temperature coefficient of resonant frequency (τ_f) of any material gives the stability of the material with change in environmental conditions [Ioachim et al. (2003), Ubic Rick et al. (2010)]. The deviation of τ_f from zero is explained by the presence of TiO_2 as a secondary phase as well as porosity. Significant TiO_2 phase and porosity at 1200 ℃ and 1300 ℃ sintered ZST ceramics resulted in much deviation from zero value for τ_f. With increase in sintering temperature, τ_f approaches close to zero. This can be attributed to the pure phase of ZST with minor secondary phases as well as to the reduction in porosity.

Table 5.1: Microwave dielectric properties of ZST ceramics sintered at different temperatures

Sintering temperature and duration (°C)	Avg. grain size (μm)	Density (%)	Experimental Dielectric constant (ε$_r$)	Porosity corrected (ε$_r$)	Q×f (GHz)	τ$_f$ (ppm/°C)
1200-3h	2.6	90	35	41	18000	9
1300-3h	4.3	96	36	38	29000	7
1400-3h	5.1	97	37	39	32000	6

The microwave dielectric properties of ZST ceramics can be further enhanced with inclusion of additives like V$_2$O$_5$, WO$_3$, Ta$_2$O$_5$, NiO and CuO along with ZnO [Mailadil Sebastian et al. (2008)], which can influence the composition by aiding densification thereby reducing porosity, increasing uniform grain size.

Fig. 5.7 Zr$_{0.8}$Sn$_{0.2}$TiO$_4$ gel after casting in plastic and glass moulds

Fig. 5.7 depicts the (Zr$_{0.8}$Sn$_{0.2}$)TiO$_4$ gel after casting in different mold materials like glass and polyethylene. The applicability of mold materials like glass, polyethylene, anodized aluminum and Teflon were tested and their

advantages in fabrication are compared in Table 5.2. Polyethylene molds were found to be best suitable for ZST where the advantages like mold release, inexpensive and ease in fabrication can be widely applicable for industrial applications.

Table 5.2: Summary of different mould materials used in the present study for ZST ceramics

S.No.	Material	Advantages	Disadvantages	Applicability
1.	Polyethylene	Inexpensive and moldable	Difficult to machine and limited shapes	Circular disks, Cylinders, Rectangular Substrates, hemispherical etc.
2.	Glass	Inexpensive and readily available	Limited shapes	Initial Lab tests for plates and rods
3.	Anodized aluminium	Machinable and inexpensive	Material sticking at the edges	Not recommended for ZST
4.	Teflon	Machinable and inert	Very poor release.	Not recommended for ZST

Zr$_{0.8}$Sn$_{0.2}$TiO$_4$ ceramic powder with ZrO$_2$, TiO$_2$ and SnO$_2$ as initial reagents is prepared through mechanical milling (ball milling). Particle size and shape are optimized so as to obtain highly densified ceramic bodies. Slurry is prepared with the ZST ceramic powder in water along with a suitable dispersant, monomer(s) and cross linker. The slurry is molded in a mold of desired shape and polymerization of slurry in the mold is triggered. The polymerized product is subjected to controlled drying process in order to get rid of the excess water and thus to obtain firm green ceramic body. If necessary, machining or grinding

of the green product is done to get a net-shaped component with fine surface finish. The final product is heat treated in a controlled fashion to remove polymers and then to increase the density of the product.The obtained microwave dielectric properties of the resonators, ε_r= 37, Q×f = 32000 and τ_f = 6 ppm/^{o}C are comparable with the previous reports. These resonators are useful for a wide range of applications like dielectric resonator antenna, oscillators and filters.

Chapter 6

Explosive molecules sensing from $Zr_{0.8}Sn_{0.2}TiO_4$ porous substrates through fluorescence quenching

In the present chapter, details of porous $Zr_{0.8}Sn_{0.2}TiO_4$ made using gel casting with different pore forming agents like baking soda, ethyl cellulose and starch are discussed. The substrates have multi emission peaks in green, orange and red regions with an excitation wavelength of 355 nm. When an analyte of TNT, RDX and CL 20 were in contact with ZST, the fluorescence emission quenched with time as well as with analyte concentration. The quenching efficiency of each analyte and their mechanism are discussed in detail. Analyte diffusion through porous matrix and the sensing performances are analyzed. The main mechanism involved in fluorescence quenching is the photo induced electron transfer between the excited state of the indicator and the ground state of the explosive compound. TNT is found to be an effective analyte for diffusion through porous $Zr_{0.8}Sn_{0.2}TiO_4$ substrates. These porous substrates exhibit fast, sensitive, inexpensive and highly selective fluorescence quenching. The quenching efficiencies varied to CL 20, TNT and RDX. The materials developed in this work have extensive potential in sensing applications due to the ease in fabrication, high mechanical strength and tunability in porous structures as well as reusability by removing the analytes at high temperatures by heating since the substrates are ceramics.

6.1 Introduction

The detection of explosive molecules is of prime concern for military operations, homeland security and environmental toxicity. The trace level presence of many explosives based on nitramines, nitro aromatic, nitro alkanes, peroxides and nitro ester are to be detected [Meaghan et al. (2009)]. The widespread use of explosives for military purposes increase the environmental contaminants which leads to health threats (for both animals and humans) in the form of Anemia, Carcinogenicity, Abnormal Liver function, Skin irritation etc. Therefore, sensitive and cost effective detection could provide rapid warning to the environmental hazards and offer appropriate feed-back in remediation of contaminated sites [Shu- Ran Zhang et al. (2014)]. Most of the explosives used for different applications were broadly categorized based on their vapour pressure [Jennifer L. Novotney et al. (2013)].

Typically, nitro aromatics (e.g., 2, 4, 6-trinitrotoulene and 2, 4-dinitrotoulene) are used for military applications [Gokcen Birlik Demirel et al. (2013)]. Nitramines and Nitrate Esters (e.g.; 3, 5-trinitroperhydro-1, 3, 5-triazine (RDX) and Penta Erythritol Tetra Nitrate (PETN)) are the primary components of highly energetic explosives [Richard G. Smith et al. (2008)]. Ammonium salts like Ammonium Phosphate (AP) and Ammonium Nitrate (AN) are widely used in rocket propellants [Qi-Long Yan et al. (2016)]. Peroxide based molecules like Triacetone Triperoxide and Hexamethylene Triperoxide Diamine are used for homemade explosives because of their simple and inexpensive synthesis [Salles et al. (2014)]. Almost all the nitrated explosives are sensitive to shock, friction and impact. Hence, the detection techniques that are contact free are highly desirable.

Techniques that are well known and currently followed are canine teams, metal detectors, X-ray dispersion, Ion Mobility Spectroscopy (IMS) and optical methods [Meaghan et al. (2009)]. Each of the above has their own advantages and disadvantages. Canine teams involve dogs for discrimination between target molecules and are commonly used for detection. The well trained canines are the most sensitive method of detection and highly responsive to trace level vapors. But, the main drawback is that the trained dogs are expensive and easily get tired [Xiangcheng Sun et al. (2015)]. Ion Mobility Spectrometry (IMS) is a well known explosive detection technique. The disadvantages which cannot be ruled out includes low resolution, chemical contamination issues and instrument calibration [Meaghan et al. (2009)]. X-ray detection of explosives is also widely used to image baggage and humans since X-rays can penetrate. These are used at the transportation hubs like airports, railway and bus stations. The X-ray scattering is able to detect a bomb whereas unlikely to identify the trace level explosive molecules. This is an advantage to carry explosives in portable manner or in dismantled pieces. Although metal detectors are most commonly used technique, the heavier metal casings and unease in usage for wide applications made them avoidable to some extent. The chemical structure of CL20, RDX and TNT are given in fig. 6.1.
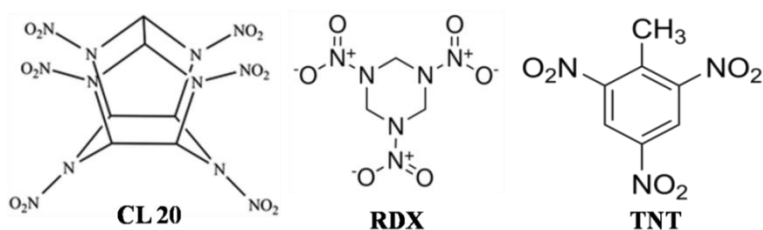

Fig. 6.1 Chemical structure of Nitramine (CL20, RDX) and Nitro Aromatic (TNT) molecules

Therefore, the search for inexpensive, portable and sensitive detectors with ability to detect trace level molecules is still in progress. Optical based methods using infrared or visible light are found to be efficient for explosives detection. Examples include Surface Enhanced Raman Scattering (SERS) a well advanced, non destructive, cost effective and highly sensitive technique for detection of explosives by identifying characteristic vibrational modes [Sultan Ben-Jaber et al. (2016)]. In addition, fluorescence based methods provide best sensitivity because the emission signal is visible and is measured with a low background emission [Yan Geng et al. (2015)].

In general, fluorophores used for explosive sensing are organic and inorganic polymers, crystals and thin films. The electron transfer technique is the main mechanism in the fluorescence quenching based detection and provides ample scope for the detection of chemical composition of the indicator and analyte [Heran Nie et al. (2011)]. Fluorescence based detection techniques are broadly categorized as fluorescence quenching and fluorescence turn-on [30].

Most of the research is focused on fluorescence quenching since the emission signal clearly diminishes in the presence of explosive quencher molecule. The fluorescence turn-on is less explored because of the complexity involved in making a non fluorescent material to a fluorescent indicator only in the presence of explosive molecules. The chemistry involved in the explosive sensing mechanism is still a challenge to be investigated. Some limitations with fluorescence detection techniques include photo bleaching of fluorescent materials, slow response times due to the analyte transport and photo degradation. However, the fluorescent detection is portable and inexpensive which has a lot of scope to be further explored.

The main mechanism involved in fluorescence quenching is the photo induced electron transfer between the excited state of the indicator and the ground state of the explosives compound [Heran Nie et al. (2011)]. Some parameters influence the fluorescence quenching and give insight into the kinetics of the mechanism. Emission intensity (I_o) in the absence of analyte is high, but the intensity in the presence of analyte (I) depends on the concentration of analyte or quencher (Q). Static quenching solely depends on the binding of analyte (K_A) whereas collisional quenching is a function of the intrinsic fluorescence lifetime (τ_o) and the rate of analyte indicator collision (K_Q).

The Stern-Volmer equation is a product of static and collisional quenching [Jiajun Ma et al. (2015)]:

$$I_o/I = (1+K_A[Q])(1+K_q\tau_o[Q]) \qquad\qquad (6.1)$$

Diffusion of analyte molecule takes very long times through dense matrix and therefore sensing performance will be decreased. Thin films (<100 nm) can be used for the same where the reliability and reproducibility are difficult because of the low intensity in fluorescence signal. Therefore, work is focused to prepare micro scale and nanoscale porous materials for explosives detection as the transport rate of the analyte through porous network and the sensitivity of detection can be enhanced [Levitsky et al. (2007)]. Another added advantage of porous structures is that the sensitivity and discrimination of analyte can be engineered by tuning the porous structures accordingly.

Yun-Shan Xue et.al developed novel micro porous tetrakis [(3,5-dicarboxyphenoxy)methyl]methane (H_8L), a rare (4,8)-scu type coordination polymer, $[In_2L][NH_2(CH_3)_2]_2$, $DMF_4(H_2O)_{16}$ for nitro aromatic explosive sensing

[Yun-Shan Xue et al. (2013)]. A facile technique to fabricate fluorescent porous thin film (organic) on poly (methyl methacrylate) optical fiber for high fluorescence quenching for trace level detection of TNT and DNT resulting in highest fluorescence quenching efficiency [Jiajun Ma et al. (2015)]. The enhanced quenching efficiency is due to the well organized pore network which results in sensitive fluorescence quenching. Fluorescent poly (2,7-carbazole) with a 4-[tris-(4-octyl-oxyphenyl)methyl] phenyl is used to detect TNT and DNT which can be used after recycling [Heran Nie et al. (2011)].

Processed fluorescent porous organic-inorganic thin films of silica nanotubes were processed with fluorescent dye for practical sensing applications of nitro explosives [Adem Yildirim et al. (2011)]. Mesoporous ormosil thin films were synthesized from facile template free sol-gel methods for rapid and selective quenching of nitro aromatic molecules: Trinitrotoluene (TNT), Dinitrotoluene (DNT) and Nitrobenzene (NB). The formation of π-π stacking in the thin pyrene doped polyether sulfone worm like structured thin film is developed for naked eye trace level detection of nitro aromatic explosive vapours and are reusable [Pinar Beyazkilic et al. (2014)]. The film showed different quenching performance to TNT, DNT and NB. This factor is explained based on the differences between the vapour pressures of varied analytes. Lourdes Basabe-Desmonts et.al gave a review in detail based on the fluorescent material that can be synthesized using different techniques and their applications for chemical sensing [Lourdes Basabe-Desmonts et al. (2007)]. The growth conditions of conjugated porous polymer (CPP) were optimized in developing sensor for TNT vapour [Jennifer L. Novotney et al. (2013)].

In the present chapter, porous $Zr_{0.8}Sn_{0.2}TiO_4$ were synthesized using gel casting with different pore forming agents like baking soda, ethyl cellulose and starch. The synthesis procedure is explained from schematic as shown in fig. 6.2. The substrates have multi emission peaks with an excitation wavelength of 355 nm. When an analyte of TNT, RDX and CL 20 were in contact with ZST, the fluorescence emission quenched with time as well as with analyte concentration. The quenching efficiency of each analyte with concentration and time are discussed in detail.
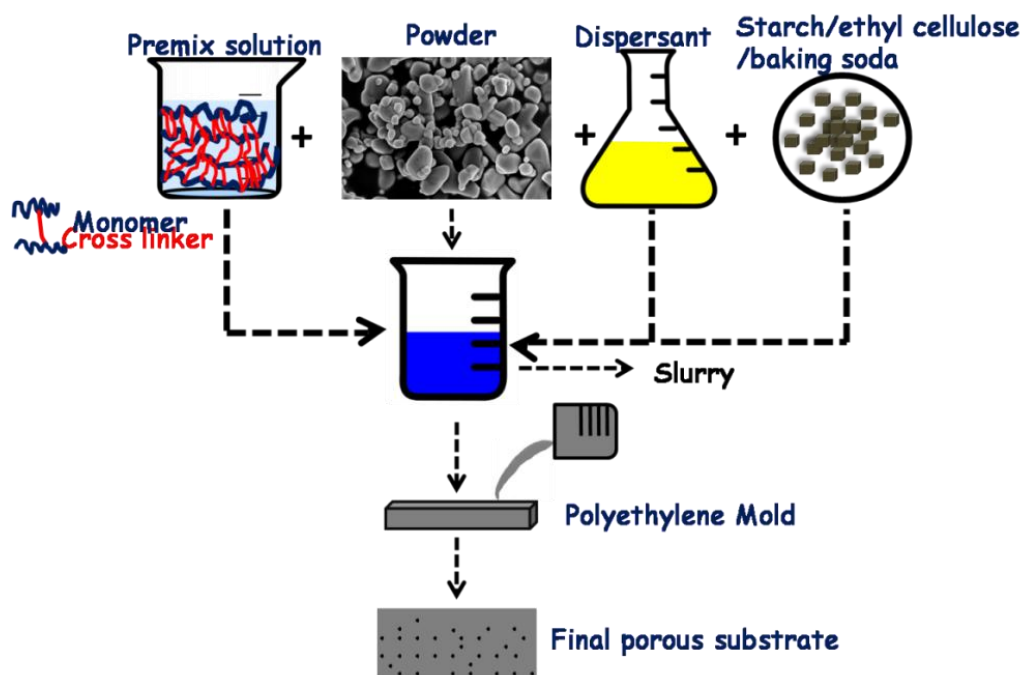

Fig. 6.2 Schematic representation of synthesis of $Zr_{0.8}Sn_{0.2}TiO_4$ porous substrates from gel casting.

6.2 Experimental details

As mentioned in the experimental section of chapter II, $Zr_{0.8}Sn_{0.2}TiO_4$ was prepared using gel casting technique. In order to make porous $Zr_{0.8}Sn_{0.2}TiO_4$,

starch, ethyl cellulose and baking soda were added and the slurry is tumbled for 12 h to get the homogeneous mixing. Six samples of 20 vol.% and 25 vol.% loading with 5 wt.% starch, ethyl cellulose and baking soda were prepared and their X-ray diffractions along with microstructure were recorded. The solids loading and their relative densities were mentioned clearly in table 6.1. Out of all the samples prepared using different pore forming agents, the sample with less density ZST 01 is considered for the study.

Table 6.1: Sample coding and their corresponding solids loading and relative density

Pore forming agent	Sample code	Solids loading (Vol. %)	Relative Density (%)
Starch	ZST 01	20	54
	ZST 02	25	63
Ethyl cellulose	ZST 03	20	59
	ZST 04	25	67
Baking soda	ZST 05	20	66
	ZST 06	25	78

6.3 Microstructure of $Zr_{0.8}Sn_{0.2}TiO_4$ substrates

Fig. 6.3 gives the microstructure of all the samples prepared using gel casting with different pore forming agents. ZST 01 with addition of starch forms the low density and the grain size also found to be low when compared to the samples prepared by adding ethyl cellulose and baking soda. ZST 03 and ZST 04 possess relatively larger grains. It is clear that ZST 05 and ZST 06 have distorted grain structure with lesser porosity. To investigate the fluorescence quenching with different analytes, porous ZST substrates of same density are considered. Conditions are to be further optimized in order to make the micro porous ZST using gel casting for enhanced properties.
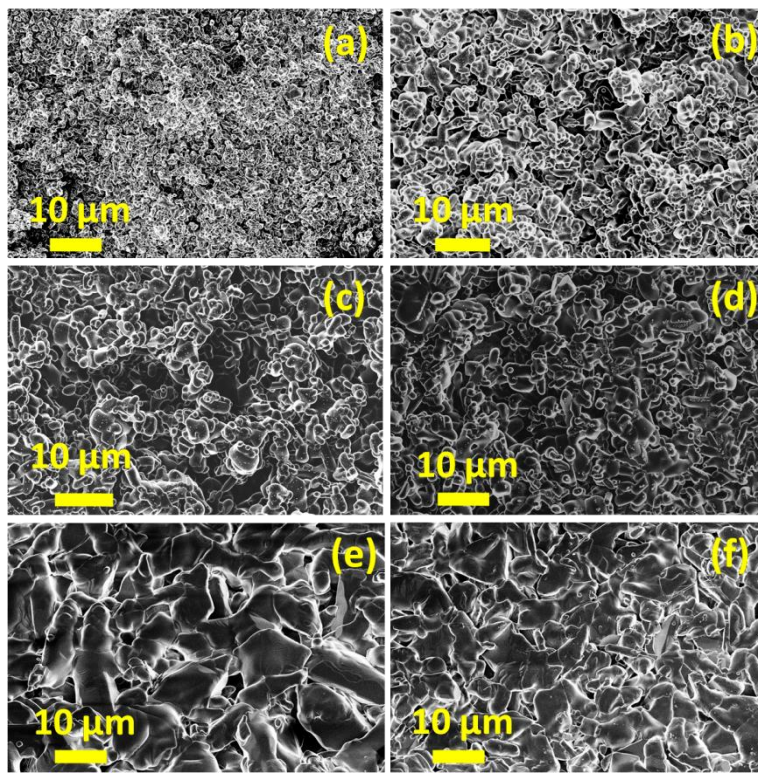
Fig. 6.3 Microstructure of porous ZST with pore forming agents (a) ZST 01, (b) ZST 02 (c) ZST 03 (d) ZST 04 (e) ZST 05 and (f) ZST 06

6.4 Fluorescence quenching measurements

CL20 (Hexanitrohexaazaisowurtzitane), RDX (3,5-trinitroperhydro-1,3,5-triazine) and TNT (2,4,6-trinitrotoluene) are the analytes used in the present study. The analytes of different concentrations are prepared using acetonitrile as solvent. Fluorescence spectra for acetonitrile, CL20, RDX and TNT in acetonitrile are recorded prior to the quenching measurements and are given in fig. 6.4. Porous ZST exhibit multi emission peaks with many defects in the form of unreacted ZrO_2, SnO_2 and TiO_2 and the fluorescence spectra is dominantly categorized into green (561, 567 and 573 nm), orange (598, 603, 612 and 617 nm) and red (651, 659 and 666 nm) emissions as shown in fig. 6.4.
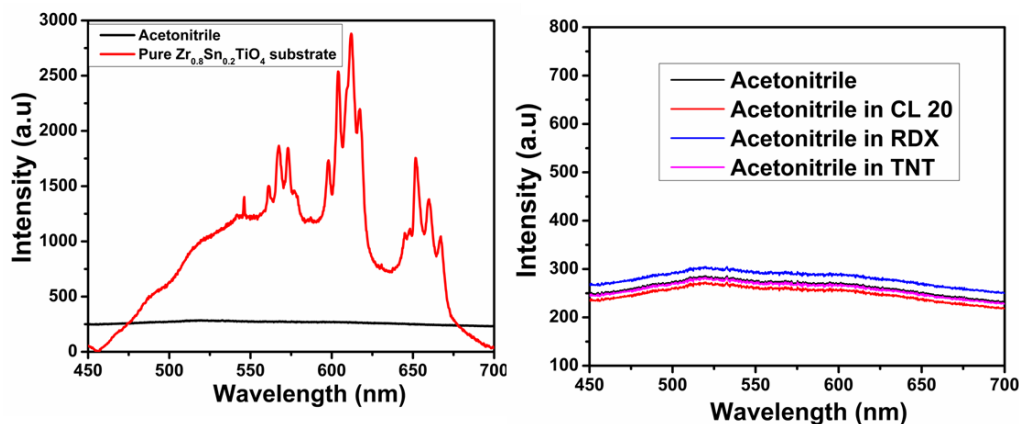
Fig. 6.4 Fluorescence spectra of pure acetonitrile, CL 20, RDX and TNT in acetonitrile

The Nitro Aromatic and Nitramine Compounds (NACs) including TNT, CL20 and RDX can quench the fluorescence emission of porous ZST substrate where the fluorescence intensity decreases gradually with increasing analyte concentration from 1 μM to 1 M as shown in fig. 6.4. These fluorescence quenching spectra are in the order of TNT>CL20>RDX confirming the response of porous ZST substrates differently to different analytes. The stability of the fluorescence quenching of CL 20, RDX and TNT was studied by measuring the emission intensities of porous ZST substrates at different time intervals.
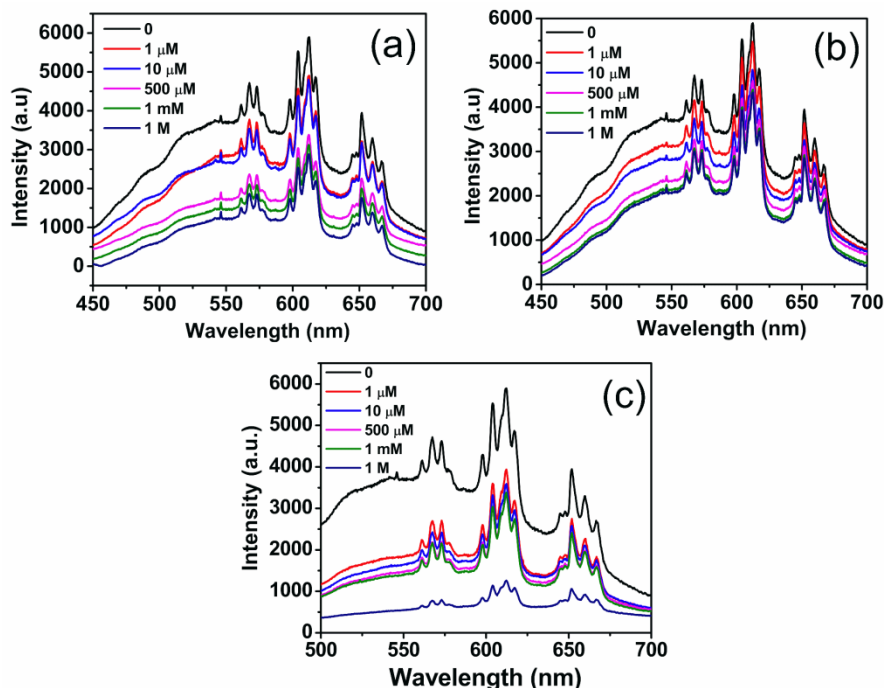
Fig. 6.5 Fluorescence spectra of porous ZST with respect to different concentrations of CL20 analyte

Fluorescence spectra measured at different concentrations with time intervals in case of CL 20 are given in fig. 6.5. Fluorescence spectra were recorded immediately after the ZST substrates is in contact with analyte and considered as 0 s measurement in which the diffusion is not complete. After 10 s, the fluorescence signal started decaying but is not significant in case of 1 μM and 10 μM. There is a remarkable decrease in intensities for the analyte concentration of 500 μM and 1 mM respectively thereby increasing intensity at 1 M. This confirms the minimum density or concentration of analyte molecules required for the maximum quenching in case of CL 20. The remarkable quenching of emission at 500 μM and 1 mM is attributed to the enhanced diffusion of CL 20 into porous ZST thereby promoting photo induced electron transfer between CL 20 and porous ZST.
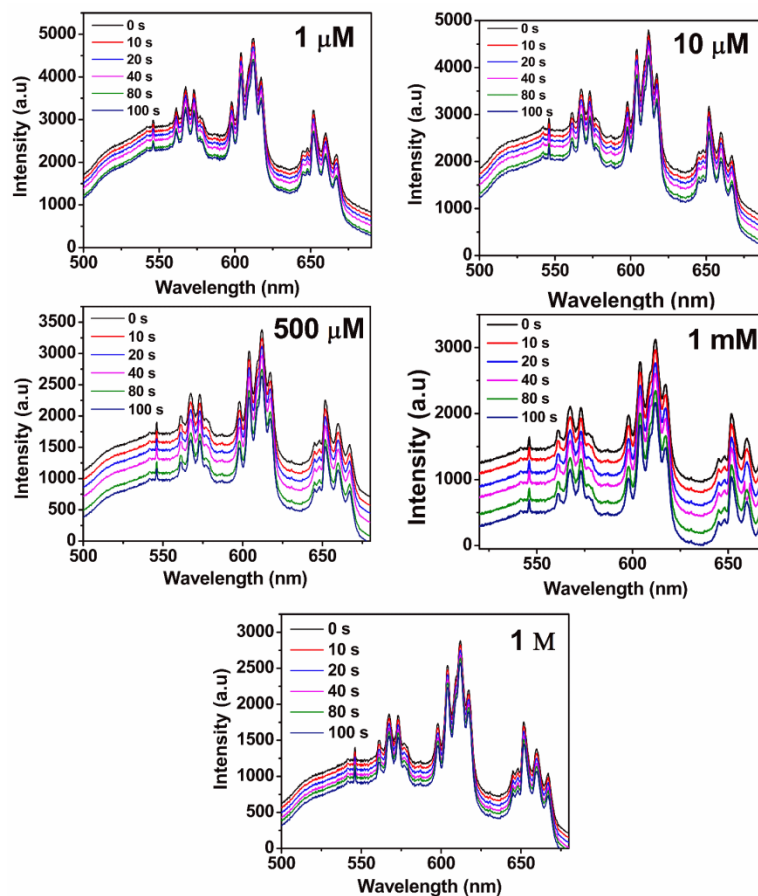
Fig. 6.6 Fluorescence spectra of porous ZST corresponding to different concentrations of CL20 analyte with respect to time

The same experiment is repeated for nitramine RDX. Fluorescence spectra measured at different concentrations with time intervals in case of RDX are given in fig. 6.6. The emission signal starts quenching after 10 s irrespective of all concentrations but the prominent decrease is observed only in case of 500 μM whereas the quenching is almost negligible in case of 1 M. In case of RDX, the emission peaks at 612 nm are found to be slightly broader when compared to CL20.
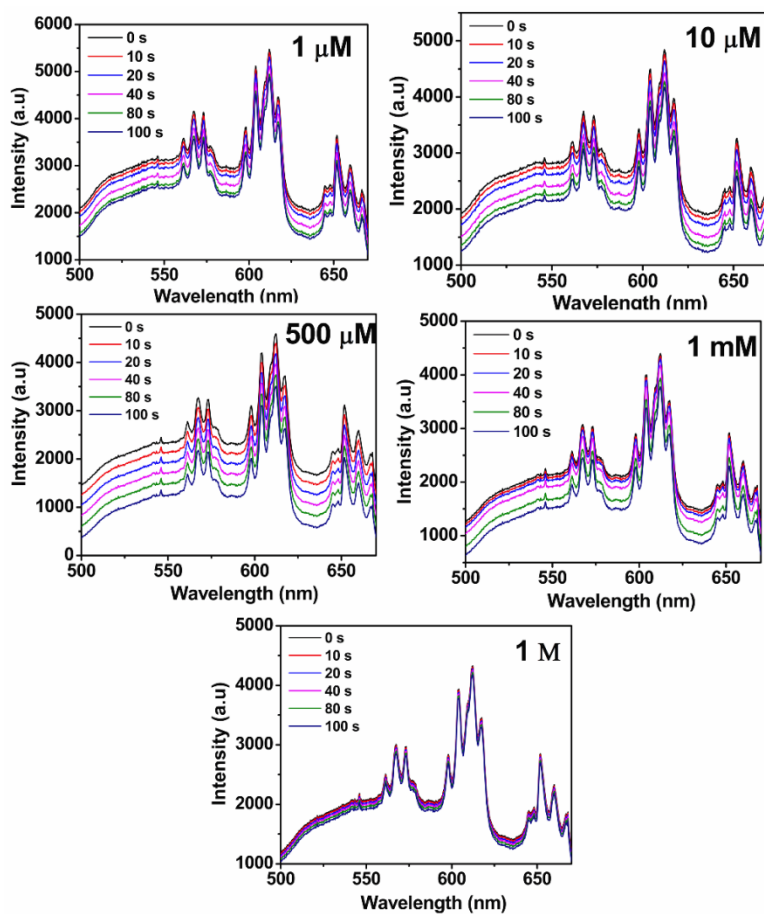
Fig. 6.7 Fluorescence spectra of porous ZST corresponding to different concentrations of
RDX analyte with respect to time

Fig. 6.7 shows the fluorescence quenching of the porous ZST against TNT exposure recorded at different time intervals. Fluorescence of the ZST was quenched significantly from 10 μM to 1 M and with increasing time the intensity of the signal decreases further. This confirms the stability of the porous ZST for fluorescence quenching in case of TNT. The quenching efficiencies of all the analytes were discussed in detail in the next section.
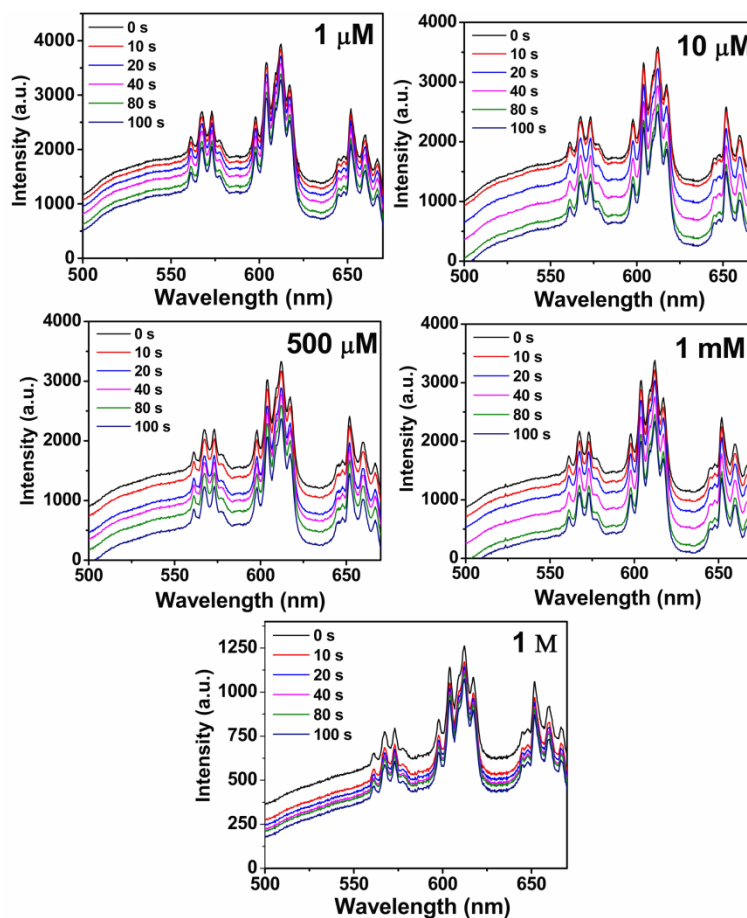
Fig. 6.8 Fluorescence spectra of porous ZST corresponding to different concentrations of TNT analyte with respect to time

The fluorescent variations from different regions (orange, green and red) suggest that the emission at different wavelengths actually responds distinctly to various analytes. Therefore, the plot of the variation in fluorescence intensity (I_o/I)-1, at three selected wavelengths (567 nm, 612 nm and 651 nm) as recognition patterns are shown in fig. 6.8 where I_o and I are the intensities of the porous ZST in the absence and presence of analytes respectively. These three wavelengths were chosen because they represent the maximum in the green (567 nm), orange (612 nm) and red (651 nm) regions. It is clear that the array of three

wavelengths can generate a distinct pattern response to each NAC, suggesting that the present substrate could discriminate the structurally similar analytes.
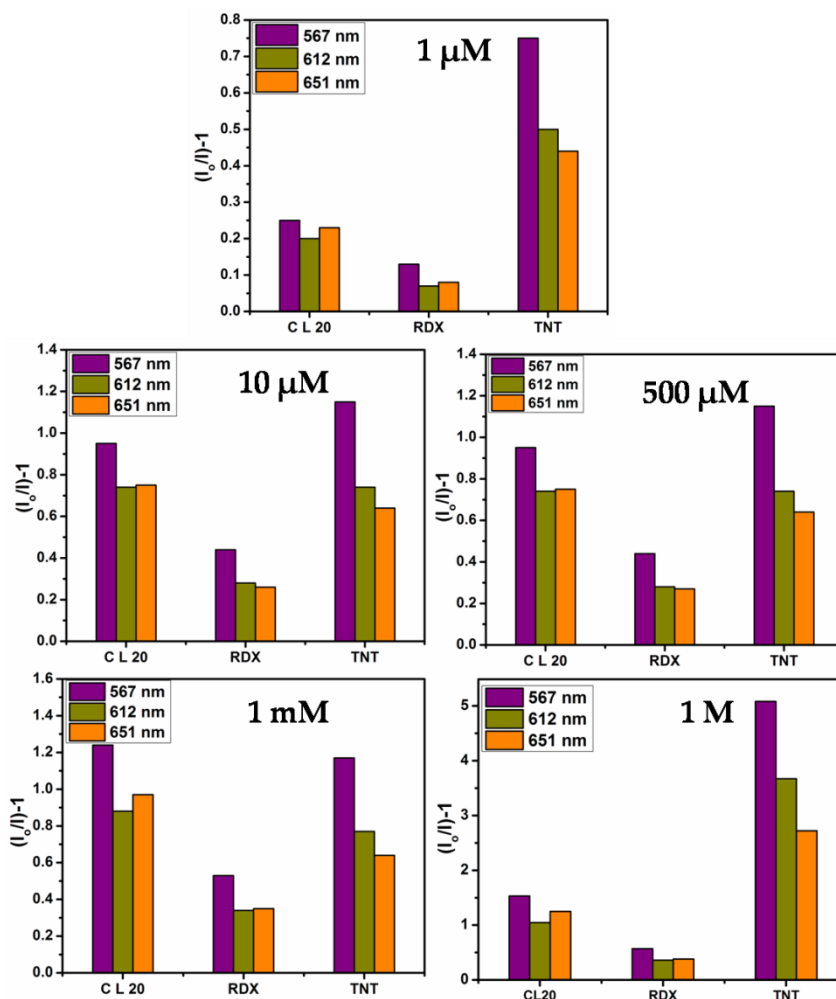

Fig. 6.9 Recognition patterns for CL20, RDX and TNT analytes by collecting fluorescence quenching data at three selected wavelengths

Fluorescence variations from defect centers of porous ZST suggest different emission at different wavelengths and respond differently to different analytes. From all the recognition patterns, TNT is found to be the best analyte for quenching fluorescence signal regardless of concentration and wavelength.

These recognition patterns confirms that array of three wavelengths can generate a fingerprint to differentiate analytes encouraging the use of porous ZST substrates to discriminate the structurally similar explosive molecules.

Quenching efficiency of porous ZST substrate with different analytes is shown in fig. 6.9. The examination of quenching response of porous ZST substrates to different analytes may affect the detection ability of nitro aromatic and nitramine explosive molecules. It is observed that emission is quenched by 30% in case of 1 mM of CL20 while this value 23% and 30% for RDX and TNT for 500 μM and 1 mM respectively. It can be confirmed that porous ZST is more sensitive to both CL20 and TNT when compared to RDX. The quenching performance of porous ZST substrates are following the order of TNT>CL20>RDX.

The quenching efficiency was also further confirmed from Stern-Volmer constants of equation (6.1). The quenching efficiency as revealed by the Stern-Volmer constants follows the order of TNT>CL20>RDX. It is well known that the quenching efficiency solely depends on the electron acceptor ability of Nitro Aromatic and Nitramine analytes promoting the electron transfer from immobilized porous ZST to analytes. Analytes with different chemical structures have different electron acceptor ability which ultimately influences the fluorescence decrease of the porous ZST.

Quenching efficiencies varied for different concentrations with different analytes because of the diffusion of concentrated analytes into the porous ZST. To make it clear, the hydrophilic or hydrophobic nature between analyte and porous ZST substrate is to be understood. The contact angle measurements can

reveal the diffusion of analyte into the porous ZST substrate. Higher the tendency of hydrophilic nature, higher will be the accessibility of porous ZST substrate and analyte thereby enhancing photo induced electron transfer resulting in higher emission quenching.
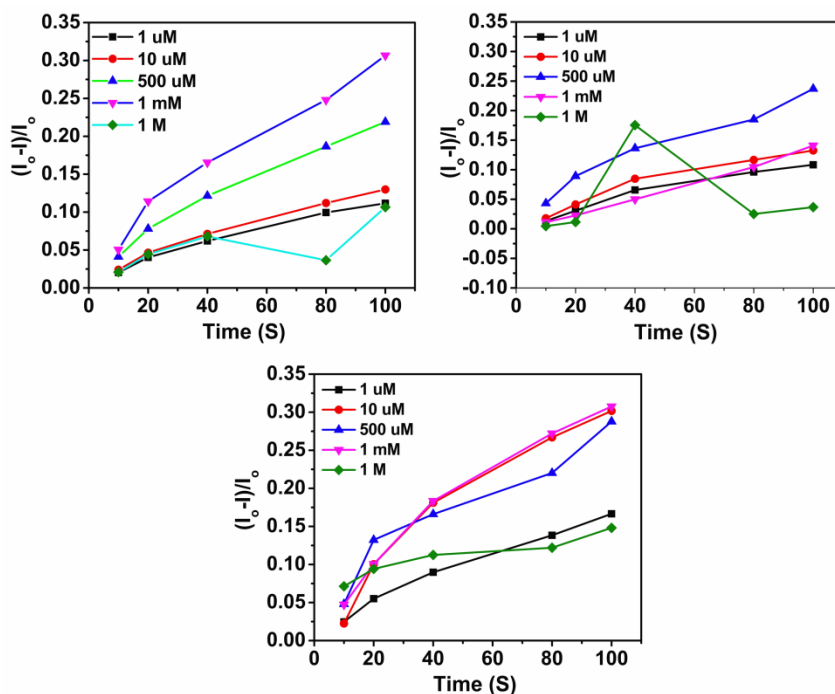

Fig. 6.10 Concentration dependent fluorescence quenching efficiencies at 612 nm for porous ZST substrates with different analytes

The sensitivity of the porous ZST substrate to analyte is determined from Stern-Volmer plot of I_o/I as a function of analyte concentration at 612 nm as shown in fig. 6.10. The obtained plots reveal good agreement with the Stern-Volmer equation as follows

$$I_o/I = 1 + K_{sv}[analyte] \qquad (6.2)$$

The Stern-Volmer constant K_{sv} is calculated from the slope of the Stern-Volmer plots. The K_{sv} values of CL20, RDX and TNT are 2.82×10^2, 1.31×10^2 and 2.9×10^2 M^{-1} respectively. These values reflect the sensitivity of porous ZST substrate to analytes and are in the order of TNT>CL20>RDX. The repeatability of the porous ZST substrate was investigated and the fluorescence intensity is recorded with 5 min time interval after substrate displayed the complete quenching. But, for the second time the results are not encouraging as in the case of first time. This shows that the preparation method of porous ZST substrate is to be further optimized towards sensing for analytes.
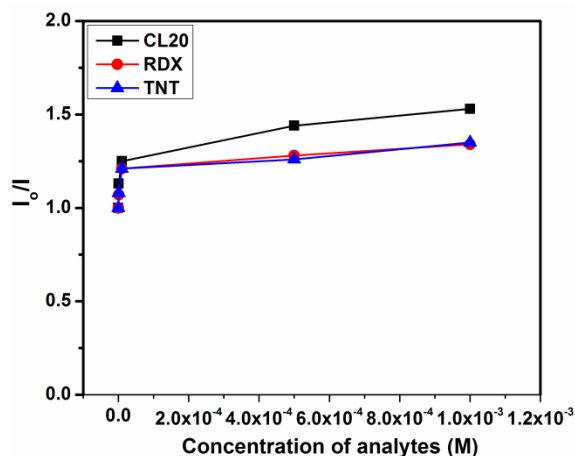

Fig. 6.11 Stern-Volmer plots of the fluorescence quenching of porous ZST to the concentration of analytes

In conclusion, a porous ZST substrate via gel casting is prepared. The diffusion of analyte with various concentrations into the porous ZST substrate was verified by fluorescence quenching technique. Pure ZST substrate exhibits fluorescence due to the defect centers from unreacted ZrO_2, SnO_2 and TiO_2 and emission spectra is broadly categorized into green, orange and red regions. These emission signals were quenched down when the porous ZST substrate is in

contact with different nitro aromatic and nitramine analytes of different concentrations.

To further confirm the stability of the fluorescence quenching, the emission spectra is recorded after regular time intervals (0s, 10s, 20s, 40s, 80s and 100s) keeping the analyte concentration constant. Each analyte at a particular concentration gave the best fluorescence quenching at three selected wavelengths (567 nm, 612 nm and 651 nm) provided a recognition pattern for each analyte (CL20, RDX and TNT). The porous ZST substrate also displays sensitivity towards different analytes confirmed from the Stern-Volmer plots. The repeatability of the porous ZST substrates towards the same analyte is verified but is not satisfactorily and cannot be readily used for the practical applications.

To the best of our knowledge, the studies on using porous ceramic substrate for explosive sensing have not been done. But, this study presents a novel strategy of developing discriminatory materials by using multiple emission of a single porous ZST. The present study will give an insight into the usage of identifying structurally similar chemicals using porous ZST. More studies have to be done to understand and analyze the mechanism of multi emission and their quenching for different analyte molecules.

Chapter 7

Conclusions and Scope for future work

In this chapter, the main conclusions of the present thesis are summarized. Some possibilities for extending this work in the future are also discussed. Broadly the thesis work is classified in to two applications:

1. Polycrystalline and oriented $LiNbO_3$ (LN) thin films for nonlinear and optoelectronic applications.

2. Porous $Zr_{0.8}Sn_{0.2}TiO_4$ (ZST) substrates for explosive sensing using fluorescence quenching.

In the first part, $LiNbO_3$ thin films were deposited by means of Al:ZnO as intermediate layer using pulsed laser deposition. The films obtained are interestingly (110) and (300) oriented which has not been reported previously. Many reports on $LiNbO_3$ thin films are either polycrystalline or C-axis epitaxial so far. The films evidenced transparency of above 80% in visible and near IR region. The polycrystalline and $LiNbO_3$ oriented in (300) direction demonstrate reverse saturable absorption and transits to saturable absorption in case of (110) $LiNbO_3$. The switching behavior of nonlinear absorption based on structural differences can be directly used in nonlinear optical devices. In addition, nonlinear optical properties derived from open aperture and closed aperture curves of Z-Scan provides detailed insight into the quantitative information about nonlinear absorption coefficient, nonlinear refractive index and nonlinear susceptibility. The observed two photon absorption is attributed to the indirect transition via intermediate defect levels which relates to the structural un-

symmetry and significant change in band gap also contributes to the nonlinearity in $LiNbO_3$ thin films. The large nonlinearity in refractive index is the result of electronic polarization and ferroelectric polarization. The third order nonlinearity of polycrystalline LN and (300) oriented LN are of the order of 10^{-9} esu and (110) oriented LN is of the order of 10^{-15} esu which is observed to be greater than the single crystal Z-cut $LiNbO_3$.

Temperature dependent linear optical properties of the same films (polycrystalline, (110) and (300) oriented $LiNbO_3$) were extracted from transmission spectra. The optical constants like refractive index, extinction coefficient and optical band gap are derived in the temperature range of 308 to 523 K. The transmission got decreased with increase in temperature. The band gap is found to be red shifted with increasing temperature and is attributed to the band gap renormalization. Positive thermo optic coefficient (dn/dT) is observed for all the films and is attributed to the structural dissimilarities. These results could lead to the usage of $LiNbO_3$ thin film based photonic devices in optoelectronic and integrated optic applications at different temperatures.

In the second part, conditions were optimized for the synthesis of $(Zr_{0.8}Sn_{0.2})TiO_4$ ceramics. This is done using a slurry based technique (gel casting) involving organic/inorganic carrier medium. Reports on usage of $(Zr_{0.8}Sn_{0.2})TiO_4$ ceramics for dielectric resonators and their microwave dielectric properties are explained. An inexpensive polyethylene mould is used for the fabrication of dielectric resonators. From gel casting, $(Zr_{0.8}Sn_{0.2})TiO_4$ ceramics are processed without any additives and were sintered at 1400 °C. The desirable microwave dielectric properties of $\epsilon_r = 37$, Qxf=32000 and $\tau_f = +6$ ppm/°C, which is comparable with the dielectric resonators of this composition prepared by the ceramic route are

obtained. The advantages like inexpensive, desired thicknesses for ease in fabrication of complex shapes and adaptability to industrial applications made this work quite attractive.

The slurry based technique is considered as a fundamental idea to synthesize porous substrates of $(Zr_{0.8}Sn_{0.2})$ TiO_4 for the fluorescence quenching based explosive sensing applications. Details of porous $Zr_{0.8}Sn_{0.2}TiO_4$ made using gel casting with different pore forming agents like baking soda, ethyl cellulose and starch are discussed. The substrates have multiple emission peaks in green, orange and red regions with an excitation wavelength of 355 nm. When an analyte of TNT, RDX and CL20 were in contact with ZST, the fluorescence emission quenched with time as well as with analyte concentration. Analyte diffusion through porous matrix and the sensing performances are studied. The main mechanism involved in fluorescence quenching is the photo induced electron transfer between the excited state of the indicator and the ground state of the analyte.

The quenching efficiencies varied to CL20, TNT and RDX. The fluorescence quenching efficiencies are in the order of TNT>CL20>RDX confirming the response of porous ZST substrates differently to different analytes. It is observed that emission of ZST is quenched by 30% in case of 1 mM for CL20 while it is 23% and 30% for RDX and TNT for 500 μM and 1 mM respectively. The materials developed in this work have extensive potential in sensing applications due to the ease in fabrication, high mechanical strength and tunability in porous structures as well as reusability by removing the analytes at high temperatures by heating since the substrates are ceramics. The porous ZST substrate also displays sensitivity towards different analytes confirmed from the Stern-Volmer

plots. The repeatability of the porous ZST substrates towards the same analyte is verified but is not satisfactorily and cannot be readily used for the practical applications.

The studies on application of porous ceramic substrates for explosive sensing have not been reported so far. But, this study presents a new strategy of developing discriminatory materials by using multiple emissions from a single porous ZST. More studies have to be done to understand and analyze the mechanism of multi emission and their quenching for different analyte molecules.

The most important contributions of the thesis are

1. Detailed understanding of the $LiNbO_3$ thin films with Al:ZnO as intermediate layer using pulsed laser and their linear and nonlinear optical properties.

2. Demonstration of the temperature dependent optical constants of $LiNbO_3$ thin films and their usage in optoelectronic applications.

3. Fabrication of $Zr_{0.8}Sn_{0.2}TiO_4$ ceramics using gel casting and their microwave dielectric properties were explored.

4. Porous $Zr_{0.8}Sn_{0.2}TiO_4$ substrates exhibit dominant green and red emission which quenches with different analyte concentrations. The quenching efficiency is found to be good enough to use these porous substrates for nitro explosive sensing.

Future Scope:

1. Deposition of high quality $LiNbO_3$ thin films and their electro optic modulator studies at microwave frequency.

2. Piezoelectric properties of high quality $LiNbO_3$ thin films can be explored.

3. Studies on ZnO/LiNbO$_3$/ZnO staked layers for optical wave guiding applications.

4. Temperature dependent transmission of LiNbO$_3$ is of interest for optical switching applications.

5. Homogeneously ordered porosity in Zr$_{0.8}$Sn$_{0.2}$TiO$_4$ using gel casting can be used for microwave filter and sensor applications.

6. Studies on doping trivalent and pentavalent impurities into (Zr$_{0.8}$Sn$_{0.2}$)TiO$_4$ will greatly enhance the microwave dielectric properties and can be used for device applications.

References

Abliz Yimit, Axel G. Rossberg, Takashi Amemiya, Kiminori Itoh, Talanta, 65, 1102 (2005)

Adem Yildirim, Handan Acar, Turan S. Erkal, Mehmet Bayindir, Mustafa O. Guler, ACS Appl. Mater. Interfaces, 3, 4159 (2011)

Ahmed A. Kishk, Yan Yin, Glisson A.W., IEEE TRANSACTIONS ON ANTENNAS AND PROPAGATION, 50, 469 (2002)

Akazawa H., Shimada, M., Materials Science and Engineering: B, 120, 50 (2005)

Allwood D.A., Klipstein P.C., Mason N.J., Nicholas R.J., Walker P.J., Journal of Electronic Materials, 29, 99 (2000)

Anil Tumuluri, James Raju K.C., Adv. Mat. Lett., 5, 287 (2014)

Anil Tumuluri, James Raju K.C., Ceramics International, 40, 3371 (2014)

Anil Tumuluri, K Lakshun Naidu, James Raju K.C., International Journal of Chem. Tech. Research, 6, 3353 (2014)

Anil Tumuluri, P Missak Swarup Raju, KC James Raju, V Seshubai, T Rajasekharan, Materials Letters, 154, 128 (2016)

Anil Tumuluri, Mounika Rapolu, Venugopal Rao S., James Raju K.C., AIP Conf. Proc. 1728, 020365 (2016)

Anusha P.T., Thomas A.R., Philip R., Venugopal Rao S., Chemical Physics Letters, 641, 23 (2015)

Ashish Kumar, Parmod Kumar, Kaushal Kumar, Trilok Singh, Singh R., Asokan K., Kanjilal D., Journal of Alloys and Compounds, 649, 1205 (2015)

Ashok Kumar Jyani, Seema Awasthi, Animesh Biswas, Applied Electromagnetics Conference (AEMC), 2013 IEEE, 1 (2013)

Ausrine Bartasyte, Valentina Plausinaitiene, Adulfas Abrutis, Sandra Stanionyte, Samuel Margueron, Pascal Boulet, T Kobata, Yoshiaki Uesu, Jerome Gleize, Journal of Physics: Condensed Matter, 25, 205901 (2013)

Aziz M.J., Appl. Phys. A, 93, 579 (2008)

Bai, M., Huang, S., Xu, S., Hu, G. and Wang, L., Analytical chemistry, 87, 2383 (2015)

Bartasyte, A., Plausinaitiene, V., Abrutis, A., Murauskas, T., Boulet, P., Margueron, S., Gleize, J., Robert, S., Kubilius, V. and Saltyte, Z., Appl. Phys. Lett., 101, 122902 (2012)

Basanth S. Kalanoor, Laxman Gouda, Ronen Gottesman, Shay Tirosh, Eynav Haltzi, Arie Zaban, Yaakov R. Tischler, ACS Photonics, 3, 361 (2016)

Bashaiah Sindam, James Raju K.C., Journal of Materials Science: Materials in Electronics, 26, 3997 (2015)

Basun, S.A., Bursian, V.E., Evans, D.R., Kaplyanskii, A.A., Razdobarin, A.G. and Sochava, L.S., Physical review letters, 100, 057602 (2008)

Beyazkilic, P., Yildirim, A. and Bayindir, M., ACS applied materials & interfaces, 6, 4997 (2014)

Bo Xiao, Sangram K. Pradhan, Kevin C. Santiago, Gugu N. Rutherford, Aswini K. Pradhan, Scientific Reports, 6, 24385 (2016)

Bornand, V., Huet, I., Bardeau, J.F., Chateigner, D. and Papet, P., Integrated Ferroelectrics, 43, 51 (2002)

Brian D. Viezbicke, Shane Patel, Benjamin E. Davis, Dunbar P. Birnie, Physica Status solidi b, 252, 1700 (2015)

Bukhari, S., Islam, M., Haziot, A. and Beamish, J., Journal of Physics: Conference Series, 568, 032004 (2014)

Cai L, Kong R, Wang Y, Hu H, Opt Express, 23, 29211 (2015)

Cajzl, J., Nekvindová, P., Macková, A., Malinský, P., Oswald, J., Staněk, S., Vytykáčová, S. and Špirková, J., Optical Materials, 53, 160 (2016)

Campos, B.B., Contreras-Cáceres, R., Bandosz, T.J., Jiménez-Jiménez, J., Rodríguez-Castellón, E., da Silva, J.C.E. and Algarra, M., Carbon,106, 171 (2016)

Chen N.B., Wu H.Z., Qiu D.J., Xu T.N., Chen J., Shen W.Z., J. Phys.: Condens. Matter 16, 2973 (2004)

Chen, R., Sun, G., Xu, G., Ding, Y.J. and Zotova, I.B., Applied Physics Letters, 101, 111101 (2012)

Chen, Z., Huang, J., Yang, Y., Wang, Y., Wu, Y., He, H., Wei, X., Ye, Z., Zeng, H., Cong, H. and Jiang, Z., RSC Advances, 2, 7380 (2012)

Christen H.M., Eres G., Journal of Physics: Condensed Matter, Volume 20, 264005 (2008)

Christoph Brandes, Laura Treccani, Stephen Kroll, Kurosch Rezwan, Journal of American Ceramic Society, 97, 1393 (2014)

Costas P. Grigoropoulos "Transport in Laser Microfabrication: Fundamentals and applications", Cambridge University Press, ISBN-978 0 521 821728 (2009)

Das B.K., Ricken R., Sohler W., Appl. Phys. Lett. 82, 1515 (2003)

Demirel, G.B., Daglar, B. and Bayindir, M., Chemical Communications, 49, 6140 (2013)

Di Zhou, Li-Xia Pang, Ze-Ming Qi, Baio-Bing Jin, Xi Yao. Sci Rep., 4, 5980 (2014)

Di Zhou, Wen-Bo Li, Jing Guo, Li-Xia Pang, Ze-Ming Qi, Tao Shao, Hui-Dong Xie, Zhen-Xing Yue, Xi Yao, Inorganic Chemistry, 53, 5712 (2014)

Di, Z., Li-Xia, P., Ze-Ming, Q., Biao-Bing, J. and Xi, Y., Scientific reports, 4 (2014)

Díaz-Moreno, C., Farias, R., Hurtado-Macias, A., Elizalde-Galindo, J. and Hernandez-Paz, J., Journal of Applied Physics, 111, 07D907 (2012)

Dipali Soren, Rowdra Ghatak, Rabindra K. Mishra, and Dipak R. Poddar, Progress In Electromagnetics Research B, 60, 195 (2014)

Donald M. Mattox "Handbook of Physical Vapor Deposition Processing ", Noyes publications, U.S.A, ISBN-0-8155-1422-0 (1998)

DrDomenico M., S. H. Wemple, J. Appl. Phys. 40, 720 (1969)

Fan Zhang, Rong-Jun Zhang, Dong-Xu Zhang, Zi-Yi Wang, Ji-Ping Xu , Yu-Xiang Zheng, Liang-Yao Chen, Ren-Zhong Huang, Yan Sun3, Xin Chen, Xiang-Jian Meng, Ning Dai, Applied Physics Express 6 121101 (2013)

Farid A. Harraz, Sensors and Actuators B: Chemical, 202, 897 (2014)

Fernández-Ruiz R., Martín y Marero D., Bermúdez V., PHYSICAL REVIEW B 72, 184108 (2005)

Freer, R., Azough F., Journal of the European Ceramic Society, 28, 1433 (2008)

Freitas G.F.G., Nasar R.S., Cerqueira M., Melo D.M.A., Longo E., Varela J.A., Materials Science and Engineering A, 434, 19 (2006)

Fryad. Z. Henari, Karl Cazzini, Fathi El Akkari, Werner J. Blau, J. Appl. Phys. 78, 1373 (1995)

Fukuda, T. and Hirano, H., Applied Physics Letters, 28, 575 (1976)

G. Balestrino, S. Martellucci, P. G. Medaglia, A. Paoletti, G. Petrocelli, A. Tebano, A. Tucciarone, F. Gelli, Giorgetti E., Sottini S., Tapfer L., Appl. Phys. Lett., 78, 1204 (2001)

Gallo, K., Codemard, C., Gawith, C.B., Nilsson, J., Smith, P.G., Broderick, N.G. and Richardson, D.J., Optics letters, 31, 1232 (2006)

Gallo, K., Codemard, C., Gawith, C.B., Nilsson, J., Smith, P.G., Broderick, N.G. and Richardson, D.J., Optics letters, 3, 1232 (2006)

Gallo, K., Pasquazi, A., Stivala, S. and Assanto, G., Physical review letters, 100, 053901 (2008)

Gan Q, Ding YJ, Bartoli FJ., Phys Rev Lett. 102, 056801 (2009)

Ghasemi A., Ashrafizadeh A., ShamsAlam R., J.PhysD:Conf.Ser., 191, 012016 (2009)

Gilissen R., Erauw J.P., Smolders A., Vanswijgenhoven E., Luyten J., Materials and Design, 21, 251 (2000)

Gokcen Birlik Demirel, Bihter Daglarac and Mehmet Bayindir, Chem. Commun., 49, 6140 (2013)

Gorachand Ghosh, OPTICS LETTERS, 19, 1391 (1994)

Guo Jing, Zhou Di, Wang Lu, Wong Hong, Shao Tao, Qi Ze M, et al. Dalton Trans., 42, 1483 (2013)

Guo X., Zheng H., King S.W., Afanasev V.V., Baklanov M.R., de Marneffe M.F., Nishi Y., J. L. Shohet, Appl. Phys. Lett., 107, 082903 (2015)

Gupta, V., Tomar, M., Bhattacharya, P., Sreenivas, K. and Katiyar, R.S., Ferroelectric Letters, 32, 125 (2005)

Hammel E.C., Ighodaro O.L.R., Okol O.I., Ceramics International, 40, 15351 (2014)

Hana Woo, Somin Cho, Yejee Han, Weon-Sik Chae, Dae-Ro Ahn, Youngmin You, Wonwoo Nam, J. Am. Chem. Soc., 135, 4771 (2013)

Hansen, P.J., Terao, Y., Wu, Y., York, R.A., Mishra, U.K. and Speck, J.S., Journal of Vacuum Science & Technology B, 23, pp.162-167 (2005)

Haung Cheng-Ling, Weng Min-Hung, Chen Hui-Liang. Jpn. J. Appl. Phys., 40, 698 (2000)

He, R., Zhang R., Zhu X., Wei K., Qu Z., Pei Y., Fang D., Journal of the American Ceramic Society, 97, 2401 (2014)

He, R., Zhang, X., Han, W., Hu, P. and Hong, C., Materials & Design, 47, pp.35-40 (2013)

Heran Nie, Yang Zhao, Ming Zhang, Yuguang Ma, Martin Baumgarten, Klaus Mullen, Chem. Comm., 47, 1234 (2011)

Hirotoshi Nagata, Yasuyuki Miyama, Kaoru Higuma, Yoshihiro Hashimoto, Futoshi Yamamoto, Yuuji Yamane, Miki Yatsuki, MRS Proceedings, 654 (2000)

Hongxia Li, Joris Lousteau, William N. MacPherson , Xin Jiang, Henry T. Bookey, James S. Barton, Animesh Jha, Ajoy K. Kar, OPTICS EXPRESS, 15, 8857 (2007)

Hou Z., Du H., Liu J., Hao R., Dong X., Liu M., Journal of the European Ceramic Society, 33, 717 (2013)

Hou Z., Liu J., Du H., Xu H., Guo A., Wang, M., Ceramics International, 39, 969 (2013)

Hu Z.G., Li Y.W., Yue F.Y., Zhu Z.Q., Chu J.H., Appl. Phys. Lett. 91, 221903 (2007)

Huang C.L., Weng M.H., Mater.Res.Bulletin, 35, 1881 (2001)

Hussain Ali Badran, Results in Physics, 4, 69 (2014)

Ioachim A, Toascan MI, Banciu MG, J. Optoelectron. Adv. Mater. 5, 1395 (2003)

Ioachim, M.G.Bansiu, L.Nedelcu, C.A.Dutu, J. Optoelectronics and Adv. Mater., 8, 3, 941 (2006)

Irzhak, D., Roshchupkin, D. and Punegov, D., Ferroelectrics, 351, 163 (2007)

Janney M.A., Nunn S.D., Walls C.A., Omatete O.O., Ogle R.B., Kirby G.H., McMillan A.D., "The handbook of ceramic engineering", pg. 1-15, Marcel Dekker (1998)

Jennifer L. Novotney and William R. Dichtel, ACS Macro Lett., 2, 423 (2013)

Jiajun Ma, Ling Lv, Gang Zou, Qijin Zhang, ACS Appl. Mater. Interfaces, 7, 241 (2015)

Jian Zhang, Ruzhong Zuo, J. Am. Ceram. Soc., 1, 7 (2016)

Jiang, J., Meng, X.J., Geng, D.Q. and Jiang, A.Q., J. Appl. Phys., 117, 104101 (2015)

Jiang, X., Fang, L., Xiang, H., Guo, H., Li, J. and Li, C., Ceramics International, 41, 13878 (2015)

Jing Guo, Di Zhou, Lu Wang, Hong Wang, Tao Shao, Ze M. Qi, Xi Yao, Dalton Trans., 42, 1483 (2013)

Jinlong Yang, , Juanli Yu , Yong Huang, J. Eur. Cer. Soc. 31, 2569 (2011)

John A. Rogers, Alex A. Maznev and Matthew J. Banet, Keith A. Nelson, Annual Review of Materials Science, 30, 117 (2000)

Kao M.C., Chen H.Z., Yang S.L., Chen Y.C., Hsieh P.T., Yu C.C., Thin Solid Films, 516, 5518 (2008)

Kawamata, A., Hosaka, H. and Morita, T., Sensors and Actuators A: Physical, 135, 782 (2007)

Kilburger, S., Millon, E., Di Bin, P., Boulle, A., Guinebretière, R. and Di Bin, C., Thin Solid Films, 518, 4654 (2010)

Kiselev, D.A., Zhukov, R.N., Bykov, A.S., Malinkovich, M.D. and Parkhomenko, Y.N., PIERS Proceedings, 520 (2014)

Kostritskii S.M., Aillerie M., J. Appl. Phys., 111, 103504 (2012)

Krishna G Podagtlapalli, Syed Hamad, Surya P. Tewari, Sreedhar S., Muvva D. Prasad, Venugopal Rao S., J. Appl. Phys. 113 , 073106 (2013)

Kugsun Hong, Hyukjoon Yoon, Sooncheun Byun, Seoyong Cho, Dongwan Kim, Taeguen Kim, Deukyang Kim, Jongwoon Moon, Hyojong Lee, Byungkyu Kim, , U.S.Patent No.6,242,375 B1 (2001)

Ledbetter H., Ogi, H. and Nakamura N., Mechanics of materials, 36, 941 (2004)

Levitsky I.A., Euler W.B., Tokranova N., Rose A., Appl. Phys. Lett. 90, 041904 (2007)

Li S., Zhong X.L., Cheng G.H., Liu X., Wang J.B., Huang J., Song H.J., Tan C.B., Li B., Zhou Y.C., Appl. Phys. Lett., 105, 192901 (2014)

Li D., Zhang Y., Fan Z. and Yu J., Chemical Communications, 51,13830 (2015)

Li W.B., Xi H.H. and Zhou D., Ceramics International, 41,9063 (2015)

Li-ping Wang, Pei-de Han, Zhu-xia Zhang, Cai-li Zhang, Bing-she Xu, Computational Material Science, 77, 281 (2013)

Liu S.W., Min Xiao, Appl. Phys. Lett., 88, 143512 (2006)

Liu, B., Liu, X.Q. and Chen, X.M., Journal of Materials Chemistry C, 4, 1720 (2016)

Long fang Zou, Christophe Fumeaux, IEEE ANTENNAS AND WIRELESS PROPAGATION LETTERS, 10, 742 (2011)

Lourdes Basabe-Desmonts, David N. Reinhoudt and Mercedes Crego-Calama, Chemical Society Reviews, 36, 993 (2007)

Lü, Z., Zhao, K., Liu, H., Zhou, N., Zhao, H., Gao, L., Zhao, S. and Wang, A., Chinese Optics Letters, 7, 718 (2009)

Ma, H., He, C., Li, X., Ablikim, O., Zhang, S. and Zhang, M., Sensors and Actuators B: Chemical, 230, 746 (2016)

Mackwitz P., Rüsing M., Berth G., Widhalm A., Müller K., Zrenner A., Appl. Phys. Lett. 108, 152902 (2016)

Mailadil Sebastian "Dielectric materials for wireless communication" 1st ed., Netherlands: Elsevier (2008)

Makram A.F., Alwazni M.S., Yarub A.D., Salim E.T., Uda H., Woei C.C., International Journal of Chemical, Molecular, nuclear, materials and metallurgical Engineering, 10, 426 (2016)

Makram, A.F., Alwazni, M.S., Yarub, A.D., Salim, E.T., Uda, H. and Woei, C.C., 2016. World Academy of Science, Engineering and Technology, International

Journal of Chemical, Molecular, Nuclear, Materials and Metallurgical Engineering, 10(5), pp.426-431.

Maksym V. Kovalenko , Wolfgang Heiss , Elena V. Shevchenko , Jong-Soo Lee, Harald Schwinghammer , Paul Alivisatos A. , Dmitri V. Talapin, J. Am. Chem. Soc., , 129, 11354 (2007)

Manoj K. Gupta, Nidhi Sinha, Binay Kumar, J. Appl. Phys. 112, 014303 (2012)

Marc D. Fontana, Patrice Bourson, Appl. Phys. Rev., 2, 040602 (2015)

Marco Bazzan, Cinzia Sada, Appl. Phys. Rev. 2, 040603 (2015)

Mark J. Miller, Junlan Wang, Vacuum, 120, 155 (2015)

Martin F. Volk, Sergiy Suntsov, Christian E. Rüter, Detlef Kip, OPTICS EXPRESS, 2, 1386 (2016)

Meaghan E. Germain, Michael J. Knapp, Chem. Soc. Rev., 38, 2543 (2009)

Michael N. R. Ashfold, Frederik Claeyssens, Gareth M. Fuge and Simon J. Henley, Chem. Soc. Rev., 33, 23 (2004)

Michiura N., Tatekawa T., Higuchi Y., Tamura H., J. Am. Ceram. Soc. 78, 3 (1995)

Mirco Imlau, Holger Badorreck, Christoph Merschjann, Appl. Phys. Rev. 2, 040606 (2015)

Namitha, L.K. and Sebastian, M.T., Materials Research Bulletin, 48, 4911 (2013)

Narottam P. Bansal, Aldo R. Boccaccini, "Ceramics and Composites processing methods", Wiley, ISBN-978-0-470-55344-2 (2012)

Nashimoto, K. and Cima, M.J., Materials Letters, 10, 348 (1997)

Nechache R., Harnagea C., Li S., Cardenas L., Huang W., Chakrabartty J., Rosei F., Nature Photonics 9, 61 (2015)

Nedelcu L., Toacsan M.I., Banciu M.G., Ioachim A., Journal of Alloys and Compounds 509, 477 (2011)

Neelakantan, U.A., Kalathil, S.E. and Ratheesh, R., European Journal of Inorganic Chemistry, 2015, 305 (2015)

Nie, H., Zhao, Y., Zhang, M., Ma, Y., Baumgarten, M. and Müllen, K., Chemical Communications, 47, 1234 (2011)

Norbert Kaiser, Applied Optics, 41, 3053 (2002)

Novotney, J.L. and Dichtel, W.R., ACS Macro Letters, 2, 423 (2013)

Ogbemi O. Omatete, Mark A. Janney, Stephen D. Nunn, Journal of the European Ceramic Society, 17, 407 (1997)

Olhero S.M., Ajay Kaushal, Ferreira J.M.F., RSC Adv., 4, 48734 (2014)

Olivares, J., Crespillo, M.L., Caballero-Calero, O., Ynsa, M.D., García-Cabañes, A., Toulemonde, M., Trautmann, C. and Agulló-López, F., Optics express, 17,24175 (2009)

Olivares, J., Crespillo, M.L., Caballero-Calero, O., Ynsa, M.D., García-Cabañes, A., Toulemonde, M., Trautmann, C. and Agulló-López, F., Optics express, 17, 24175 (2009)

Pai Chun Wei, Surojit Chattopadhyay, Fang-Sheng Lin, Chih-Ming Hsu, Shyankay Jou, Jr-Tai Chen, Ping-Jung Huang, Hsu-Cheng Hsu, Han-Chang Shih, Kuei-Hsien Chen, Li-Chyong Chen, OPTICS EXPRESS, 17, 11690 (2009)

Palatnikov, M.N., Sandler, V.A., Sidorov, N.V., Makarova, O.V., Biryukova, I.V., Efremov, I.N. and Ivanenko, D.V.,Physics of the Solid State, 57,1541(2015)

Pamu D., Lakshmi Narayana Rao G., James Raju K.C., Journal of American Ceramic Society, 95, 126 (2012)

Pamu D., Lakshmi Narayana Rao G., Raju K.C.James, Advances in applied ceramics, 106, 202 (2007)

Patrick PONS, Herve AUBERT, Philippe MENINI, Manos TENTZERIS, Procedia Engineering, 47, 1474 (2012)

Peng You, Chaojing Lu, Wanneng Ye, Lanzhong Hao, Jun Zhu, Yichun Zhou, Appl. Phys. Lett., 102, 051914 (2013)

Penn Stuart J, Alford Neil McN, Templeton Alan, J. Am. Ceram. Soc., 80, 1885 (1997)

Pinar Beyazkilic, Adem Yildirim, Mehmet Bayindir, ACS Appl. Mater. Interfaces, 6, 4997 (2014)

Poolman, R.H., Ivanov, A.L. and Muljarov, E.A., Applied Physics Letters, 98, 263505 (2011)

Pramodini S., Sudhakar Y.N., SelvaKumar M., Poornesh P., Laser Physics, 24, 4 (2014)

Qin X., Zhou G., Yang Y., Zhang J., Shu X., Shimai S., Wang S., Ceramics International, 40, 12745 (2014)

Qingwei Liao and Lingxia Li, Dalton Transactions 41, 6993 (2012)

Qu-Quan W., Jing S., Bai-Feng Y., Hai-Lin L., Gui-Guang X., Qi-Huang G., Qi-Kun X., Chinese physics letters, 19, 677 (2002)

Ramarao S.D., Murthy V.R.K., Dalton Trans, 44, 2311 (2015)

Reddy, H., Guler, U., Kildishev, A.V., Boltasseva, A. and Shalaev, V.M., Material Science (In press) (2016)

Rémi Lazzari, Jacques Jupille, Surf. Sci. 482, 823 (2001)

Richard G. Smith, Natasha D'Souza, Stephen Nicklin, Analyst, 133, 571 (2008)

Rick Ubic, Steven Letourneau, Sherin Thomas, Chemistry of Materials, 22, 4572 (2010)

Riefer A., Friedrich, Sanna M., Gerstmann U., Arno Schindlmayr, W. G. Schmidt W.G., Phys. Rev. B 93, 075205 (2016)

Ringleb S., Rademaker K., Nolte S., Tünnermann A., Applied Physics B, 102, 59 (2011)

Salles M.O., Meloni G.N., de Araujo W.R., Paixão T.R.L.C., Anal. Methods, 6, 2047 (2014)

Sangeetha R., Muthukumaran S., Journal of Material Science: Materials in Electronics, 26, 9667 (2015)

Santanu Dhara, Parag Bhargava, J. Amer. Cer. Soc., 84, 3048 (2011)

Saralasrita Mohanty, Bodhisatwa Das, Santanu Dhara, Journal of Asian Ceramic Societies, 1, 184 (2013)

Satapathy S., Chandrachur Mukherjee, Taruna Shaktawat, Gupta P.K., Sathe V.G., Thin Solid Films, 520, 6510 (2012)

Schneider E.,P. J. Cress man P.J., Holman R.L., J. Appl. Phys. 53, 4054 (1982)

Scott J.F. ISRN Materials Science, 187313 (2013)

Sebastian M., "Dielectric Materials for Wireless Communication, 1st Edition", Elsevier Science (2008)

Setter N., Damjanovic D., Eng L., Fox G., Gevorgian S., Hong S., Kingon A., Kohlstedt H., Park N.Y., Stephenson G.B., Stolitchnov I., Taganstev A.K., Taylor D.V., Yamada T., Streiffer S., J. Appl. Phys. 100, 051606 (2006)

Shandilya S., Tomar M., Gupta, V., J. Appl. Phys., 111, 102803 (2012)

Shandilya S., Tomar M., Sreenivas K., Gupta V., Journal of Light wave Technology, 28, 3004 (2010)

Shandilya S., Tomar, M., Sreenivas, K. and Gupta, V., J. Appl. Phys., 105, 4105 (2009)

Shandilya, S., Tomar, M. and Gupta, V., J. Appl. Phys., 111,102803 (2012)

Sharma P., Sreenivas K., Belova L.M., Rao K.V., Journal of materials research, 18, 2025 (2003)

Sheik-Bahae M., Said A.A., Wei T., Hagan D.J., Van Stryland E.W., IEEE J. Quantum Electron., 26, 76 (1990)

Shen, L., Xu, X., Lu, W. and Shi, B., Ceramics International, 4, 5569 (2016)

Shibata, Y., Kuze, N., Matsui, M., Kanai, M. and Kawai, T., Japanese journal of applied physics, 36, 7344 (1997)

Shihui Yu, Lingxia Li, Weifeng Zhang, Zheng Sun, Helei Dong, Scientific Reports, 5, 10173 (2015)

Shu- Ran Zhang, Dong-Ying Du, Jun-Sheng Qin, Shao-Juan Bao, Shun-Li Li, WenWen He, Ya-Qian Lan, Ping Shen, Zhong-Min Su, Chem. Eur. J., 20, 3589 (2014)

Silva K.C., Sakai O.A., Steimacher A., Pedrochi F., Baesso M.L., Bento A.C., Medinaa A.N., Lima S.M., Oliveira R.C., Moraes R.C.S., Yukimitu K., Araújo E.B., Petrovich M., Hewak D.W, J. Appl. Phys., 102, 073507 (2007)

Simoes, A.Z., Zaghete, M.A., Stojanovic, B.D., Riccardi, C.S., Ries, A., Gonzalez, A.H. and Varela, J.A., Materials Letters, 57, 2333 (2003)

Soma Venugopal Rao, P T Anusha, T S Prashant, Debasis Swain, Surya P Tewari, Material Sciences and Applications 2, 299 (2011)

Sones, C., Mailis, S., Apostolopoulos, V., Barry, I.E., Gawith, C., Smith, P.G. and Eason, R.W., Journal of Micromechanics and Micro engineering, 12, 53 (2001)

Song, Z., Xu, Q., Zhang, S., Liu, H., Luo, W., Hao, H., Cao, M., Yao, Z., Hu, W., Shi, Y. and Lanagan, M.T., Journal of the American Ceramic Society 98, 3212 (2015)

Subba Rao T., Murthy V.R.K., Viswanathan B., Ferroelectrics 102, 155 (1990)

Subodh, G. and Sebastian, M.T., Materials Science and Engineering: B, 136, 50 (2007)

Sulong T.A.T., Osman R.A.M., Idris M.S., AIP Conf. Proc. 1756, 070003 (2016)

Sultan Ben-Jaber, William J. Peveler, Raul Quesada-Cabrera, Emiliano Cortés, Carlos Sotelo-Vazquez, Nadia Abdul-Karim, Stefan A. Maier, Ivan P. Parkin, Nature Communications, 7, 12189 (2016)

Sun Y., Shimai S., Peng X., Zhou G., Kamiya H., Wang, S., Ceramics International, 40, 8841 (2014)

Sundari, S.T., Chandra, S. and Tyagi, A.K., Journal of Applied Physics, 114, 033515 (2013)

Sundari, S.T., Srinivasu, K., Dash, S. and Tyagi, A.K., Solid State Communications, 167, 36 (2013)

Takahashi, M., Iyoda, K., Miyauchi, T., Ohkido, S., Tahashi, M., Wakita, K., Kajitani, N., Kurachi, M. and Hotta, K., J. Appl. Phys., 106, 044102 (2009)

Tatsuya Ishikawa, Hitoshi Takagi, U.S.Patent No.6, 403, 512 (2002)

Taudte, R.V., Beavis, A., Wilson-Wilde, L., Roux, C., Doble, P. and Blanes, L., Lab on a Chip, 13,4164 (2013)

Thierfelder C., Sanna S., Arno Schindlmayr, Schmidt W.G., Phys. Status Solidi C, 7, 362 (2010)

Tomar, M., Mehan, N., Sreenivas, K. and Mansingh, A., Ferroelectrics, 329, 61 (2005)

Tomita, Y., Sugimoto, M. and Eda, K., Applied physics letters, 66, 1484 (1995)

Tripura Sundari S., Kunuku Srinivasu, S. Dash S., A.K. Tyagi A.K., Solid State Communications, 167, 36 (2013)

Tripura Sundari S., Sharat Chandra, Tyagi A.K., Journal of Applied Physics, 114, 033515 (2013)

Ubic Rick, Letourneau Steven, Thomas Sherin, Chem. Mater., 22, 4572 (2010)

Venkata Saravanan K., James Raju K.C., Ghanashyam Krishna M., Surya P. Tewari, Venugopal Rao S., Appl. Phys. Lett. 96, 232905 (2010)

Vinod E.M., Ramakanta Naik, Faiyas A.P.A., Ganesan R., Sangunni K.S., Journal of Non-Crystalline Solids, 356, 2172 (2010)

Wan, T., Yao, D., Hu, H., Xia, Y., Zuo, K. and Zeng, Y., Materials Letters, 133, 190 (2014)

Wan, W., Feng, Y., Yang, J., Xu, S. and Qiu, T., Journal of the European Ceramic Society, 35, 2163 (2015)

Wang C.L., Lee H.Y., Azough F., Freer R., J. Mater. Sci., 32, 1693 (1997)

Wang J., Zhang, F., Chen, F., Zhang, H., Tian, R., Dong, M., Liu, J., Zhang, Z., Zhang, J. and Wang, S., Journal of the American Ceramic Society, 97, 1353 (2014)

WANG Qu-Quan, SHI Jing, YANG Bai-Feng, LIU Hai-Lin, XIONG Gui-Guang, GONG Qi-Huang, XUE Qi-Kun, CHIN.PHYS.LETT. , 19, 677 (2002)

Wang S., Jia D., Yang Z., Duan X., Tian Z., Zhou Y., Ceramics International, 39, 4231 (2013)

Wang X., Tian, S., Man, W., Jia, J. and Shi, X., Crystal Research and Technology, 47, 719 (2012)

Wang X., Ye, Z. and Zhao, B., Solid state communications, 142, 694 (2007)

Wang, J., Zhang, F., Chen, F., Zhang, H., Tian, R., Dong, M., Liu, J., Zhang, Z., Zhang, J. and Wang, S., Journal of the American Ceramic Society, 97, 1353 (2014)

Wang, S., Jia, D., Yang, Z., Duan, X., Tian, Z. and Zhou, Y., Ceramics International, 39,4231 (2013)

Wang, X., Tian, S., Man, W., Jia, J. and Shi, X., Crystal Research and Technology,47, 719 (2012)

Wang, X., Ye, Z. and Zhao, B., Solid state communications, 142, 694 (2007)

Ward D.W., Statz, E.R., Nelson, K.A., Roth, R.M. and Osgood, R.M., Applied Physics Letters, 86, 2 (2005)

Weis R.S., T. K. Gaylord T.K., Applied Physics A, 37,191 (1985)

Wen C.J., Yang, J.S., Optoelectronics Letters, 1, 1 (2005)

Woo Seok Choi, Ho Nyung Lee, Appl. Phys. Lett. 100, 132903 (2012)

Wu J.M., Zhang X.Y., Yang J.L., Journal of the European Ceramic Society, 34, 1089 (2014)

Xiangcheng Sun, Ying Wang,   Yu Lei, Chem. Soc. Rev., 44, 8019 (2015)

Xie Cheng Fan, Xiang Ming Chen, Xiao Qiang Liu, Chem. Mater., 20, 4092 (2008)

Xie, H., Chen, C., Su, B. and Xi, H., Materials Letters, 166, pp.167-170 (2016)

Xiong Z. X., Fang C., Wang Y.X., Su Z.G., J. Eur. Cer. Soc. 25, 2071 (2005)

XU Jian-Ping, SHI Shao-Bo, LI Lan, ZHANG Xiao-Song, WANG Ya-Xin, CHEN Xi-Ming, CHIN. PHYS. LETT., 27, 047803 (2010)

Yakovlev V.Yu., Kabanova E.V., Weber T., Paufler P., Physics of the Solid State, 43, 1580 (2001)

Yan Geng, Mohammad A. Ali, Andrew J. Clulow, Shengqiang Fan, Paul L. Burn, Ian R. Gentle, Paul Meredith, Paul E. Shaw, Nature Communications, 6, 8240 (2015)

Yang J., Gao Y.Q., Wu J., Huang Z.M., Meng X.J., Shen M.R., Sun J.L., Chu J.H., J. Appl. Phys. 108, 114102 (2010)

Yang, M., Gong, Y., Yu, X., Feng, L., Shi, Y., Huang, Z., Xiang, X., Wei, J. and Lu, T., Ceramics International, 42, 2180 (2016)

Yi, L., Li, L., Liu, X.Q. and Chen, X.M., Journal of the American Ceramic Society, 97, 3531 (2014)

Yih-Chien Chen, Ren-Jie Tsai, Materials Chemistry and Physics, 129, 116 (2011)

Yikai Chen, Chao-Fu Wang, (2015) Characteristic Mode Theory for Dielectric Resonators, in Characteristic Modes: Theory and Applications in Antenna Engineering, John Wiley & Sons, Inc, Hoboken, NJ, ch4

Ying Cheng, Ruzhong Zuon, Yang Lv, Ceramics International, 39, 8681 (2013)

You, P., Lu, C., Ye, W., Hao, L., Zhu, J. and Zhou, Y., Appl. Phys. Lett., 102, 051914 (2013)

Yunlan Wang, Xinyi Li, Guoshun Jiang, Weifeng Liu, Changfei Zhu, J Mater Sci: Mater. Electron. 24, 3764 (2013)

Yun-Shan Xue, Yabing He, Lian Zhou, Fei-Jian Chen, Yan Xu, Hong-Bin Du, Xiao-Zeng You, Banglin Chen, J. Mater. Chem. A, 2013, 1, 4525 (2013)

Zarei, A.R. and Ghazanchayi, B., Talanta, 150, 162 (2016)

Zawrah M.F., Khattab R.M., Girgis L.G., Daidamony H.El , Rehab E. Abdel Aziz, "Stability and electrical conductivity of water-base Al2O3nanofluids for different applications", HBRC Journal (In press)

Zhang J., Jiang, D., Lin, Q., Chen, Z. and Huang, Z., Journal of the European Ceramic Society, 33, 1695 (2013)

Zhang J., Jiang, D., Lin, Q., Chen, Z. and Huang, Z., Materials & Design, 65, 12 (2015)

Zhang, J., Jiang, D., Lin, Q., Chen, Z. and Huang, Z., Journal of the European Ceramic Society, 33, 1695 (2013)

Zhang, J., Jiang, D., Lin, Q., Chen, Z. and Huang, Z., Materials & Design, 65, 12(2015)

Zhang, J., Zhou, Y., Yue, Z., Zhang, X. and Li, L, Journal of the American Ceramic Society, 98, 3942 (2015)

Zhou, D., Li, W.B., Xi, H.H., Pang, L.X. and Pang, G.S., Journal of Materials Chemistry C, 3, 2582 (2015)

Zou C., Zhang C., Li B., Wang S., Cao F., Materials & Design, 44, 114 (2013)

List of patents

1. **Anil Tumuluri**, Padala Missak Swarup Raju, Vummethala Seshubai, Thankappan Pillai Rajasekharan, K C James Raju, "**A method for the preparation of Dielectric Resonators of arbitrary shapes**" (under evaluation) Filed for an Indian patent application no. 2305/CHE/2014

List of Publications/proceedings

1. Anil Tumuluri, M Swaroop, V Seshubai, T Rajasekharan, K C James Raju, "Fabrication of $(Zr_{0.8}Sn_{0.2})TiO_4$ dielectric resonators in arbitrary shapes" **Material Letters**,154, 128, 2015.

2. Anil Tumuluri, Sandeep Marka, K C James Raju, VVSS Srikanth, "Dielectric properties of novel composites prepared with few layered graphene (FLG)-lithium triniobate $(LiNb_3O_8)$" **AIP Conference Proceedings**, 1675, 020043, 2015**.**

3. J Pundareekam Goud, S Bashaiah, Anil Tumuluri, K C James Raju, "Microwave Absorption Properties of $LiNb_3O_8$ in X-band prepared by combustion synthesis" **AIP conference Proceedings**, 1675, 020024, 2015**.**

4. Anil Tumuluri, K C James Raju, "Luminescence of $LiNbO_3$ polycrystalline ceramics: Effect of Sc_2O_3 and Lu_2O_3 doping." **Ceramics International**, 40, 3371, 2014.

5. Anil Tumuluri, K Lakshun Naidu, K.C.James Raju, "Band gap determination using Tauc's plot for $LiNbO_3$ thin films." **International Journal of Chem. Tech Research**, 6, 6, 3353, 2014.

6. J. Rama Krishna, Anil Tumuluri, R. Naresh Kumar, K. C. James Raju, V. V. S. S. Srikanth "Copper Oxide Decked Few-Layered Graphene: Synthesis and Dielectric Behavior." **Carbon**, 78, 374, 2014.

7. Anil Tumuluri, K.C.James Raju, "Stoichiometric $LiNb_3O_8$ thin films using microwave annealing" **Advanced Material Letters**, 5, 287, 2013.

8. Rambabu A, Anil Tumuluri, K C James Raju, "Variation in mechanical properties of SBTi thin films with substrate temperature using RF sputtering technique" **Advanced material Letters**, 5, 292, 2013.

9. V. Madhurima, O Sravya, Anil Tumuluri, K C James Raju "Dielectric spectroscopy of binary liquid systems as prototypes for interactions in Biological systems" **IEEE proceeding in IEEE conference on liquid dielectrics**, Bled, Slovenia, June 30-July 3, 2014.

Workshops/Conferences attended

1. DST-SERC school on "Guided wave optics and devices" at Central Glass and Ceramic Research Institute (CGCRI), Kolkata during 7th- 25th February, 2011 (Participant-got selected by organizers).

2. Workshop on Ceramics, Carbides and Diamonds (CCD-11), at College of Engineering, Pune during 8th- 10th December, 2011 (Participant).

3. International Conference on Nanoscience and Technology (ICONSAT-2012) at Taj Banjara Hyderabad during 20th -23rd January, 2012 (Poster presentation).

4. International Conference and workshop on Nanostructured Ceramics and other Nanomaterials (ICWNCN-2012) at University of Delhi, Delhi during 13th -16th March 2012 (Poster presentation).

5. National workshop on Recent Trends in RF and Microwave techniques and measurements at Department of Avionics, IIST, Valiamala, Thiruvananthapuram in collaboration with IIT Kanpur and Vikram Sarabhai Space Centre (VSSC) during 18th – 20th July, 2012 (Participant).

6. 17th National Seminar on Ferroelectrics and Dielectrics (XVII NSFD-2012) at Institute of Technical Education and Research (ITER), Bhubaneswar, Odisha at Siksha 'O' Anusandhan University, Bhubaneswar during 17th – 19th December 2012 (Poster presentation).

7. Awareness workshop of UGC-DAE consortium for Scientific Research organized by UGC-DAE consortium for scientific Research, Mumbai Centre and School of Engineering Sciences and Technology at University of Hyderabad during 28th – 30th October,2013 (Participant).

8. International Conference IUMRS-ICA-2013 at IISc. Bangalore, Bangalore during 16th – 20th December, 2013 (Poster presentation).

9. International Conference on Condensed Matter and Applied Physics (ICC-2015) at Govt. Engineering college, Bikaner, Rajasthan during 30th - 31st October, 2015 (Poster presentation).

MULTIFACETED PROPERTIES OF LiNbo3 THIN FILMS FOR OPTICAL APPLICATIONS AND POROUS